Noise Mitigation in Searches for Gravitational Waves from Compact Binaries and Cosmic Strings

by

Adrian Francis Helmling-Cornell

A dissertation accepted and approved in partial fulfillment of the

requirements for the degree of

Doctor of Philosophy

in Physics

Dissertation Committee:

Ben Farr, Chair

Raymond Frey, Advisor

Timothy Cohen, Core Member

Robert Schofield, Core Member

Marina Guenza, Institutional Representative

University of Oregon

Summer 2025

© 2025 Adrian Francis Helmling-Cornell
This work is licensed via
CC-BY 4.0.



DISSERTATION ABSTRACT

Adrian Francis Helmling-Cornell

Doctor of Philosophy in Physics

Title: Noise Mitigation in Searches for Gravitational Waves from Compact Binaries and Cosmic Strings

The LIGO-Virgo-KAGRA network of gravitational wave detectors have identified hundreds of gravitational waves since 2015. Their continued success is due in part to continuing efforts to identify and mitigate environmental noise of known and unknown origin which contaminates detector data. As the number of gravitational waves detected by these facilities continues to grow, automating data quality checks, namely estimating the contribution of environmental noise to detector strain data around the times of gravitational wave candidate events, is critical to producing reliable gravitational wave data.

To date, all directly-detected gravitational waves come from compact binary coalescences. However, cusps along cosmic string loops are also sources of gravitational waves, and—should they exist—are promising probes of Beyond the Standard Model physics. Here, new constraints on Beyond the Standard Model physics are presented from the search for gravitational waves from cosmic string cusps in the first part of the fourth observing run of LIGO-Virgo-KAGRA. Techniques from compact binary coalescence data analysis are applied to injected cosmic string signals to study their behavior in the case that gravitational waves from cosmic strings are detected in future observing campaigns.

This dissertation includes previously published and unpublished coauthored material.

ACKNOWLEDGEMENTS

No man is an island. I am deeply indebted to the University of Oregon and LIGO communities and my family for their companionship and mentorship over the course of my degree.

I do not know how I would have gotten through my first year of study here without the Binney crew, especially Aria Radick, Alex Quinn, Claire Albrecht, Hannes Sobottka, Jeremy Metzner and Will Parker. In some sort of twisted way, I look back fondly on those late nights at the chalkboards working through quantum mechanics problem sets. I thank Bruce Edelman and Kara Merfeld for welcoming me into the Oregon LIGO group and teaching me many of the tools I needed to be an effective researcher. My thanks are also due to Philippe Nguyen, who taught me so much about the detectors and who helped me realize some of my first projects, and Zoheyr Doctor, who encouraged me to publish the work of chapter IV. Most especially, I would like to recognize Matthew Ball, who as a Binney office-mate and my desk neighbor in the lab, had to put up with seven years of being a sounding board for shoddy math, poorly written code and half-baked project ideas. You listened without judgement and were always willing to entertain whatever wild tangent or question I came in with each day. The last seven years would not have been the same without you.

I would also like to thank Anne McGinley and Claire Staley; their hard work made my travel to the observatories and conferences possible. I appreciate the teaching and advice of my committee members, Tim Cohen, Ben Farr.
Their classes shaped my early research interests and their mentorship helped me navigate the worries of graduate school, choosing research topics, and life post-

graduation. Along with Marina Guenza, I especially value their careful review of this dissertation. I owe so much to the careful guidance of Robert Schofield, who always made time to teach me about the observatory, our analyses, and most importantly, how to be a better scientist. I strive to be like you in my work. Lastly, I thank my advisor Raymond Frey for his support and flexibility. I deeply value the freedom that I had during my time here to pursue topics that interested me, even if they were not the projects he had envisioned me working on.

There are too many colleagues in the LIGO Collaboration who deserve special recognition for their friendship and mentorship and so little room to list them. But I especially want to thank Daichi Tsuna, Daniel Sigg, Derek Davis, Dripta Bhattacharjee, Elenna Capote, Ethan Payne, Jeffrey Kissel, Jenne Driggers, Laurence Datrier, Mike Landry, Rick Savage, Sheila Dwyer, Siddharth Soni and Varun Srivastava for one or both.

Lastly, I thank my family, especially Bill, Cindy, John & Karen and most especially Cara for their constant support at every step in my degree. I could not have done this without you.

This dissertation is dedicated to Cara Christensen, *mi media naranja*, without whose love and support none of this would have been possible, and to Roo, without whose love I probably would have graduated a year sooner.

TABLE OF CONTENTS

Chapter Page

I. INTRODUCTION 17

II. GRAVITATION AND GRAVITATIONAL WAVES 19

2.1. Mathematical Descriptions of Gravity 19

2.1.1. Newtonian Gravity 19

2.1.2. Special Relativity 22

2.1.3. General Relativity 23

2.1.3.1. The Einstein Field Equations 26

2.2. Gravitational Waves 27

2.2.1. Wave Solutions to the Einstein Field Equations 27

2.2.1.1. Linearized Gravity 27

2.2.1.2. Lorenz Gauge 29

2.2.1.3. Gravitational Waves 31

2.2.2. Astrophysical Sources of Gravitational Waves 32

2.2.2.1. Compact Binary Coalescences 34

2.2.2.2. Other Transient Phenomena 39

2.2.2.3. Continuous Gravitational Waves 41

2.2.2.4. The Stochastic Gravitational Wave Background . . . 42

2.2.2.5. Cosmic Strings 42

III. GRAVITATIONAL WAVE INTERFEROMETRY 47

3.1. Gravitational Wave Interferometery 48

3.1.1. Detection Principles 48

3.1.2. Interferometry in Practice 49

Chapter Page

3.2. Detector Noise 50

3.2.1. Quantum and Thermal Noise 50

3.2.2. Environmental Noise 51

3.2.3. Monitoring 53

3.3. Noise Investigations 55

3.3.1. 48 Hz Noise 57

3.3.2. Magnetic Coupling 61

3.3.3. Input Power Settings and Vibrational Coupling 64

3.4. Glitches 65

3.4.1. Blip Glitches 65

3.4.1.1. Searches for Origin 66

3.4.1.2. Pre-O4 OMC Characterization 70

IV. ALGORITHMIC EVALUATION OF ENVIRONMENTAL NOISE IN LIGO 72

4.1. Automated Evaluation of Environmental Coupling for Advanced LIGO Gravitational Wave Detections 72

4.1.1. Introduction 72

4.1.2. LIGO Environmental Monitoring 75

4.1.2.1. PEM System Description 75

4.1.2.2. Studying Environmental Coupling 76

4.1.3. Quantifying Environmental Coupling 80

4.1.3.1. Data Access 80

4.1.3.2. ASD Projection 83

4.1.3.3. CF Tuning 84

4.1.3.4. c-statistic Determination 87

4.1.3.5. Combining Results 90

Chapter Page

4.1.4. Results . . . 91
4.1.4.1. Real GW Data . . . 91
4.1.4.2. GW200115_042309 . . . 94
4.1.4.3. GW190917_114630 . . . 96
4.1.4.4. GW190930_133541 . . . 97
4.1.4.5. Simulated GW Signals . . . 100
4.1.5. Conclusions . . . 102
4.2. PEMcheck Performance in O4 . . . 104
4.2.1. Integration with DQR . . . 104
4.2.2. Results . . . 105
4.2.2.1. S230524x . . . 105
4.2.2.2. S240624cd . . . 107
4.2.2.3. O4a All-sky Burst Search Candidates . . . 110
V. RESULTS OF THE SEARCH FOR COSMIC STRINGS WITH LIGO IN THE FIRST PART OF THE FOURTH OBSERVING RUN . . . 113
5.1. Search Method . . . 113
5.1.1. Search Pipeline . . . 113
5.1.2. Search Configuration . . . 114
5.1.2.1. Data Acquisition and Timesliding . . . 114
5.1.2.2. CS Template Bank Preparation and Injection . . . 116
5.1.2.3. Single-Detector Search . . . 118
5.1.2.4. Coincident Trigger Identification . . . 120
5.1.2.5. Likelihood Calculation . . . 121
5.2. Search Results . . . 122
5.2.1. Cusp Search Results . . . 122

Chapter Page

5.2.2. Constraints on Cosmic String Population 126

5.2.2.1. Upper Limits Formalism 126

5.2.2.2. Loop Distribution Models 129

5.2.2.3. Cosmic String Population Constraints from the O4a Search 132

VI. PARAMETER ESTIMATION FOR GRAVITATIONAL WAVES FROM COSMIC STRINGS 137

6.1. Introduction 137

6.2. Methods 139

6.2.1. CS Gravitational Waveforms 139

6.2.2. Frequency-domain Inference 140

6.3. Results 141

6.3.1. O3 Results 141

6.3.2. A+ Results 146

6.4. Discussion 146

6.4.1. CS Signal Type Sensitivity 146

6.4.2. Instrumental Artifacts 147

VII. CONCLUSION 152

LIST OF FIGURES

Figure Page

1. The reaction of two rings of freely-falling test particles to a passing GW. . . . 33
2. A comparison between of each LIGO detector's noise sensitivity in O3 and O4a. . . . 38
3. The number of GW events confidently detected by LIGO through April 1, 2025. . . . 40
4. A sketch of the optical layout of a LIGO detector. . . . 49
5. Noise budgets for LHO in O3 and O4a. . . . 52
6. Response of the endstation accelerometer and DARM to an acoustic injection from 60-100 Hz. . . . 56
7. CF for the endstation accelerometer computed from the injection shown in figure 6. . . . 57
8. Spectrograms showing time and frequency correlation between 48 Hz noise in GW strain data from LHO and an accelerometer placed on a vacuum chamber wall located near the noise source. . . . 58
9. Comparing responses of DARM and LHO corner station accelerometers to beating-shakers injection. . . . 60
10. $h(t)$ data from 6 of the 22 weekly high-frequency magnetic injections performed at the LHO corner station. . . . 62
11. Comparison of detector strain data during high-frequency magnetic injection times for each injection shown in figure 10 and reference background times taken a few minutes prior to each injection. . . . 63
12. Comparison of the composite vibrational CF between PEM sensors placed around the pre-stabilized laser optics table measured during 75 W and 60 W operation. . . . 65

Figure Page

13. Q-transform of a whistle glitch and an extremely loud glitch in GW strain data. . . . 66

14. Rate of blip glitches in the LIGO detectors from O2 to April 1, 2025. . . . 67

15. Distribution of blip glitch durations in LHO and LLO in O2-O4 through April 1, 2025. . . . 67

16. Distribution of blip glitch bandwidths in LHO and LLO in O2-O4 through April 1, 2025. . . . 68

17. Timeseries of the mass storage room humidity and the blip glitch rate at LHO in O3. . . . 69

18. Histograms of time delay between cosmic ray detections in LHO and blip glitches in O2 and O3. . . . 70

19. Calibrated strain and OMC photodiode data from LHO during an O3 blip glitch and OMC photodiode data from the no-light test. . . . 71

20. Comparison between blip glitch and Omicron trigger properties for data from the OMC mock-up. . . . 71

21. Vibrational coupling between LLO's HAM 6 vacuum chamber Z-axis accelerometer and DARM as measured prior to O3. . . . 79

22. ASD of the Z-axis HAM 6 accelerometer during the background time. . . . 84

23. Comparison of the CF interpolated from the data in figure 21 to the interpolated, tuned CF and comparison of the DARM t_{back} ASD with the estimated contribution from the HAM 6 accelerometer. . . . 85

24. The results of the c-statistic calculation for each spectrogram tile for the LLO HAM 6 accelerometer during GW190707. . . . 90

25. Histogram of the minimum c-statistic calculated by PEMcheck for all O3 events using the pre-O3 coupling data. . . . 92

Figure Page

26. Cumulative distribution of the c-statistic found for each PEM channel studied by PEMcheck for each GW event in O3 using the pre-O3 coupling data. 93

27. CDF of the c-statistic for each run of PEMcheck at LHO with GW200115's properties. 97

28. Constant-Q transform of LHO GW strain and signal recycling cavity beamtube accelerometer data centered on GW190930_133541's arrival time. 99

29. Constant-Q transform of LLO GW strain data during a thunderclap witnessed by PEM sensors with hypothetical GW tracks overlaid. 101

30. Histogram of the minimum c-statistic found by each PEMcheck run in O4 through April 1, 2025. 106

31. The results of PEMcheck for each PEM channel for each event in the subset of fourth observing run (O4) considered in this work. 106

32. Likelihood of coupling for four LHO PEM sensors during a claimed BNS signal. 108

33. Strain data near the time of the unmodeled search candidate GW S240624cd. 109

34. Spectrogram of accelerometer data near the gravitational wave (GW) candidate time. 110

35. CF and estimated ambient contribution to DARM of a GS-13 seismometer. 111

36. Flowchart of tasks used to find CS candidates in LIGO data. 115

37. Distribution of the SNR mismatch found for four CS cusp templates in the $\sim$400 up to hour-long searches conducted at LHO and LLO. 118

38. Template banks used for the O4a search. 119

39. Variation in the CS search sensitivity for different choices of the search starting frequency. 120

40. Difference in the f_h inferred from LHO and LLO strain data for the CS injections and the noise background. 123

Figure Page

41. Difference in inferred arrival times for CS injections and CS triggers caused by noise at each LIGO site. 123

42. Discrepancy between detector amplitudes for triggers from CS injections and noise. 124

43. Single-detector signal consistency test results. 124

44. Rate of triggers with a given likelihood found in the O4a blinded results. 125

45. Comparison of $A_{50\%}$ for the O3 and O4a CS cusp searches. 126

46. Comparison of LHO and LLO strain data near the highest-ranked background event found by the CS search. 127

47. Allowed and excluded values of the string tension in the RSB model due to their non-observation in O3 and assuming a non-observation in the unblinded O4a search data. 133

48. Allowed and excluded values of the string tension in the ARMS-RSB-mat model due to their non-observation in O3 and assuming a non-observation in the unblinded O4a search data. 133

49. Allowed and excluded values of the string tension in the ARMS-RSB-rad model due to their non-observation in O3 and assuming a non-observation in the unblinded O4a search data. 134

50. Upper limit on $G\mu$ for past and current CS cusp searches for a variety of N_k per CS loop in the RSB model, assuming a non-detection in the O4a search data. 135

51. Observable O4a burst rate for the ARMS-RSB-mat and ARMS-RAD-rad models for different N_ks. 136

52. Amplitude spectral densities used to generate realistic detector noise for this chapter. The third observing run (O3) traces correspond to already realized detector sensitivities, while the Advancced LIGO Plus (A+) curve represents a hypothetical noise budget for these facilities in the future. 141

53. Performance of the PE method described herein on a cusp, kink, kink-kink collision signal. 144

Figure Page

54. Comparison between the logarithm of the signal versus noise Bayes factor and SNR of the injected dataset. 145

55. Q-transforms of a blip glitch, as identified by GravitySpy in O3 data from LLO and a CS cusp waveform injected into noise drawn from the O3 LHO noise spectral density shown in figure 52. 148

56. Results of PE around a blip glitch that occurred in O3. 150

57. Kernel density estimate of inferred power law index and high frequency cutoff distributions for the 58 O3 blip glitches considered in this work. 151

LIST OF TABLES

Table Page

1. Basic detection information and initial estimates of source frame masses and dimensionless spins for GW190707. 82

2. The number of O3 GW events where the tuning procedure was used in calculating the time-frequency tile with the highest likelihood of contamination. 94

3. Estimates of source frame masses and dimensionless spins for GW190521. 100

4. Naming conventions used for CS loop population models. 132

5. Upper limit on CS tension for each model set by non-observation. 135

6. Limits on the CS tension inferred from O4a for several choices for N_k. 136

7. Parameter combinations for the waveforms injected into O3 noise. 142

8. Prior choices for the O3 injections. 142

9. The result of model selection for $8 \leq \rho \leq 10$ CS injections. 147

CHAPTER I

INTRODUCTION

> *"What is great in man is that he is a bridge and not a goal: what is lovable in man is that he is an over-going and a going under."*
>
> —Friedrich Nietzsche, *Thus Spoke Zarathusthra* [1]

Over the course of the past decade, direct GW detection has been transformed from an aspirational goal to a routine occurence. With hundreds of GWs from compact binary coalescences (CBCs) detected through April 1, 2025 by the LIGO-Virgo-KAGRA Collaboration, concerns have shifted from the feasibility of finding GW signals in interferometer data to recovering small features in GW waveforms which hint at the properties of the universe's population of black holes (BHs) and neutron stars (NSs).

Despite these successful searches for GWs from CBCs, other possible sources of GWs have yet to be found with the LIGO-Virgo-KAGRA network. These include the "monotone" GWs emitted by rapidly spinning single NSs, supernovae, accretion disk instabilities around compact objects, and many other interesting systems. One particularly interesting class of potential GW sources are cosmic strings (CSs). These are topological defects which may have been formed in the early universe via spontaneous symmetry breaking. Careful study of GWs from these objects will reveal the energy scale of the string-forming symmetry breaking. Knowing this energy scale gives us insight into the behavior of the universe at its earliest moments and highest energies.

This dissertation is organized as follows: chapter II presents a historical and mathematical review of gravitational theory, concluding with a discussion of GWs

and GW sources. Chapter III details the design and operation of interferometers used for direct detection of GWs and discusses noise sources which affect the sensitivities of these detectors. Portions of this chapter describing environmental noise studies appear in previously published work authored by the LIGO Instrument Science/Detector working group under the leadership of Siddharth Soni. Chapter IV describes an automated tool for assessing environmental noise contamination near the GW candidate event times and details the performance of this tool when applied to GWs detected from 2019-2025. The first half of this chapter was previously published with the assistance of Philippe Nguyen, Robert Schofield and Raymond Frey. Chapter V describes the design of and presents results for a search for GWs from CSs in interferometer data collected in 2023 and 2024. Chapter VI extends mathematical routines applied to GWs from CBCs to extract information about the progenitor and remnant NSs or BHs to synthetic CS signals added to observatory data and explores their efficacy at recovering the underlying properties of the CSs. This chapter consists of unpublished material; Daichi Tsuna and Raymond Frey contributed to the analysis presented in this chapter. Finally, chapter VII concludes with remarks about directions for future research.

CHAPTER II

GRAVITATION AND GRAVITATIONAL WAVES

> *Tis true without lying, certain & most true. That which is below is like that which is above & that which is above is like that which is below to do the miracles of one only thing... It ascends from the earth to the heaven & again it descends to the earth & receives the force of things superior & inferior. By this means you shall have the glory of the whole world & thereby all obscurity shall fly from you. Its force is above all force. For it vanquishes every subtile thing & penetrates every solid thing.*
>
> —Isaac Newton, *Translation of the Tabula Smaragdina* [2]

2.1 Mathematical Descriptions of Gravity

2.1.1 Newtonian Gravity The first formal description of gravity appears in Isaac Newton's classic treatise *Principia Mathematica*. In this work, key properties of gravity, including the shell theorem and the inverse square behavior of gravitational forces, are first rigorously proved to demonstrate that orbits subject to an inverse square attractive force take the shape of ellipses [3]. In modern notation, Newton's description of gravity can be written as

$$\vec{F}(\vec{r}) = -G\frac{mM}{r^2}\hat{e}_r \tag{2.1}$$

with $\vec{F}$ the gravitational force between two point masses, m and M, G the universal gravitation constant, r the distance between the masses and $\hat{e}_r$ the unit vector pointing between m and M. The value of G has been found experimentally to be roughly $6.67 \times 10^{-11}\,\mathrm{m}^3/\mathrm{kg}/\mathrm{s}^2$ [4]. The corresponding gravitational potential generated by the point mass of mass M, is

$$\vec{F} = -m\vec{\nabla}\Phi. \tag{2.2}$$

Integrating both sides of equation 2.2 yields the Newtonian gravitational potential a distance r away from a point mass of mass M:

$$\Phi(r) = -\frac{GM}{r}. \tag{2.3}$$

The gravitational potential of a collection of point masses can be calculated by adding many terms in the form of equation 2.3 together. In the case of a continuous mass distribution $\rho(\vec{r})$, determining the gravitational potential at a location $\vec{r}'$ may be found by integrating each infinitesimal element of the mass distribution over all space

$$\Phi(\vec{r}) = -\int_V \frac{G\rho(\vec{r})}{|\vec{r} - \vec{r}'|} dV. \tag{2.4}$$

Taking the Laplacian of the gravitational potential highlights that mass distributions are the source of the gravitational potential field.

$$\nabla^2\Phi = 4\pi G\rho. \tag{2.5}$$

Observations show that the inertial mass, the quantity which relates how much an object accelerates when a force is applied, is equivalent to the gravitational mass of equation 2.1. As a result, for an object in a gravitational field feeling no other forces, the equations of motion are given by

$$\frac{d^2\vec{x}}{dt^2} = -\vec{\nabla}\Phi. \tag{2.6}$$

In brief, this is the system of gravitation devised by Newton, dressed in more modern language and mathematics. Collections of masses instantaneously exchange information through some uncertain means to set the value of the gravitational potential field, defined in three spatial dimensions, at a given location. A test mass placed into the field experiences a force exactly equal in magnitude to the mass of the test mass times the gradient of the field. This description of gravity is now known to be incomplete. For example, the theory fails to explain why

the gravitational mass for a body is equal to its inertial mass. Furthermore, the propagation of gravity is instantaneous in the Newtonian picture. A contemporary of Newton, Ole Rømer, made the first determination of the speed of light, suggesting that there may be a corresponding speed of gravity [5]. The physical and philosophical underpinnings of Newton's absolute space and absolute time were challenged, most notably by Ernst Mach [6].

Despite the shortcomings of Newton's gravitation, it was extraordinarily successful at describing the observable universe and predicting new phenomena. For example, prescient eighteenth century physicists using only Newtonian physics and geometry showed that certain configurations of masses could exist whose escape velocity exceeds the measured speed of light [7]. When it was found that the orbit of Uranus could not be described by the gravitational influence of the Sun and other known planets in the solar system, Newtonian physics was used to predict the mass and orbit of Neptune, leading to its discovery in 1846 [8].

Newtonian gravity, however, was eventually overturned. Precision astronomical measurements, such as the amount of precession of Mercury's perihelion, could neither be explained by Newtonian gravity nor could the disagreement between prediction and observation be explained by a massive body located between Mercury and the Sun, as suggested by some astronomers [9]. Development in other domains, such as successes in the study of electromagnetism via a field theory description, advances in geometry and tensor calculus [10], the blending of space and time needed to describe electrodynamics modulated by a constant and finite speed of light—Albert Einstein's special relativity [11], laid the foundation for Newtonian gravity's eventual successor: the general theory of relativity.

2.1.2 Special Relativity

Special relativity is the theory of dynamics in a locally flat spacetime. It rests upon two postulates: first, that experiments conducted in different inertial reference should agree with one another and second, that the speed of light in a vacuum, c, is measured the same in any reference frame. While Newtonian mechanics satisfies the first of these postulates, it cannot satisfy the second [12]. Here the most relevant points of the theory as it relates to and differs from Newtonian mechanics and full general relativity; a more thorough discussion may be found in a number of references, such as [13].

A key consequence of the postulates of special relativity is that lengths and times measured by observers in inertial frames moving with respect to one another should differ. Spatial and temporal measurements made in one inertial frame can be related by Lorentz transformations to any other inertial frame. However, observers making time and length measurements in inertial frames moving with respect to one another should agree on the value of the Lorentz invariant interval Δs^2, given in Cartesian coordinates by

$$\Delta s^2 = -c^2\Delta t^2 + \Delta x^2 + \Delta y^2 + \Delta z^2. \tag{2.7}$$

An important quantity in the following discussion is the proper time, $d\tau^2$, where

$$d\tau^2 = -\frac{ds^2}{c^2}. \tag{2.8}$$

Here the infinitesimal form of the invariant interval introduced in equation 2.7 is used. The proper time describes the time measured by a clock travelling along with an inertial frame. As a point of comparison to equation 2.6, an object travelling in the flat spacetime of special relativity

$$\frac{d^2x^\mu}{d\tau^2} = 0 \tag{2.9}$$

with x^μ the 4-displacement.

2.1.3 General Relativity The restriction of special relativity to locally flat spacetimes means it too is insufficient. The presence of mass or energy can distort spacetime. Spacetime could extract or expand. Therefore a general theory of relativity is needed to account for spacetime curvature. As in the previous section, a more detailed discussion of the principles of general relativity can be found in a number of texts, a classic reference is [14]. Derivations found in [15] were also useful in formulating this section.

In the discussion that follows, the ordinary conventions of the field are adopted: the speed of light is taken to be 1, the mostly positive $(-,+,+,+)$ metric signature is used with the 0-th component corresponding to time, Greek indices run from $0-4$ while Latin indices run from $0-3$, and Einstein summation convention is used.

General relativity extends special relativity's principle of relativity. As before, experiments in different inertial frames should have the same results. But the key addition of general relativity is the realization that a freely-falling inertial reference frame is identical to a reference frame feeling an acceleration from gravitational forces. Therefore the principle of relativity and the constancy of the speed of light should extend to experiments in freely-falling observatories.

To satisfy these conditions, new mathematical objects which describe the coordinate systems of freely-falling frames and the gravitation that they are subject to must be introduced. At each event in a (not necessarily flat) spacetime, a relation can be quantifying lengths of and angles between basis vectors. The relation can vary due to curvature of the spacetime itself. This encoding is the metric tensor $g_{\mu\nu}$. It can be used to compute fundamental quantities, like the general relativistic version of the invariant interval first introduced in equation 2.7,

via

$$ds^2 = g_{\mu\nu} dx^\mu dx^\nu. \tag{2.10}$$

For the flat spacetime of chapter 2.1.2, $g_{\mu\nu}$ takes a simple form in Cartesian coordinates known as the Minkowski metric, denoted $\eta_{\mu\nu}$ where

$$\eta_{\mu\nu} = \begin{pmatrix} -1 & 0 & 0 & 0 \\ 0 & 1 & 0 & 0 \\ 0 & 0 & 1 & 0 \\ 0 & 0 & 0 & 1 \end{pmatrix}. \tag{2.11}$$

Introducing mass to the spacetime introduces curvature. For example, in the case of a spherically symmetric mass distribution with total mass M, the metric exterior to the mass takes the form, in Schwarzschild coordinates (t, r, θ, ϕ) [16]

$$g_{\mu\nu} = \begin{pmatrix} -\left(1 - \frac{2GM}{r}\right) & 0 & 0 & 0 \\ 0 & \frac{1}{1-2GM/r} & 0 & 0 \\ 0 & 0 & r^2 & 0 \\ 0 & 0 & 0 & r^2 \sin^2\theta \end{pmatrix}. \tag{2.12}$$

For any choice of metric, the equations of motion are found by finding the equations of motion in special relativity and adding a correction factor which depends on the curvature encoded in the metric. Defining the Christoffel symbols, $\Gamma^\alpha_{\mu\nu}$, as

$$\Gamma^\alpha_{\mu\nu} = \frac{1}{2} g^{\alpha\beta} (\partial_\mu g_{\nu\beta} + \partial_\nu g_{\beta\mu} - \partial_\beta g_{\mu\nu}) \tag{2.13}$$

the equations of motion, or the geodesic equation, for a free falling particle in general relativity are

$$\frac{d^2 x^\alpha}{d\tau^2} + \Gamma^\alpha_{\mu\nu} \frac{dx^\mu}{d\tau} \frac{dx^\nu}{d\tau} = 0. \tag{2.14}$$

This is consistent with special relativity. Inserting elements of the special relativity metric of equation 2.11 into equation 2.13, all elements of the Christoffel symbols vanish, leaving just equation 2.9. Furthermore, the metric of equation 2.12 which describes the space external to a spherically symmetric mass is consistent with the results from Newtonian gravity outlined in chapter 2.1.1. In the low-speed (i.e. $\frac{dx^i}{dt} << 1$ and $\frac{dt}{d\tau} \approx 1$) limit far from the static, spherically symmetric mass, the metric in equation 2.12 may be written as

$$g_{\mu\nu} = \eta_{\mu\nu} + h_{\mu\nu} \tag{2.15}$$

where $|h_{\mu\nu}| << 1$. All Christoffel symbols for the metric of equation 2.12 vanish except

$$\Gamma^{\alpha}_{tt} = \frac{1}{2} g^{\alpha\beta}(\partial_t g_{t\beta} + \partial_t g_{\alpha t} - \partial_\alpha g_{tt}), \tag{2.16}$$

so equation 2.14 becomes

$$\frac{d^2x^\alpha}{d\tau^2} + \Gamma^{\alpha}_{tt}\frac{dt}{d\tau}\frac{dt}{d\tau} = 0. \tag{2.17}$$

For non-relativistic speeds, this reduces to

$$\frac{d^2x^\alpha}{d\tau^2} + \Gamma^{\alpha}_{tt} = 0. \tag{2.18}$$

The timelike component of equation 2.18 yields

$$\frac{d^2t}{d\tau^2} + \Gamma^{t}_{tt} = 0 \tag{2.19}$$

and the spacelike components in the weak-field limit take the form

$$\frac{d^2x^i}{d\tau^2} + \Gamma^{i}_{tt} = 0 \tag{2.20}$$

with the non-vanishing contributions to the Christoffel symbols equal to, when dropping small terms proportional to h,

$$\Gamma^{i}_{tt} \approx -\frac{1}{2}(\eta^{ij})\partial_j(\eta_{tt} + h_{tt}). \tag{2.21}$$

Since $h_{tt} = \frac{2GM}{r}$, equation 2.20 becomes, when using $\frac{dt}{d\tau} \approx 1$,

$$\frac{d^2\vec{x}}{dt^2} = -\frac{1}{2}\eta^{ij}\partial_j h_{tt} = -\vec{\nabla}\Phi, \tag{2.22}$$

reproducing the equations of motion for Newtonian gravity (equation 2.6).

The two requirements of general relativity: that laboratories in freely-falling reference frames should make the same measurements, and that the speed of light in vacuum is always the same, regardless of the reference frame leads to a geometric theory of spacetime. As described in chapter 2.1.3.1, the presence of mass or energy imposes curvature on spacetime; metric tensors are needed to easily describe coordinate systems in these curved spacetimes. Despite the increased sophistication of the general theory of relativity, it is straightforward to recover special relativity in the low-curvature limit and Newtonian gravity in the low-speed, low-curvature limit.

2.1.3.1 The Einstein Field Equations The Einstein field equations,

$$G_{\mu\nu} = 8\pi G T_{\mu\nu}, \tag{2.23}$$

determine, for a particular choice of coordinate system, the components of the metric $g_{\mu\nu}$ given a mass and energy distribution. Here, $G_{\mu\nu}$ is the Einstein tensor, given by

$$G_{\mu\nu} = R_{\mu\nu} - \frac{1}{2}R g_{\mu\nu} \tag{2.24}$$

with $R_{\mu\nu}$ the Ricci tensor

$$R_{\mu\nu} = \frac{\partial\Gamma^{\alpha}_{\mu\nu}}{\partial x^{\alpha}} - \frac{\partial\Gamma^{\alpha}_{\mu\alpha}}{\partial x^{\nu}} - \Gamma^{\alpha}_{\mu\nu}\Gamma^{\beta}_{\alpha\beta} - \Gamma^{\alpha}_{\mu\beta}\Gamma^{\beta}_{\nu\alpha} \tag{2.25}$$

and R the curvature scalar, that is, R^{μ}_{μ}. The Ricci tensor and curvature scalar encode the curvature of spacetime, with the Ricci tensor analogous to the change in volume of a body as it is moved along a geodesic through curved space. The curvature scalar compares the area of a hypersphere in flat space to its area in a

curved spacetime [17]. The stress-energy tensor is $T_{\mu\nu}$. Components of the stress-energy tensor describe the energy and momentum density and flux through a region and stresses from external forces applied on a body. For flat spacetimes, energy and momentum can be conserved by demanding that

$$\frac{\partial T^{\mu\nu}}{\partial x^{\nu}} = 0. \tag{2.26}$$

Equation 2.23 can be interpreted as "space tells matter how to move. Matter tells space how to curve" [14]. Metrics which solve the Einstein field equations for a particular configuration of stress-energy describe distances between events in a spacetime, allowing observables to be computed.

2.2 Gravitational Waves

2.2.1 Wave Solutions to the Einstein Field Equations

2.2.1.1 Linearized Gravity As demonstrated in equation 2.15 and the following discussion in chapter 2.1.3, it is fruitful to examine the behavior of this theory in the low-curvature regime. Here we adopt the metric of equation 2.15 and study the consequences of a small deviation from flat space in general relativity. To compute the Einstein tensor, the Ricci tensor and scalar will be needed, which in turn rely on the Christoffel symbol and the inverse metric of equation 2.15.

From properties of the matrix inverses, it is straightforward to determine that

$$g^{\mu\nu} = \eta^{\mu\nu} - h^{\mu\nu} \tag{2.27}$$

with

$$h^{\mu\nu} = \eta^{\mu\alpha}\eta^{\beta\nu}h_{\alpha\beta} \tag{2.28}$$

where higher-order term in h are neglected, as they are small. Using this, a Christoffel symbol can be computed using equation 2.13

$$\Gamma^{\alpha}_{\mu\nu} = \frac{1}{2}(\eta^{\alpha\beta} + h^{\alpha\beta})(\partial_{\mu}(\eta_{\nu\beta} + h_{\nu\beta}) + \partial_{\nu}(\eta_{\beta\mu} + h_{\beta\mu}) - \partial_{\beta}(\eta_{\mu\nu} + h_{\mu\nu})). \tag{2.29}$$

Since partial derivatives of $\eta_{\mu\nu}$ vanish, equation 2.29 simplifies to

$$\Gamma^{\alpha}_{\mu\nu} = \frac{1}{2}\eta^{\alpha\beta}(\partial_{\mu}h_{\nu\beta} + \partial_{\nu}h_{\beta\mu} - \partial_{\beta}h_{\mu\nu}) \tag{2.30}$$

when higher order terms in h are dropped. Furthermore, the products of Christoffel symbols found in the second half of the right hand side of equation 2.25 will depend on higher order terms in the perturbation from flat space and do not contribute to leading order. The linearized form of the Ricci tensor becomes

$$R_{\mu\nu} = \frac{1}{2}\big(- \frac{\partial^2 h}{\partial x^{\mu}\partial x^{\nu}} + \frac{\partial^2 h^{\alpha}_{\nu}}{\partial x^{\alpha}\partial x^{\mu}} + \frac{\partial^2 h^{\beta}_{\mu}}{\partial x^{\beta}\partial x^{\nu}} - \eta^{\alpha\beta}\frac{\partial^2 h_{\mu\nu}}{\partial x^{\alpha}\partial x^{\beta}}\big) \tag{2.31}$$

with h the trace of $h_{\mu\nu}$. The Ricci scalar is found via contracting equation 2.31 with the metric

$$R = g^{\mu\nu}R_{\mu\nu} \tag{2.32}$$

taking $g^{\mu\nu} \to \eta^{\mu\nu}$ to keep only the terms lowest order in h. This is

$$R = \frac{1}{2}\big(- \eta^{\mu\nu}\frac{\partial^2 h}{\partial x^{\mu}\partial x^{\nu}} + \eta^{\mu\nu}\frac{\partial^2 h^{\alpha}_{\nu}}{\partial x^{\alpha}\partial x^{\mu}} + \eta^{\mu\nu}\frac{\partial^2 h^{\beta}_{\mu}}{\partial x^{\beta}\partial x^{\nu}} - \eta^{\mu\nu}\eta^{\alpha\beta}\frac{\partial^2 h_{\mu\nu}}{\partial x^{\alpha}\partial x^{\beta}}\big) \tag{2.33}$$

. Note that the final term in equation 2.33 is the partial derivative of the trace of $h_{\mu\nu}$ and that the middle two terms consist only of sums over dummy indices. Consequently the middle two terms are identical quantities and equation 2.33 reduces to

$$R = -\eta^{\mu\nu}\frac{\partial^2 h}{\partial x^{\mu}\partial x^{\nu}} + \frac{\partial^2 h^{\mu\nu}}{\partial x^{\mu}\partial x^{\nu}} \tag{2.34}$$

when these identifications are made. A further simplification is made by identifying the d'Alembertian operator,

$$\Box = -\frac{\partial^2}{dt^2} + \frac{\partial^2}{dx^2} + \frac{\partial^2}{dy^2} + \frac{\partial^2}{dz^2} \tag{2.35}$$

in Cartesian coordinates, as $\Box = \partial^\alpha \partial_\alpha = \eta^{\alpha\beta}\partial_\alpha\partial_\beta$. The Einstein tensor for linearized gravity is thus

$$G_{\mu\nu} = \frac{1}{2}\Big(- \frac{\partial^2 h}{\partial x^\mu \partial x^\nu} + \frac{\partial^2 h^\alpha_\nu}{\partial x^\alpha \partial x^\mu} + \frac{\partial^2 h^\beta_\mu}{\partial x^\beta \partial x^\nu} - \Box h_{\mu\nu} + \eta_{\mu\nu}\Box h - \eta_{\mu\nu}\frac{\partial^2 h^{\alpha\beta}}{\partial x^\alpha \partial x^\beta}\Big) \tag{2.36}$$

This expression can be further simplified by rewriting it in terms of the trace-reversed perturbation tensor

$$\bar{h}_{\mu\nu} = h_{\mu\nu} - \frac{1}{2}\eta_{\mu\nu}h \tag{2.37}$$

where $\bar{h} = -h$, 2.36 becomes, after some index manipulation,

$$G_{\mu\nu} = \frac{1}{2}\eta_{\nu\gamma}\frac{\partial^2 \bar{h}^{\alpha\gamma}}{\partial x^\alpha \partial x^\mu} + \frac{1}{2}\eta_{\mu\gamma}\frac{\partial^2 \bar{h}^{\beta\gamma}}{\partial x^\beta \partial x^\nu} - \frac{1}{2}\eta_{\mu\nu}\frac{\partial^2 \bar{h}^{\alpha\beta}}{\partial x^\alpha \partial x^\beta} - \frac{1}{2}\Box \bar{h}_{\mu\nu}. \tag{2.38}$$

2.2.1.2 Lorenz Gauge This simpler form of the linearized gravity Einstein tensor suggests that solutions to Einstein field equations may involve only a wave equation in the trace-reversed perturbation. But first, terms which depend on divergences of the trace-reversed perturbation would have to vanish to leave only a single term. We examine the behavior of $\bar{h_{\mu\nu}}$ under arbitrary coordinate transformations to determine the conditions under which derivatives of the trace-reversed perturbation vanish. For an arbitrary coordinate transformation of the form

$$x'^\mu = x^\mu + \xi^\mu \tag{2.39}$$

the metric in the primed coordinate system is

$$g'_{\mu\nu} = \frac{\partial x^\alpha}{\partial x'^\mu}\frac{\partial x^\beta}{\partial x'^\nu} g_{\alpha\beta}. \tag{2.40}$$

Equation 2.39 can be inverted to find the form of the partial derivative terms. Keeping only leading order terms in $h_{\mu\nu}$ and ξ^{μ}, the metric in the primed coordinate system is, in terms of the old coordinate system,

$$g'_{\mu\nu} = \eta_{\mu\nu} - \frac{\partial \xi_{\mu}}{\partial x^{\nu}} - \frac{\partial \xi_{\nu}}{\partial x^{\mu}} + h_{\mu\nu}. \tag{2.41}$$

From the definition of the linearized metric, this leads immediately to an expression for the small perturbation in terms of the original coordinates:

$$h'_{\mu\nu} = h_{\mu\nu} - \frac{\partial \xi_{\mu}}{\partial x^{\nu}} - \frac{\partial \xi_{\nu}}{\partial x^{\mu}}. \tag{2.42}$$

Lastly, from here, an expression for the trace-reversed polarization tensor can be found. It is

$$\bar{h}'_{\mu\nu} = \bar{h}_{\mu\nu} - \frac{\partial \xi_{\nu}}{\partial x^{\mu}} - \frac{\partial \xi_{\mu}}{\partial x^{\nu}} + \eta_{\mu\nu}\frac{\partial \xi_{\beta}}{\partial x_{\beta}}. \tag{2.43}$$

All terms on the right hand side of equation 2.38, except the term containing the d'Alembertian, will vanish if $\frac{\partial \bar{h}^{\mu\nu}}{\partial x^{\mu}} = 0$. Suppose this condition is true in the primed coordinate system. What form does this impose on ξ^{μ} so that it is always possible to find a coordinate system where derivatives of the perturbation vanish by performing the transformation of equation 2.39? Taking the derivative of equation 2.43 and setting it equal to zero yields

$$0 = \frac{\partial \bar{h}^{\mu\nu}}{\partial x^{\mu}} - \Box \xi_{\nu} - \frac{\partial^2 \xi^{\mu}}{\partial x^{\mu} \partial x_{\nu}} + \frac{\partial^2 \xi^{\beta}}{\partial x_{\nu} \partial x^{\beta}} \tag{2.44}$$

. The final two terms cancel one another, so ξ^{μ} belong to the family of functions which solve the differential equation

$$\xi^{\mu} = \frac{h^{\mu\nu}}{\partial x^{\nu}}, \tag{2.45}$$

to which the homogeneous solution, $\Box \xi^{\mu} = 0$ may always be added. Thus coordinate systems that satisfy the Lorenz gauge condition (equation 2.45) can be related to other Lorenz gauge satisfying coordinate systems by applying coordinate

transformations which solve this homogeneous form of the differential equation. Therefore, if the primed coordinates respect Lorenz gauge, it is possible to find a transformation to a new coordinate system where Lorenz gauge is still respected with an appropriate choice of ξ^μ.

Working in Lorenz gauge, the Einstein tensor is simply

$$G_{\mu\nu} = -\frac{1}{2}\Box\bar{h}_{\mu\nu} \tag{2.46}$$

and the Einstein field equations are

$$-\Box\bar{h}_{\mu\nu} = 16\pi G T_{\mu\nu}. \tag{2.47}$$

This simple approximation for small spacetime curvatures has profound consequences for modern astronomy and cosmology.

2.2.1.3 Gravitational Waves In vacuum with no energy or momentum flux, all components of the stress-energy $T_{\mu\nu}$ vanish. Therefore, solutions to the Einstein equations in vacuum are those which satisfy

$$-\Box\bar{h}_{\mu\nu} = 0. \tag{2.48}$$

Nontrivial solutions to these equations take the form of plane waves with wavevector k_μ, or

$$\bar{h}_{\mu\nu} = C_{\mu\nu}e^{ik_\alpha x^\alpha}. \tag{2.49}$$

Working in coordinates where the trace of $C_{\mu\nu}$ vanishes, and the Lorenz gauge condition is satisfied, the exact form of $C_{\mu\nu}$ and k_μ become tractable [18]. In this coordinate system, which can be reached from any other satisfying Lorenz gauge with appropriate choice of ξ^μ, the wavevector takes the form

$$k_\mu = (-\omega, 0, 0, \omega) \tag{2.50}$$

and symmetry, trace and gauge considerations reduce the amplitude tensor to

$$C_{\mu\nu} = \begin{pmatrix} 0 & 0 & 0 & 0 \\ 0 & C_{11} & C_{12} & 0 \\ 0 & C_{12} & -C_{11} & 0 \\ 0 & 0 & 0 & 0 \end{pmatrix}. \tag{2.51}$$

Note that in these coordinates $\bar{h}_{\mu\nu} = h_{\mu\nu}$.

This describes a plane wave traveling in the x^3 direction. Like waves in vacuum in electromagnetism, the plane waves propagate in one spatial direction, but the fluctuations are orthogonal to the direction of propagation. For a monochromatic plane wave in vacuum in transverse-traceless gauge, there are only two degrees of freedom: the two unique, nonzero components of the tensor in equation 2.51. By convention, these unique coefficients describe the amplitudes of plus- and cross-polarized fluctuations. That is, by convention, $C_{11} = h_+$ and $C_{12} = h_\times$.

The geometric treatment and unification of space and time in general relativity means that matter and energy can deform spacetime from flat Minkowski space via gravitation. When solving for small deviations from flat spacetime, the structure of the underlying equations and gauge concerns permit propagating solutions to the Einstein equations. These GWs are quadrupolar stretching and squeezing of spacetime. The action of an GW on a ring of test particles is shown in figure 1.

2.2.2 Astrophysical Sources of Gravitational Waves The particular matter and energy content of a region of spacetime, encoded by $T_{\mu\nu}$, can act as a source of GWs. In general, a spacetime with stress-energy tensor $T^{\alpha\beta}$ will produce

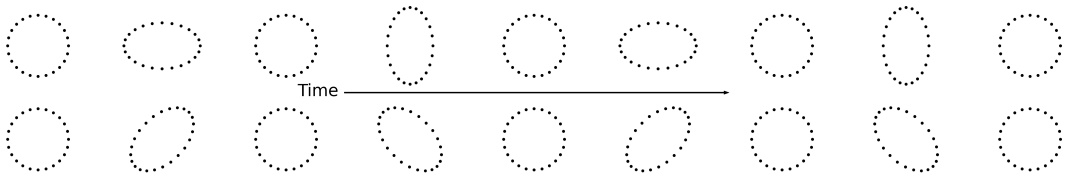


Figure 1. The reaction of two rings of freely-falling test particles to a passing GW. The GW is propagating in the direction orthogonal to the surface of the page. The top ring is affected by a completely +-polarized GW while the bottom ring is affected by a completely ×-polarized GW.

perturbations on top of flat spacetime according to

$$h^{\bar{\mu}\nu}(x^\alpha) = 4\int d^3x' \frac{T^{\mu\nu}(t - |x^i - x^{i\prime}|)}{|x^i - x^{i\prime}|}. \tag{2.52}$$

Working in the radiation zone, that is a distance r away from the GW source with r much larger than the characteristic size of the source, this simplifies to

$$h^{\bar{\mu}\nu}(x^\alpha) \sim \frac{4}{r}\int d^3x' T^{\mu\nu}(t - r, x^{i,\prime}). \tag{2.53}$$

Enforcing equation 2.26 yields the identity

$$\int d^3x T^{ij}(x^k) = \frac{1}{2}\frac{d^2}{dt^2}\int d^3x x^i x^j T^{00}(x^k), \tag{2.54}$$

and in the low-energy radiation zone the stress-energy tensor tends towards the non-relativistic limit, i.e. $T^{00} \sim \mu x^k$, with $\mu(x^k)$ the rest-mass density. The integral on the left of equation 2.54, in this limit, simplifies to the definition of the second moment of the mass. Hence, far from a weak source of GWs, the amplitude of perturbations go as

$$h^{ij}(\bar{x^\mu}) = \frac{2}{r}\ddot{I}^{ij}(t - r). \tag{2.55}$$

Therefore, arrangements with non-vanishing second time derivatives of the quadrupolar mass moment are sources of GWs. The following sections discuss relevant astrophysical sources of GWs.

2.2.2.1 *Compact Binary Coalescences*

A CBC is a system of two compact objects (NSs and/or BH) orbiting one another which, over time, lose angular momentum through GW emission and eventually inspiral and collide with one another. To leading post-Newtonian order, the energy loss rate from GW emission for compact objects with masses m_1 and m_2 in a circular orbit separated by a distance r is [19]

$$\frac{dE}{dt} = -\frac{32G^4}{5}\frac{m_1^2 m_2^2 (m_1 + m_2)}{r^5}. \tag{2.56}$$

The decrease in orbital period corresponding to energy loss via GW emission was first observed in the binary neutron star (BNS) system PSR B1913+16 [20, 21]. The observation of a shortening orbital period represents the first indirect detection of GWs. Further observations of the system measured other general relativistic effects, such as the Shapiro delay and small corrections to the shapes of the binary's orbits [22]. This BNS pair should inspiral into one another in approximately 300 million years [23].

When a pair of compact objects draw near each other before merger, more and more orbital energy is converted to GW emission due to the strong dependence of equation 2.56 on the separation of the two bodies. The Laser Interferometric Gravitational-Wave Observatory (LIGO), Virgo and Kamioka Gravitational Wave Detector (KAGRA) detectors are designed to observe GWs from CBCs in the final minutes to seconds of their inspiral prior to coalescence [24–26]. A more thorough description of these facilities is given in chapter . The LIGO-Virgo-KAGRA network is best-suited to observe GWs from CBCs composed of $\sim$ 1–100 $M_\odot$ compact objects [27].

The era of GW astronomy truly began with the direct detection of GWs from the inspiral and merger of a 36^{+5}_{-4} $M_\odot$ BH and a 29^{+4}_{-4} $M_\odot$ BH made by

the LIGO detectors on September 14, 2015 [28]. The observation of this merger provided a new opportunity to test the foundations of general relativity in the strong-field and no deviation from the predictions of general relativity were observed [29]. From this single detection, the formation scenarios for and merger rates for tens of solar mass binary black hole (BBH) systems were constrained [30, 31]. An extensive follow-up campaign was also conducted with neutrino [32] and electromagnetic [33] observatories, although this was limited by the poor sky localization (~ 600 deg^2) of the event from the GW data.

GW150914 was discovered at the beginning of LIGO's first observing run (O1), which ran from September 12, 2015 to January 19, 2016 [34, 35]. During this observing campaign, one additional GW was detected with high significance as well as a third signal with a high likelihood of astrophysical origin, but not enough statistical significance to unambiguously claim a detection [36]. This final signal was "promoted" to GW status at the conclusion of second observing run (O2), when a reanalysis of the data using an improved two-detector ranking statistic as well as better understanding of the noise background of the LIGO detectors [37]. These additional detections were also CBCs containing two BHs.

After the conclusion of O1, the LIGO detectors were taken offline for a period of detector improvements and conditioning. Improved optics and suspension components were installed and environmental noise isolation efforts were undertaken in this period [37, 38]. Consequently, the astrophysical reach of the LIGO detectors improved between the observing runs. The astrophysical sensitivity usually expressed in terms of the BNS range: the distance at which two colliding 1.4 $M_\odot$ NSs would be detected with an signal-to-noise ratio (SNR) of 8 [39, 40]. Thanks to detector improvements, the best BNS ranges achieved by the LIGO

detectors improved from ∼80 Mpc in O1 to over 100 Mpc by the conclusion of O2 [41].

O2 was conducted from November 30, 2016 to August 25, 2017. The Advanced Virgo detector joined LIGO in searching for GWs in August 1, 2017. O2 saw the detection of 8 GWs from CBCs [37]. This includes the first three-detector observation of GWs from a BBH merger. Including data from the Virgo detector reduced the sky localization for the GW source by a factor of 19.3 compared to the sky localization reconstructed based on LIGO data alone [42]. Notably, O2 also includes the first detection of GWs from a BNS merger: GW170817 [43]. A gamma-ray burst (GRB) arrived at Earth coincident with the GWs observed by the LIGO-Virgo network [44]. The sky location constraints inferred from the combined GW and electromagnetic data resulted in confident identification and observation of the kilonova formed from the BNS merger across the electromagnetic spectrum [45]. Radio observation of the source continued for more than four years post-merger [46]. The identification of the host galaxy of GW170817, NGC 4993, led to a distance-ladder-free determination of the Hubble constant as well as tests of the speed of gravity and the number of spacetime dimensions [44, 47, 48]. The non-observation of tidal deformation of the nuclear matter during the final phase of the inspiral also provided new constraints on NS structure [49].

Once again, the detector network was shut down for a period of improvements prior to the start of O3. Along with replacements made to optics and suspensions and commissioning to support increased circulating laser power [50], this break saw the realization of an in-vacuum frequency-dependent squeezed vacuum source used to reduce shot noise [51].

O3 began on April 1, 2019 and concluded on March 27, 2020 with a month-long break for detector commissioning during October 2019. 79 GWs with a high probability of astrophysical origin were observed [52–54]. Noteworthy detections from this observing run include: two observations of BHs colliding with much lighter secondary objects [55, 56], an extremely light CBC with total source frame mass of $3.4^{0.3}_{-0.1}$ $M_\odot$ [57], and a merger where the remnant BH was heavy enough to fall into the pair-instability mass gap, a mass range where a dearth of BHs is expected due the suppression of outward radiation pressure from nuclear burning via electron-positron pair production [58, 59]. For the first time, the LIGO-Virgo network observed neutron star-black hole (NSBH) coalescences in the early days of 2020 [60]. No electromagnetic counterparts were observed in conjunction with the O3 GW events. The large increase in the number of CBCs seen in O3 in comparison to the prior observing runs permitted detailed study of the mass distribution, spin distribution of merging compact objects [61, 62]. Due to scheduling complications introduced by the Covid-19 pandemic, KAGRA did not participate in a joint observing campaign with the LIGO-Virgo detector network, as planned. However, KAGRA did operate in concert with the GEO 600 GW observatory in the month following the end of O3 [63].

Following O3, the detectors again underwent a period of upgrades prior to the start of O4. Important detector configuration changes made during this period include replacing optics which had developed point absorbers [64] and support for higher input laser power [65, 66]. A filter cavity was constructed and instrumented to realize frequency-independent squeezed vacuum state injection to further reduce noise [67]. The effects of these improvements are illustrated by the 1-5+$\times$ reduction

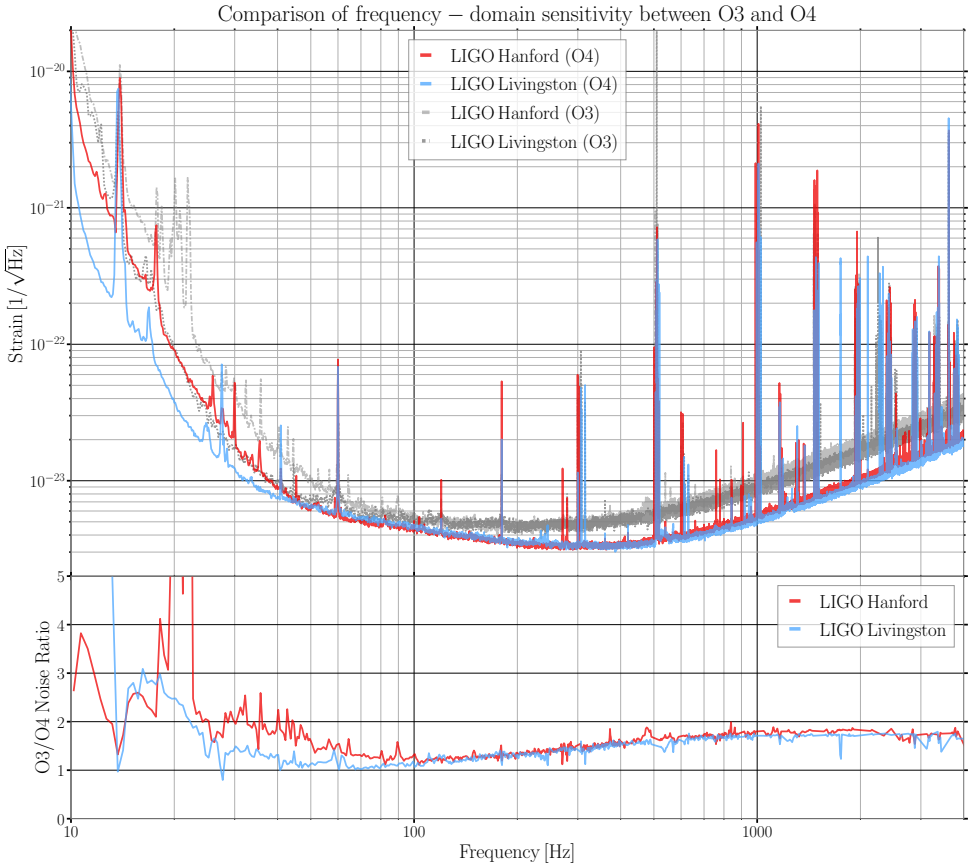


Figure 2. A comparison between of each LIGO detector's noise sensitivity in O3 and O4a [68].

each detector's strain amplitude spectral density (ASD) below 100 Hz and 1-2× reduction in strain ASD above 100 Hz shown in figure 2.

The O4 began on May 24, 2023 and is ongoing at the time of writing. The LIGO detectors were briefly joined by KAGRA before KAGRA halted observing for a long period of commissioning. In 2024, the Virgo detector joined the LIGO detectors in a joint observing campaign. The total number of GWs from CBCs has nearly tripled since O3 thanks to the improved sensitivity of the LIGO-Virgo-

KAGRA network. Figure 3 shows the number of GWs detected in each observing run. While analysis of events is ongoing, the most significant single detection of O4 has been a CBC where the identity of the primary mass is unknown. It is either a NSBH with the lightest-mass BH ever observed or a BNS with the heaviest NS ever observed [69].

In the searches described above, the primary method, "pipelines," for identifying GWs employ matched filter methods comparing frequency-domain strain data from one of more interferometers $h(f)$ with multiple templates—predictions for the functional form of GW strain produced by numerical relativity studies—to produce an SNR timeseries for a given template $t(f)$ via [15]

$$\rho(t) = 4 \int_{f_{\text{low}}}^{f_{\text{high}}} \frac{h(f)t^*(f)}{S_n(f)} df \tag{2.57}$$

where $S_n(f)$ is an interferometer's single-sided noise power spectral density (PSD) and the * denotes the complex conjugate. Templated search algorithms used in O4 include GstLAL [70], MBTA [71], PyCBC [72] and SPIIR [73].

2.2.2.2 Other Transient Phenomena While there are many search pipelines for the inspiral and merger of 1-100 $M_\odot$ quasicircular CBCs, these CBCs are just a subset of the possible GW sources detectable by the LIGO-Virgo-KAGRA network. Short GW transients from non- or extraordinary CBC sources are typically classed as GW "bursts." Some example sources of GW burst sources are highlighted below. An extended discussion of GW bursts from CSs is found in chapter 2.2.2.5

Due to difficulties computing a deep enough template bank and the short merger timescale compared to the CBCs of chapter 2.2.2.1, mergers involving hundreds of $M_\odot$ are better recovered by either targeted template-bank based searches [74] or generic searches for coherent power between two or more GW

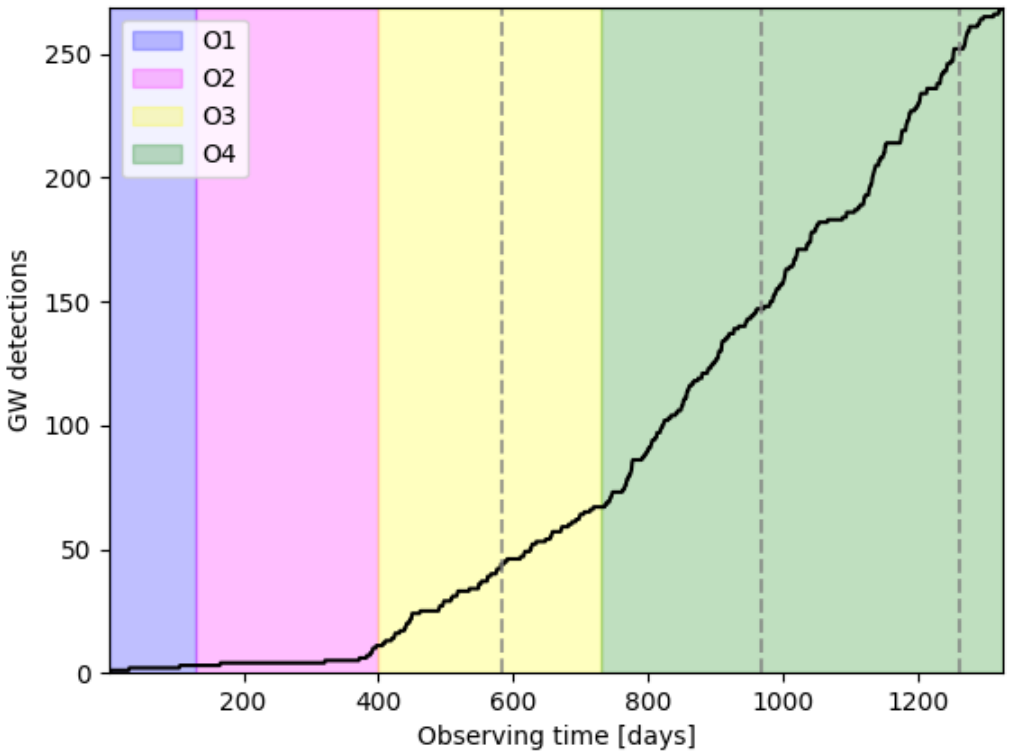


Figure 3. The number of GW events confidently detected by LIGO through the first three observing runs and part of O4. The colored background differentiates between observing runs and the vertical dashed lines denote the positions of planned intra-run detector commissioning breaks. These breaks subdivide the last two observing runs into multiple parts, i.e. O3a/O3b and O4a/O4b/O4c. Detection counts and dates were drawn from [37] for O1 and O2 observations and non-retracted events appearing in the Gravitational-wave Candidate Event Database (GraceDB) for O3 and O4. This plot includes observations through April 1, 2025, at which point the LIGO detectors were taken offline for a short period of commissioning, upgrading and repairs.

detectors. The latter method is used by the cWB search pipeline [75]. A dearth of templates for eccentric BH mergers means that these too are covered by unmodeled searches [76].

Supernovae are potential sources of GWs. During the engineering run prior to the start of O4 supernova SN2023ixf was discovered in the nearby galaxy Messier 101 [77]. Despite the LIGO detectors being operational for much of the time period surrounding the supernova, GWs from SN2023ixf were not observed [78]. A more realistic GW detection scenario would involve a galactic supernova, but the low ($\sim$1/century) rate of galactic supernova makes this unlikely.

The same processes which produce GRBs and fast radio bursts may also produce GWs. Dedicated searches for GWs around times of GRBs and fast radio bursts identified by electromagnetic observers have been carried out by the LIGO-Virgo-KAGRA network [79, 80], but GW170817 so far remains exceptional in the observation of both electromagnetic and gravitational radiation.

In addition to physically-motivated searches for unmodeled GW transients, searches for generic signal morphologies, such as band-limited white noise bursts and sine-Gaussian wavelets are conducted [81].

2.2.2.3 Continuous Gravitational Waves While the previously discussed sources of GW are transient features in detector data, disappearing as soon as the compact objects have merged, continuous GWs are long-lived, monochromatic sources of gravitational radiation. These include the GWs observed indirectly in [21]. Other sources of continuous GWs include non-axisymmetric internal mass distributions or topographical features occurring in the known pulsar and hypothesized galactic center NS populations [82, 83]. Directed searches for continuous GWs from the NSs of Scorpius X-1 and the NS remnants of the

Cassiopeia A and Vela Jr. supernovae have also been conducted [84, 85]. None of these searches have yet found continuous GWs.

2.2.2.4 The Stochastic Gravitational Wave Background The stochastic GW background consists of the superposition of GWs from all these and other sources. The magnitude of the stochastic GW background is typically parameterized in terms of the energy density of GWs per frequency bin:

$$\Omega_{GW}(f) = \frac{f}{\rho_c}\frac{d\rho_{GW}}{df} \tag{2.58}$$

with ρ_c the critical density. Searches for a stochastic GW background with the LIGO-Virgo-KAGRA network involve cross-correlating and Wiener filtering data from multiple detectors. The most stringent limits for the mass-energy density of the GW background given by O3 data is $\Omega_{GW} \leq 5.8 \times 10^{-9}$ at 25 Hz [86]. The pulsar timing array (PTA) NANOGrav [87, 88] observatory, in conjunction with the International Pulsar Timing Array [89], detected a correlated process governing the timing residuals of pulsars consistent with a GW background with energy density $9.3^{5.8}{-}4.0 \times 10^{-9}$ in the nHz frequency band in 2023 [90].

2.2.2.5 Cosmic Strings CSs are one-dimensional topological defects resulting from one or more spontaneous symmetry breaking phase transitions in the early universe [91, 92]. Spontaneous symmetry breaking is a generic process which appears in numerous physically relevant scenarios [93]. Well-studied examples, such as radiative corrections to abelian Higgs Lagrangians, feature characteristic energy scales below which symmetries are broken, but above which they are restored [94]. SU(5) or SO(10) grand unified theories, for example, reduce to the Standard Model in the low-energy limit, but may feature topological defect-forming symmetry breakings [92, 95]. In general, should the collection of vacua in a theory featuring hidden symmetries be nontrivial, CSs can be formed. The mass per unit length μ of

strings is proportional to the square of the vacuum expectation value prescribed by the theory.

Should CSs exist, they should encode information about high-energy extensions of the Standard Model. There are a number of ways that they may be detected; of particular relevance is their GWs signature. The geometry of spacetime around a CS is reviewed to show how observable gravitational and electromagnetic consequences emerge. For a static, straight string the stress-energy tensor is

$$T^{\nu}_{\mu} = \begin{pmatrix} \mu\delta(x)\delta(y) & 0 & 0 & 0 \\ 0 & 0 & 0 & 0 \\ 0 & 0 & 0 & 0 \\ 0 & 0 & 0 & \mu\delta(x)\delta(y) \end{pmatrix}. \tag{2.59}$$

Working in Lorenz gauge, equation 2.47 is solved by $h_{11} = h_{22} = 8G\mu\ln(\sqrt{x^2+y^2}/r_0)$ with all other components of the perturbation vanishing [96]. Here r_0 is simply a constant of integration. The string tension, $G\mu$, a useful quantity to characterize these objects appears here. The effect of a CS on spacetime is more apparent in cylindrical coordinates. The metric tensor with the addition of the string-induced perturbation is

$$ds^2 = -dt^2 + (1-h)(dr^2 + r^2 d\theta^2) + dz^2 \tag{2.60}$$

with $h = 8G\mu\ln(\sqrt{x^2+y^2}/r_0) = 8G\mu\ln(r/r_0)$. With the substitutions $(1-h)dr^2 \to dr'^2,\ (1-h)r^2 \to (1-8G\mu)r'^2$, the metric becomes

$$ds^2 = -dt^2 + dr'^2 + (1-8G\mu)r'^2 d\theta^2 + dz^2. \tag{2.61}$$

To leading order in $G\mu$, this takes a pseudo-Minkowskian form under the substitution $\theta \to (1-4G\mu)\theta',\ d\theta \to (1-4G\mu)d\theta'$. In the region near the string,

spacetime is indistinguishable from flat spacetime, that is

$$ds^2 = -dt^2 + dr'^2 + r'^2 d\theta^2 + dz^2. \tag{2.62}$$

A consequence of the second pair of substitutions to recover flat-looking spacetime, however, is to restrict the domain of the angular variable: while θ ran from 0–2π, θ' is restricted to the domain 0–$2\pi - 8\pi G\mu$. The effect of a CS is to impose a globally conical geometry on spacetime with deficit angle $8\pi G\mu$. A full general relativistic treatment of the straight string geometry finds the same result for $G\mu << 1$ [92].

The Nambu-Goto action for thin strings with radii of curvature much larger than their thickness dictates string dynamics [97, 98]. In the usual worldsheet parameterization, the string is represented as a two-dimensional object in spacetime with $x^\mu = x^\mu(\zeta^a)$ with ζ^0 timelike and ζ^1 spacelike. Analogous to the metric tensor, the worldsheet metric is

$$\gamma_{ab} = g_{\mu\nu} \frac{\partial x^\mu}{\partial \zeta^a} \frac{\partial x^\nu}{\partial \zeta^b}. \tag{2.63}$$

The Nambu-Goto action in this parameterization is

$$S = -\mu \int \sqrt{-\det \gamma_{ab}}\, d^2\zeta. \tag{2.64}$$

The equations of motion in flat space are

$$\partial_a \big(\sqrt{-\det \gamma_{ab}}\, \gamma^{ab} \frac{\partial x^\mu}{\partial \zeta^b} \big). \tag{2.65}$$

A useful gauge for the following discussion is the gauge in which both the off-diagonal components and trace of γ_{ab} vanish. Inserting the definition of the worldsheet into these gauge conditions leads to the equations

$$\dot{x}x' = \dot{x}^2 + x'^2 = 0 \tag{2.66}$$

with dots representing differentiation with respect to ζ^0 and primes ζ^1. In this setup, the equations of motion reduce to

$$\ddot{\vec{x}}^{\mu} - \vec{x}^{\mu\prime\prime} = 0 \tag{2.67}$$

when the transverse string gauge is used [92]. The three-vector $\vec{x}$ describes the trajectory of the string and is function of the timelike and spacelike ζ parameters. General solutions to equation 2.67 take the form of arbitrary vector functions describing trajectories in the positive and negative spacelike directions

$$\vec{x} = \frac{1}{2}(\vec{a}(\zeta^1 - t) + \vec{b}(\zeta^1 - t)). \tag{2.68}$$

Although these functions are arbitrary, specifying the gauge imposes conditions on relations between between them or their derivatives [92]. Imposing these conditions and evaluating equation 2.68 at $\zeta^0 = 0$ gives the shape of the string as

$$\vec{x}(\zeta^1, 0) = \frac{1}{4}(\vec{a}(\zeta^1)'' + \vec{b}(\zeta^1)'')\zeta^1 \times \zeta^1 \tag{2.69}$$

to leading order in the spatial derivatives. At points where the sum of second spatial derivatives of the string shape functions is nonzero, the string develops a cusp.

At cusps, the trajectory of the CS doubles back on itself. At that point, the velocity of the string goes to the speed of light [99]. Through self-interaction or collisions with other strings, kinks—special points along the string where the first spatial derivative of the $\vec{a}$ and $\vec{b}$ functions are discontinuous—can be formed [100]. These kinks can propagate along the loop trajectory.

These special points, cusps and kinks, are powerful emitters of GWs. Cusps emit bursts of GWs in a narrow beam orthogonal to the string trajectory [101, 102]. Kinks emit wider, fan-shaped patterns of GWs [103]. When two kinks on a loop collide with one another, they resulting kink-kink collision emits a burst of

GWs isotropically [104, 105]. The GW strains produced via these three emission modalities all follow a similar functional form:

$$\tilde{h}(f) = A(\ell, z) f^{-q}. \tag{2.70}$$

The GW signal amplitude is [106]

$$A(\ell, z) = g_{1,\ i} \frac{G\mu\ell^{2-q}}{(1+z)^{q-1} r(z)} \tag{2.71}$$

with ℓ the CS loop size, z the redshift to the emitter and $r(z)$ the comoving distance to the source, $g_{1,i}$ a numerical factor $\mathcal{O}(0.1)$ whose value depends on the emitter, and q_i—the power law index in equation 2.70—is 4/3 for cusps, 5/3 for kinks or 2 for kink-kink collisions.

The geometry of the emissions imposes a high-frequency cutoff f_h on cusp and kink emissions, as the opening angle of the beam or fan is inversely proportional to to GW frequency [106]. In addition to the fundamental low-frequency cutoff on GW emission, $f > 2/\ell$, in practice, GW observatories have a minimum frequency, f_l, above which they are sensitive to astrophysical signals much greater than this limit. Equation 2.70 is thus taken to be

$$\tilde{h}(f) = A(\ell, z) f^{-q} \Theta(f_l < f < f_h) \tag{2.72}$$

where equation 2.71 is unchanged.

The non-detection of GWs from CSs [106–109] allows smaller and smaller limits on the string tension, and thus more stringent constraints on beyond the Standard Model physics of the early universe. So far, constraints are set for specific loop distribution models, which describe the size and number density of CSs loops.

CHAPTER III

GRAVITATIONAL WAVE INTERFEROMETRY

> *"O king of time and substance and cipher of the century! In Babylonia didst thou attempt to make me lose my way in a labyrinth of brass with many stairways, doors, and walls; now the Powerful One has seen fit to allow me to show thee mine, which has no stairways to climb, nor doors to force, nor wearying galleries to wander through, nor walls to impede thy passage."*
>
> —Jorge Luis Borges, *The Two Kings and the Two Labyrinths* [110]

Sections 3.3.2 and 3.3.3, with the exception of 11, of this chapter were published in volume 41 of Classical and Quantum Gravity in April, 2025 [65]. Siddharth Soni organized the writing of the publication on behalf of the LIGO Instrument Science/Detector author list. Individual section writing and analyses that appear in the paper was led by a team of 22 authors, including Siddharth Soni and myself. 43 additional scientists helped with analyses appearing in the text. The additional authors beyond these 65 did not directly contribute to the work, but provided commissioning, computing, noise investigation or other support for one or more of the LIGO sites during the preparations for or during O4a.

I wrote the text of section 3.3.2 and helped design the weekly magnetic injection routine described therein prior to O4a. I used the PEMcoupling codebase [111, 112] to identify the weekly variation in magnetic coupling at LIGO Hanford Observatory (LHO) and produced the figure used in the paper. Samantha Callos and Robert Schofield conducted an unsuccessful search for the cause of the variation.

I wrote the text of section 3.3.3 and used PEMcoupling to analyze acoustic and shaker injections in the vicinity of the pre-stabilized laser (PSL) which

were organized by myself, Anamaria Effler and Robert Schofield prior to O4a. The later injections at lower input power were made by Lance Blagg, Genevieve Connolly and Robert Schofield, but I analyzed the injections and compared them to their 75 W counterparts.

3.1 Gravitational Wave Interferometery

3.1.1 Detection Principles As illustrated in figure 1, a passing GW may be observed by repeatedly measuring the distance between multiple test masses sufficiently isolated from their local environment. In principle, any time-varying change in the distance between these masses is evidence for a GW. For a GW with amplitude A, frequency f, and phase ϕ, the change in distance between two test masses oriented in such a manner as to maximize the distance change when considering the polarization and direction of propagation of the GW is [13]

$$\frac{\Delta L}{L} = \frac{1}{2} A \sin(2\pi f t + \phi) \tag{3.1}$$

if the two masses are separated by a distance L when unperturbed. The GW strain, $\frac{\Delta L}{L}$, varies sinusoidally in time due to the passing GW. Confidence in detections can be improved by assembling a network of spatially-separated test masses so that fluctuations in the inter-mass distance from local environmental effects can be identified and discarded.

Initial attempts to directly detect GWs looked for mechanical modes in metal bars or cavities excited by passing GWs [113]. However, technical, historic, scientific and cost considerations have led to this method to be largely superseded by interferometric techniques for direct GW detection. In the interferometric approach, the test masses are optical components and resonant optical cavities bounded by these test masses are affected by passing GWs.

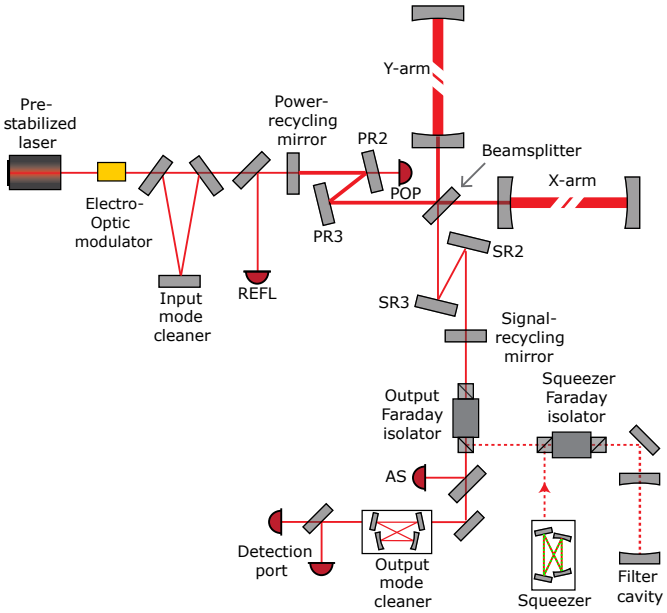


Figure 4. A sketch of the optical layout of a LIGO detector [66].

3.1.2 Interferometry in Practice The first dedicated GW interferometer was a single-arm laser strainmeter with a 30-meter cavity length engineered to search for the continuous GW signal emitted by the Crab pulsar [114]. Decades of development in GW interferometry, summarized in [115], culminated in the construction of the LIGO facilities: a pair of dual-recycled Fabry-Pérot Michelson interferometers located near Hanford, Washington, United States and Livingston, Louisiana, United States. A diagram of the layout of a single LIGO detector is shown in figure 4.

Input light for the LIGO detectors is produced by a 2 W non-planar ring oscillator with an Nd:YAG crystal which produces infrared light with a wavelength of 1,064 nm [116]. Its power is then increased by a series of amplifiers before being passed via a periscope from the PSL enclosure optics table into vacuum and 9 and 45 MHz sidebands are added to the signal. The input mode cleaner spatially filters out higher-order TEM modes from the beam. Circulating power

in the input beam is increased in the power recycling cavity before it is sent by the beamsplitter to two perpendicular, four km long arms [117]. These arms are bounded be fused silica mirrors which are supported by quadruple pendulum suspensions. The signal recycling cavity contains another mirror to increase the useful bandwidth of the detector. The output mode cleaner again filters out higher-order modes in the recombined beam. Squeezed light is injected into the output beam to reduce the effect of quantum shot noise on the signal [51, 67]. Finally, the light falls on photodiodes. The laser power incident on the photodiodes depends on the difference in arm length of the two 4 km cavities. A time-varying signal in the photodiodes could be evidence of the arms stretching and shrinking in response to a passing GW. The two LIGO detectors, LHO and LIGO Livingston Observatory (LLO), are separated by thousands of km, reducing correlated noise sources and providing additional verification that an astrophysical GW signal was observed. Their design is identical, although the two differ slightly in their as-built realizations.

3.2 Detector Noise

3.2.1 Quantum and Thermal Noise Typical GW strain amplitudes for CBCs observed by LIGO are $\mathcal{O}(10^{-21})$ or smaller, corresponding to a differential arm length (DARM) of $\mathcal{O}(10^{-17})$ m. Consequently, even small sources of noise can have large effects on detector sensitivity. Quantum and thermal noise represent the most deleterious modeled noise sources in O3 and O4 [50, 66].

Quantum noise arises from shot noise and radiation pressure noise. Especially at higher frequencies, statistical variation in the arrival time of individual photons in a wavefront contributes to shot noise. Higher input power decreases the effect of shot noise. Quantum radiation pressure noise stems from

fluctuations in amplitude of the electric field in the arm cavities and is most significant at lower frequencies. Both sources of quantum noise are decreased by frequency-dependent squeezing. At low frequencies, amplitude-squeezed light is injected into the detctor arm cavities, modifying the coherent vacuum state in the arms. This reduces the quantum amplitude fluctuations seen by the test masses in the arms. At high frequencies, phase-squeezed light is injected, which lessens quantum phase fluctuations of the beam, lowering shot noise.

Towards the middle of LIGO's frequency range, thermal noise is the limiting noise source in O4. Normal modes of vibration in optical components and their suspensions are naturally excited by the surrounding thermal environment. Brownian motion of the atoms the optical coatings on the exterior of the test masses also contributes to the overall thermal noise performance of the interferometers.

3.2.2 Environmental Noise In addition to these noise sources, the LIGO detectors are sensitive to myriad environmental noise sources from their local surroundings. This environmental noise of known or unknown origin is frequently difficult to model and contributes to the disparity between the sum of noise from known noise sources and the actual sensitivity of the detectors in O3 and O4. The inadequacy of known noise sources to fully explain each LIGO detector's sensitivity is shown in figure 5. An additional significant contribution to the realized detector noise shown in figure 5 is controls noise: shortcomings, such as filter limits, of the control loops used to steer or fix optical components in place.

Significant design and commissioning work has been devoted to ensuring that at all frequencies, the limiting sources of noise are either fundamental, like quantum or thermal, or controls noise. Unfortunately, this is not always the

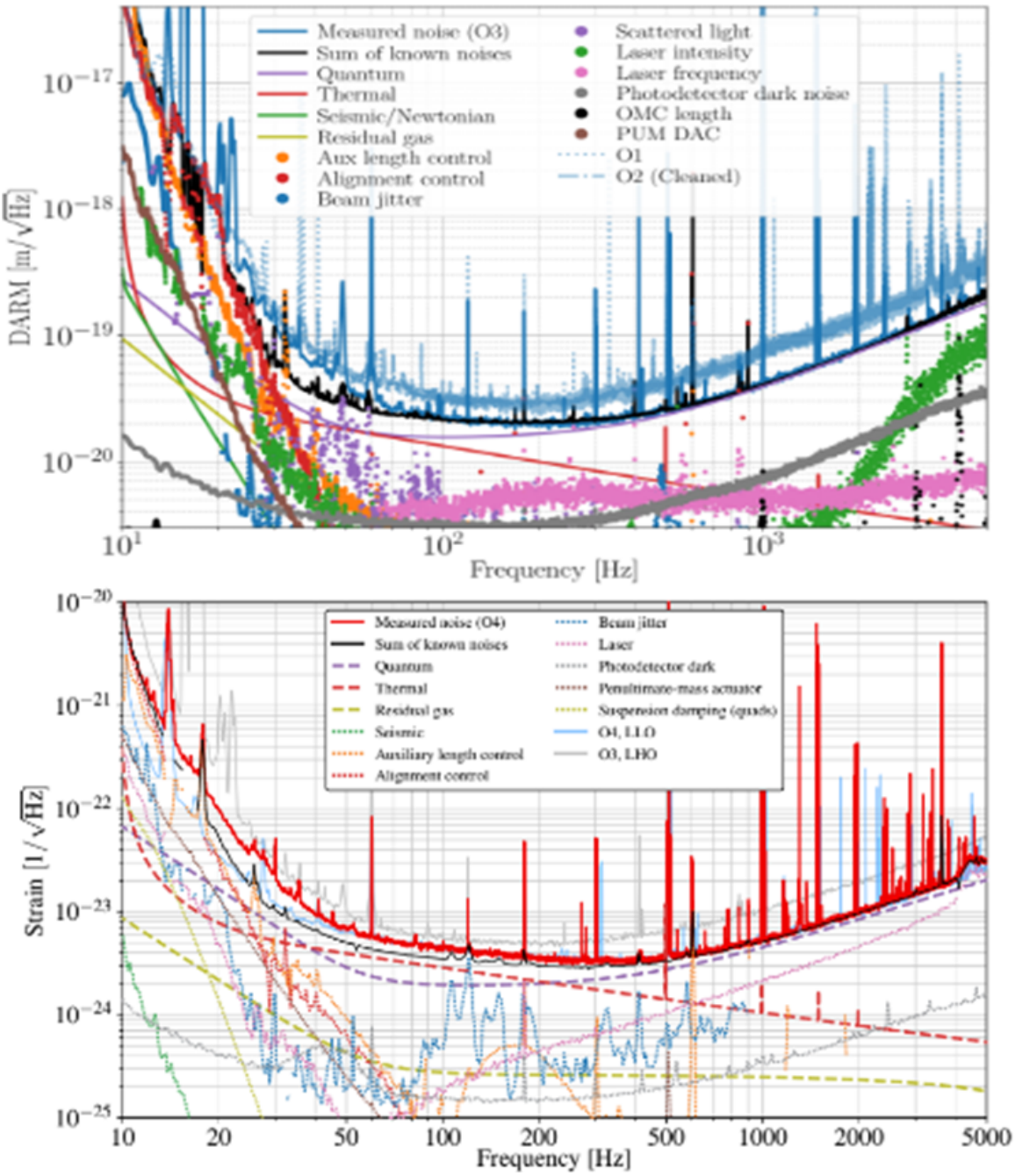


Figure 5. Noise budgets for LHO in O3 (top) and O4a (bottom) [50, 66]. The sum of known noise sources does not fully explain the shape of each detector's sensitivity curve. Note that the O3 and O4 sensitivities differ by a factor of 4,000 due to the numerical difference between DARM and strain.

case. Figure 5 illustrates that LIGO's sensitivity is is not typically limited by environmental noise, loud environmental transients can occasionally couple to the detector and degrade its sensitivity and performance.

The inability of detector noise budgets to capture the impact of environmental transients on detector sensitivity means that ambient environmental conditions must be monitored so that when environmental noise contaminates detector data, its cause can be identified. Examples of environmental noise include, but are not limited to, heightened input laser beam jitter from anthropogenic activity, interference between radio signals and the sidebands of the carrier beam, stray light beams reflecting from shaking components imparting scattered light noise, wind-induced tilts affecting the control loops used to align and maintain the arm cavity mirrors.

Transient environmental noise degrades the astrophysical sensitivity of the detectors and could bias parameter estimation should a noise transient coincide with a GW detection [118]. As the LIGO detectors become more sensitive and the rate of GW candidates increase, accurate and rapid identification and quantification of environmental effects on the GW data have become increasingly necessary.

3.2.3 Monitoring The influence of environmental noise in the detectors is monitored via several methods. Codebases have been developed which permit rapid production of summary plots to compare data from auxiliary sensors at each detector against noise in the GW strain data [119, 120]. Statistical correlations between auxiliary sensor data and transient noise in the GW channel or variations in detector BNS range are also employed to monitor and identify environmental effects [38, 121, 122].

The primary concern of this section is the use of the network of physical and environmental monitoring (PEM) sensors at each LIGO site to evaluate sources of environmental noise. This sensor network consists of over 100 sensors of various types distributed around each detector including accelerometers, microphones, magnetometers, weather stations and seismometers [111, 112, 123].

Prior to each observing run, a campaign of injections is conducted to understand the vibrational and magnetic coupling of each detector. The goal of each injection is to create environmental disturbances which are loud enough to substantially exceed the background noise ASD of one or more PEM sensors and DARM data in a particular frequency band. This can be accomplished by playing white noise on large speakers, shaking the detector's vacuum chamber walls with an architectural shaker or running current through a wire coil to affect the electromagnetic field near detector infrastructure. The results of this campaign serve two purposes: to aid in noise investigations and to assist with GW candidate event validation. The latter is discussed in chapter IV. The coupling is quantified through coupling functions (CFs) measured for each sensor. For frequency bins where the PEM sensor ASD is much greater than its background value and the DARM ASD is much greater than its background value, the sensor-DARM coupling is measured via

$$CF(f) = \sqrt{\frac{\mathrm{DARM_{inj}}(f)^2 - \mathrm{DARM_{bkgd}}(f)^2}{\mathrm{PEM_{inj}}(f)^2 - \mathrm{PEM_{bkgd}}(f)^2}}. \tag{3.2}$$

Typical choices for the injection/background ratio used for measured points in the CF are ≥ 5 for PEM accelerometers and ≥ 2 for DARM during acoustic and vibrational injections or ≥ 10 for PEM magnetometers and ≥ 1.3 for DARM during magnetic injections. In frequency bins where the injection exceeds the threshold in PEM sensors but does not excite DARM sufficiently above its ambient value, an

upper limit on the sensor-DARM coupling can be set by calculating

$$U(f) = \frac{\mathrm{DARM_{bkgd}}(f)}{\sqrt{\mathrm{PEM_{inj}}(f)^2 - \mathrm{PEM_{bkgd}}(f)^2}}. \tag{3.3}$$

Where neither condition is true, the coupling is assumed to vanish. Figures 6 and 7 show the coupling between H1:PEM-EX_ACC_BSC9_ETMX_Y, an accelerometer mounted on the side of the vacuum chamber which houses the X-arm end test mass, found by playing band-limited white noise in the 60-100 Hz band from a speaker placed near the door used to access the X-arm endstation vacuum enclosure area prior to the start of O4. Results from multiple noise injections across multiple frequency bands are combined to produce composite CFs for each PEM sensor which may span from 5-4,096 Hz.

3.3 Noise Investigations

When noise simultaneously appears in PEM sensors and in DARM, and the noise in DARM is well-predicted by the sensor's coupling function, this indicates that some environmental effect witnessed by the sensor is contaminating the GW data. Sensor data can be used to localize and characterize the behavior to study and potentially mitigate these sources of environmental noise. Conversely, non-observation of environmental noise effects in DARM that are seen by PEM sensors indicate locations which are well-isolated from the local vibrational or magnetic environment. However, the upper limit estimate on noise coupling in these cases can be used to see whether actions must be taken in the future should detector design changes improve sensitivity in the frequency region of interest. The following sections describe noise hunting and noise assessment tasks carried out in O3 and O4. Some noteworthy examples of detector noise hunting from O3 and previous observing runs are summarized in [124, 125].

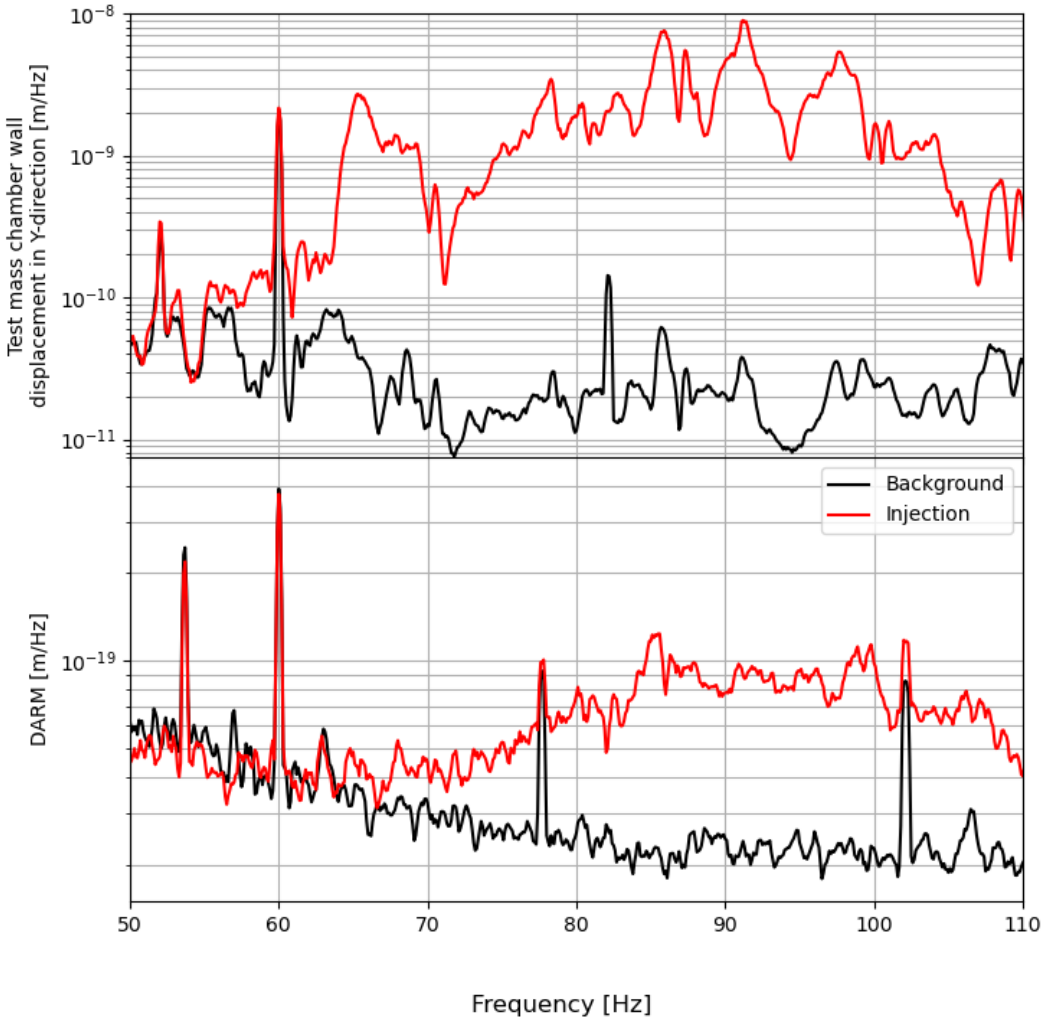


Figure 6. Response of the endstation accelerometer and DARM to an acoustic injection from 60-100 Hz. Accelerometer measurements were converted to sensor displacement by dividing the sensor ASD by $4\pi^2 f^2$.

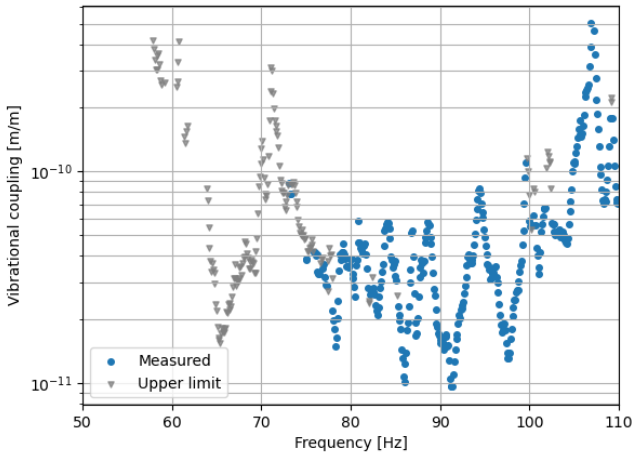


Figure 7. CF for the endstation accelerometer computed from the injection shown in figure 6.

3.3.1 48 Hz Noise Prior to the start of O3a, a transient feature in DARM was identified at $\tilde{4}8$ Hz [126–128] in LHO data. It's origin was unknown, but noise contamination in the GW data at 48 Hz was coincident with increased motion at 48 Hz witnessed by numerous corner station accelerometers. One example of temporal correlation between GW data and H1:PEM-CS_ACC_HAM6_OMC_Z, an accelerometer measuring vertical motion of the vacuum chamber which houses the output mode cleaner as well as the photodiodes which record the interference pattern used to compute DARM, is shown in figure 8. A variable-speed air handling unit (AHU) motor in one of the AHUs which cool the LHO corner station electronics bay was identified as one source of the noise at 48 Hz. This identification was made by placing a temporary accelerometer near potential noise sources, such as AHUs and water chillers. ASDs of temporary accelerometer data were produced to determine if the individual pieces of site infrastructure which the temporary accelerometer was mounted to even produced noise at 48 Hz. The AHU was eventually found to be a cause of the noise because:

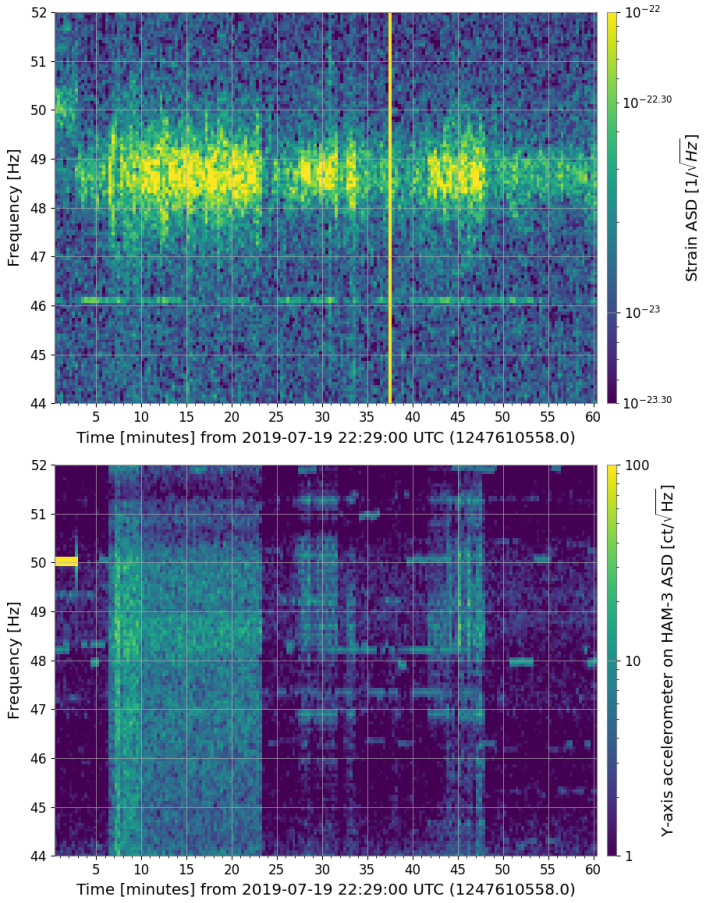


Figure 8. Spectrograms showing time and frequency correlation between 48 Hz noise in GW strain data from LHO (top) and an accelerometer placed on the vacuum chamber near the noise source (bottom). Increased broadband vibrational noise added additional noise to the GW strain data, most acutely near 48 Hz.

it was near enough to the interferometer that it was identified as a potential noise source, its motors sometimes operated at 48 Hz when studied using the accelerometer, and the appearance of heightened 48 Hz noise in GW data was contemporaneous with heightened motion at 48 Hz in the temporary accelerometer.

Because this AHU was critical for producing scientific data, it could not be turned off to remove this source of 48 Hz noise. A campaign was therefore started to identify the coupling site between the AHU noise. Impulse injections - where vacuum chamber walls are struck - were performed to search for the coupling

site by comparing the arrival times, amplitudes, and frequency content of the induced vibrations in accelerometers near the injection site with the appearance of noise in DARM [111]. Laser vibrometry was employed to rule out supports for the thermal compensation system as the coupling site [129]. However, these noise hunting techniques indicated that the coupling site was near the beamsplitter area. A new "beating-shaker" technique was used to localize the coupling site to the vacuum enclosure on LHO's input arm next to the enclosure which contains the beamsplitter. The beating-shaker injection used two shakers, one operating at 48 Hz and one operating at 48.01 Hz, to create a beat with a period of 100 s. The phase of this beat in corner station accelerometers was compared to the phase of the noise in DARM data, localizing the coupling site. The results of one of these injections are shown in figure 9.

The coupling mechanism was identified as scattered light from the scraper baffle reflecting off the interior side of an illuminator mounted on HAM3—a vacuum enclosure which contains components of the power recycling cavity. When the AHU compressor would operate at 48 Hz, the baffle would vibrate, imparting amplitude and phase noise on stray light scattering from the baffle [130, 131]. This scattered light reflected off the illuminator and was thus able to interfere with the main beam. The 48 Hz coupling was mitigated by inserting a piece of black glass between the illuminator window and the illuminator [132, 133].

To mitigate noise induced by winds driving building foundation motion and shaking optical components, wind fences were constructed at LHO's endstations between O3 and O4. To study the effect of the Y-end wind fence on the frequency content of wind gusts which pass through the fence, a trio of gustmeters were

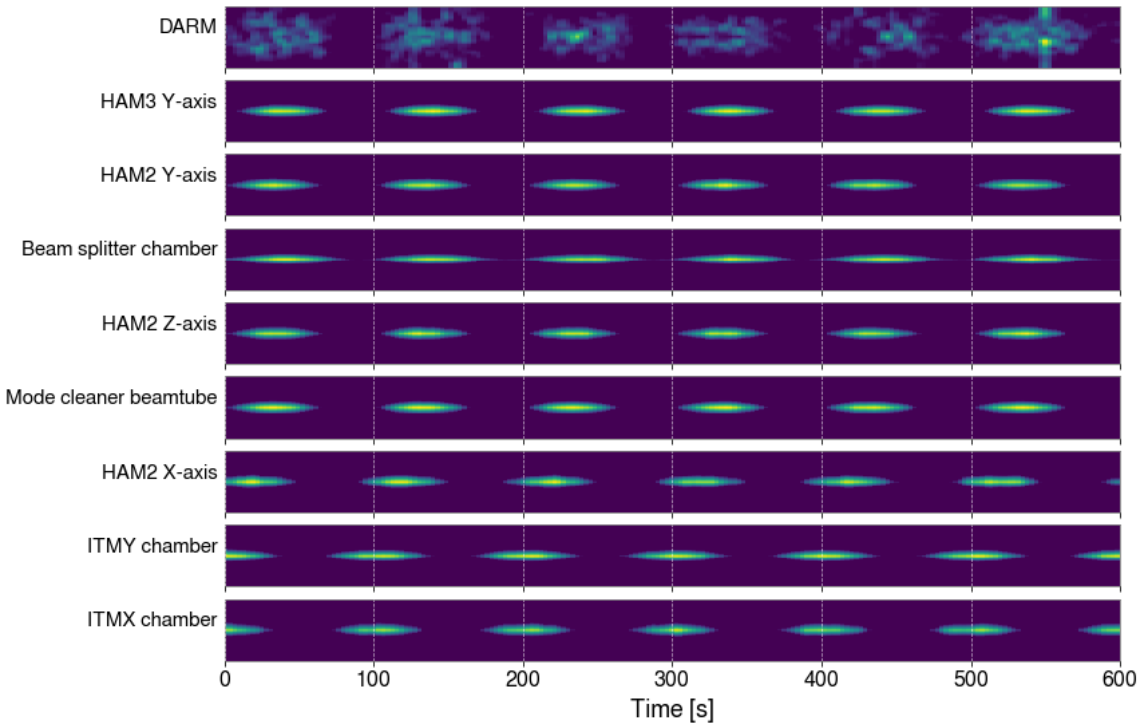


Figure 9. Comparing responses of DARM and LHO corner station accelerometers to beating-shakers injection. The poor agreement in phase between DARM and certain accelerometers, e.g. the HAM 2 X-axis accelerometer, led to potential coupling sites being ruled out [111].

calibrated and installed in temporary locations before and behind the wind fence [134].

3.3.2 Magnetic Coupling Regular measurements were taken before and during O4a to understand the potential for coupling between local magnetic fields and the interferometer [135, 136]. Local magnetic fields were generated by running a current through large coils of wire placed near electronics racks used for interferometer controls as well as in the experiment hall. The response of each interferometer to the resulting magnetic fields was quantified using the network of PEM magnetometers set up around each observatory [111, 123]. In order to vet GW candidates at kilohertz frequencies, such as transients from neutron star f-modes [137–139], more computing space was allocated prior to O4a to store accelerometer and magnetometer data up to 8192 Hz. Nearly every week of O4a, a broadband magnetic field was injected at 1000-4096 Hz at 7 locations around LHO for 36 s at each coil to quantify magnetic coupling in the newly-monitored part of the kilohertz regime. These injections provoked a response in $h(t)$ at the LIGO LHO corner station. Figure 10 shows the $h(t)$—the time-domain GW strain data measured by LHO—response to several of these weekly injections compared to a reference background time. Weekly probes of the high frequency magnetic coupling could be used to more accurately estimate the total environmental contribution to a high-frequency GW candidate [140]. Broadband magnetic injections were also made over 10-100 Hz and 100-1000 Hz from these 7 coils as part of the weekly injection campaign.

During the course of O4a, the magnetic coupling of the detector at kilohertz frequencies fluctuated from week to week. At the beginning of O4a, the LHO detector was somewhat sensitive to large external magnetic fields applied at the

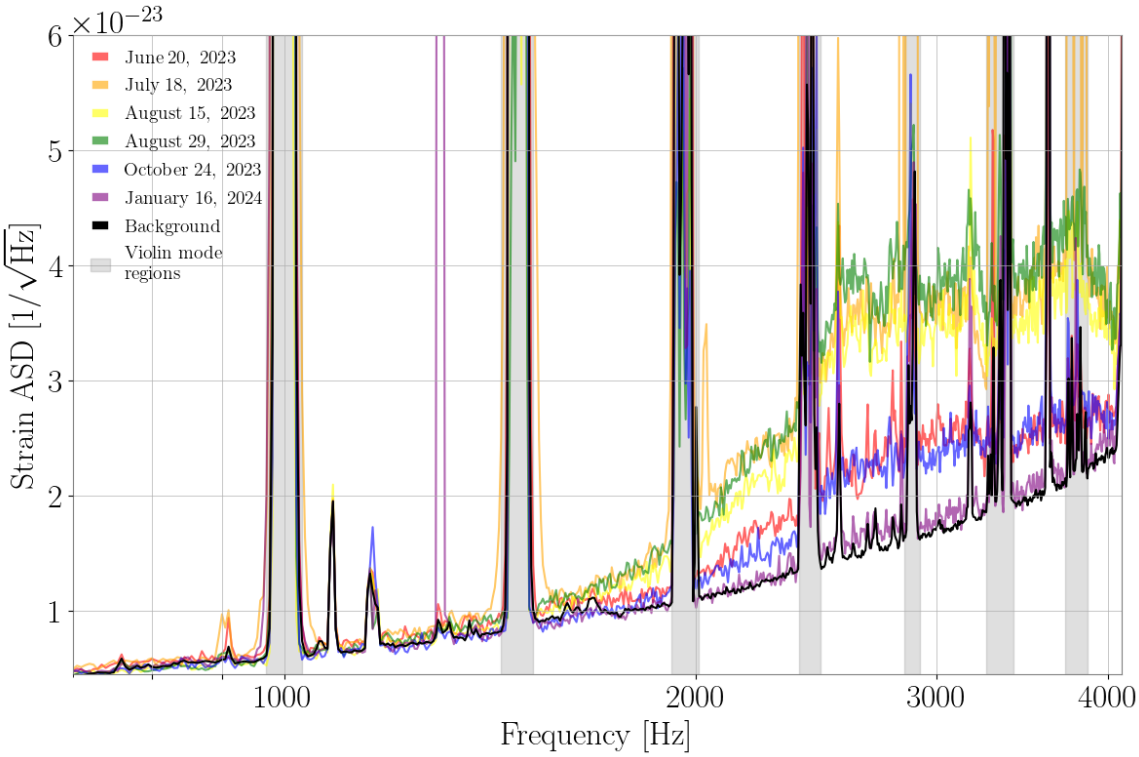


Figure 10. $h(t)$ data from 6 of the 22 weekly high-frequency magnetic injections performed at the LHO corner station. Above ∼2000 Hz, there was a significant response in $h(t)$ when a large external magnetic field was applied near the beamsplitter area during the middle portion of O4a. The reference background time was taken on June 20, 2023. Sensor background for each injection are shown in figure 11. The strain ASD also varied from week to week in certain frequency bands due to the relative absence or presence of excited thermal (violin) modes in the data. The violin mode frequency bands are denoted by the grey regions in the figure.

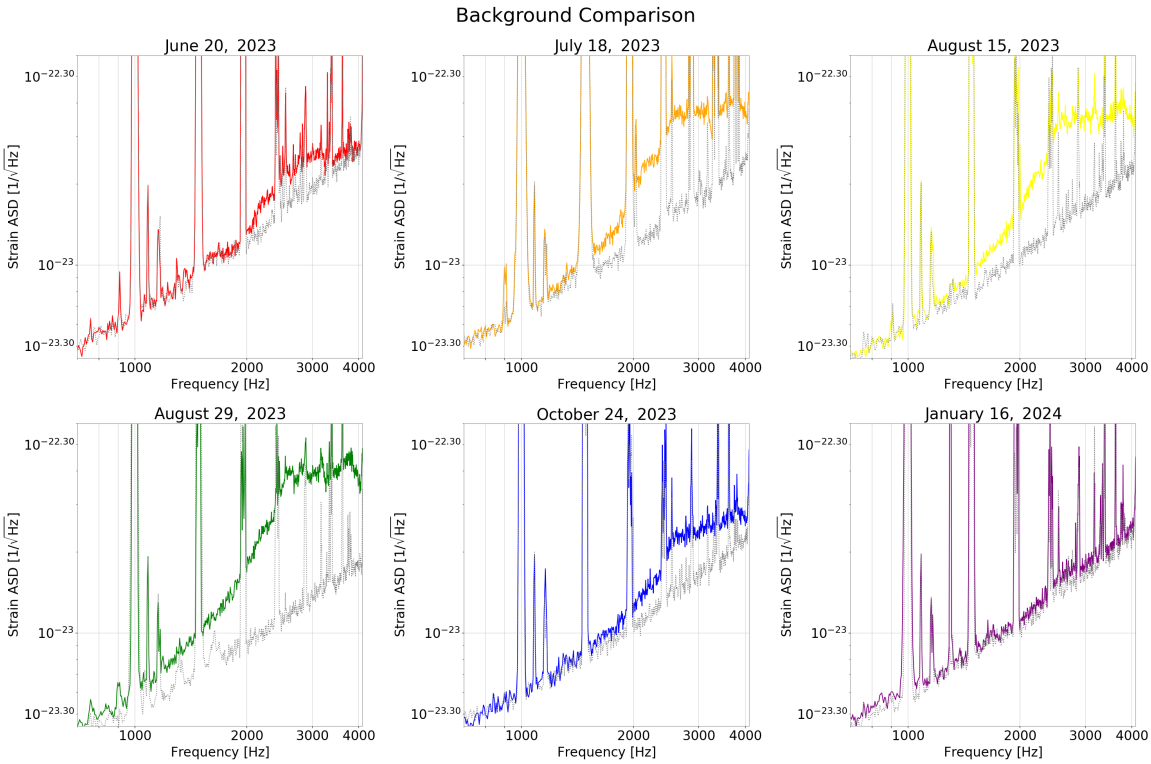


Figure 11. Comparison of detector strain data during high-frequency magnetic injection times for each injection (colored traces) shown in figure 10 and reference background times (grey traces) taken a few minutes prior to each injection. The variation of LIGO Hanford's response to the weekly magnetic injections is not due to fluctuations in the ambient value of strain at high frequencies.

corner station. Towards the middle of O4a, the detector's response to these applied magnetic fields increased, before dropping to being only weakly coupled towards the end of O4a. The most likely mechanism for the observed magnetic coupling in the kilohertz regime is magnetic interference with cables that control the LIGO suspensions and optics. Specific mid-run electronics configuration changes which affected the degree of magnetic coupling, such as new cables being connected to chassis, have not yet been identified.

3.3.3 Input Power Settings and Vibrational Coupling The amount of laser power input into the LIGO interferometers has increased in each Observing run. Increased power circulating in the arms improves the high-frequency sensitivity of the LIGO detectors by reducing the effect of quantum shot noise. In O4a, both LIGO detectors were slated to operate with 75 W of laser power sent into the input mode cleaner (IMC).

As input laser power was increased at both detectors prior to the fourth Observing run, vibration coupling also increased. This includes vibration coupling through both scattered light noise and input beam jitter noise. The dramatic increases in coupling have prompted a warning that vibration coupling may become increasingly problematic as power increases [141]. A possible explanation is that increased thermal distortion of the test mass surfaces around coating defects may increase scattered light and also reduces the symmetry of the arms, decreasing common mode rejection of input noise.

Due to duty cycle and control scheme concerns associated with high-power operation the laser power sent to the IMC was reduced from 75 W to 60 W at LHO during O4a [142]. Figure 12 shows the reduction in vibrational coupling between

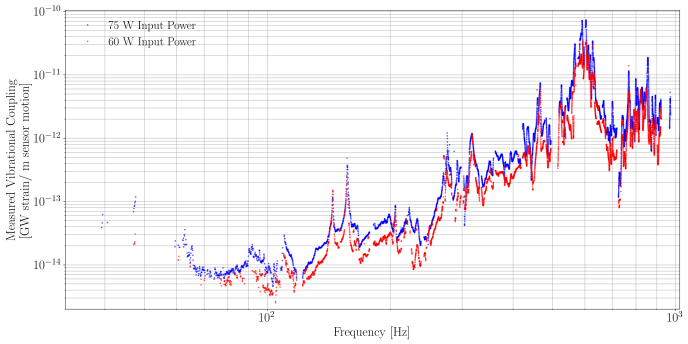


Figure 12. Comparison of the composite vibrational CF between PEM sensors placed around the PSL optics table measured during 75 W (blue) and 60 W (red) operation. The measured vibrational coupling at the input laser, observed where both the GW data channel and PEM channels witness a PEM injection [111], is worse at nearly all frequencies when operating at 75 W of input laser power.

PEM sensors placed around the in-air optics table where the input laser light is produced and the apparent differential arm length.

3.4 Glitches

Glitches are noise transients in the GW data which are not of astrophysical origin. Their time-frequency behavior is often regular enough that many can be classified by their appearance in spectrograms. Their origin can be known or unknown. *Whistle glitches*, for example arise from beat notes from voltage controlled oscillators [143], while the occurrence of *extremely loud glitches* cannot reliably be correlated with features or trends in auxiliary channel data. Examples of these glitches are shown in figure 13. Glitches whose appearance can be predicted by auxiliary channel data can be removed from interferometer data used for searches via data quality vetoes [65, 124].

3.4.1 Blip Glitches

Blip glitches are a class of glitches which are short ($\mathcal{O}$(0.1 s)) duration, large bandwidth ($\mathcal{O}$(1 kHz)) glitches seen in LIGO data since Initial LIGO, the experiment configuration prior to O1 [145]. Their incidence varies from observing run to observing run, as shown in figure 14, but

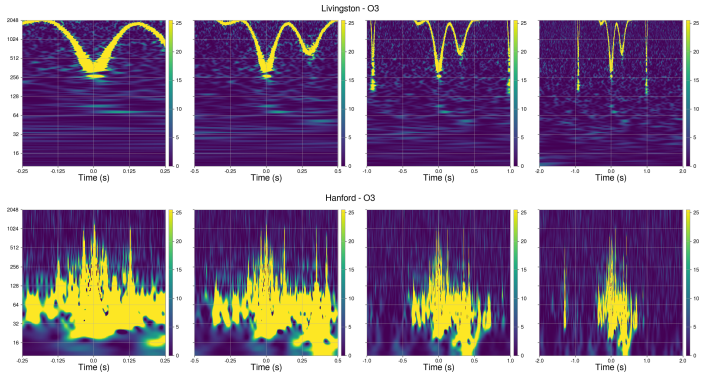


Figure 13. Q-transform of a whistle glitch (top) and an extremely loud glitch (bottom) in GW strain data. These glitches occurred on February 4, 2020. The whistle glitch pictured here occurred at LLO while the extremely loud glitch occurred at LHO. These glitches were identified by the citizen-science-aided machine learning algorithm GravitySpy [144] and LDVWeb [119] was used to access the LIGO glitch database.

it is $\mathcal{O}(1/\text{hour})$ at each observatory for each observing campaign. Figure 15 shows the duration of blip glitches in different epochs and observatories and figure 16 shows their bandwidth. While modeled searches for GWs from CBCs have become more effective at subtracting glitches from the data stream [146–150], they still present a significant challenge to unmodeled searches as well as the template-based CS search pipeline [68, 76, 81, 106]. Their time-domain behavior resembles astrophysical sources and they persist for only a few cycles in the detector, limiting the effectiveness of excess-power or template-based techniques—which suffer from sparseness in the case of intermediate-mass and eccentric BBH mergers—at distinguishing glitches from real GWs signals. If auxiliary channels were identified which could be correlated with instances of blip glitching in the GW data, this would improve the sensitivity of these searches.

3.4.1.1 Searches for Origin In O1 & O2, it was found that fewer than 8% of blip glitches at LHO and 2% of blip glitches at LLO were correlated with site humidity, anomalous signals in a PSL intensity stabilization servo

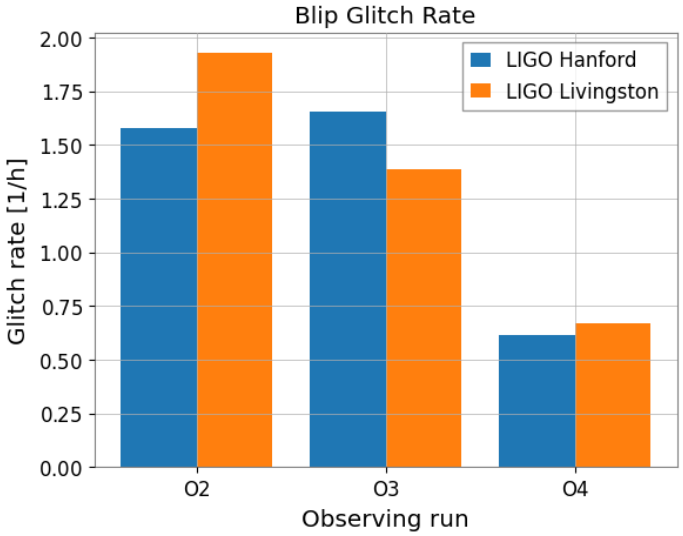


Figure 14. Rate of blip glitches in the LIGO detectors from O2 to April 1, 2025. Rates were calculated from the number of glitches identified by GravitySpy as being blips with a confidence of 0.95 or greater.

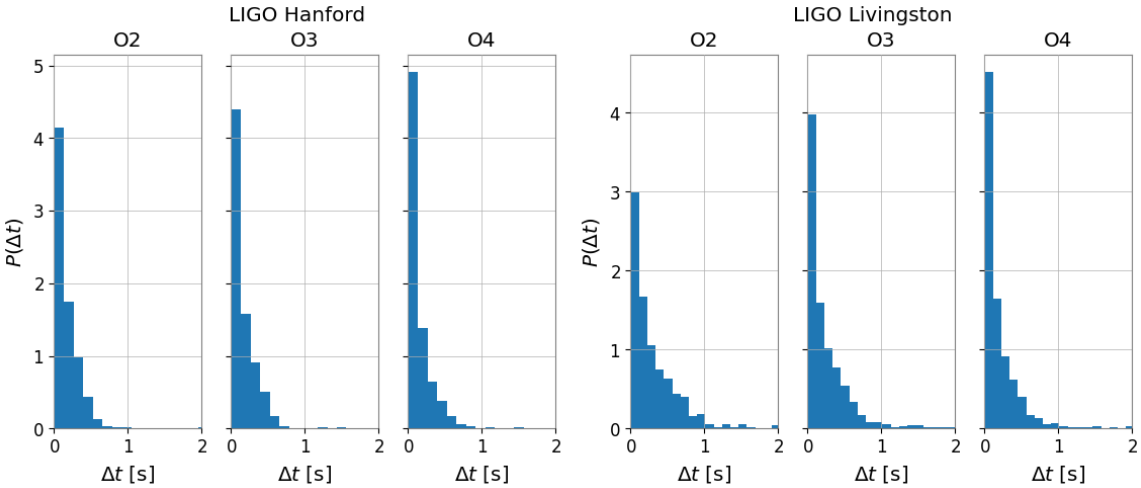


Figure 15. Distribution of blip glitch durations in LHO and LLO in O2-O4 through April 1, 2025.

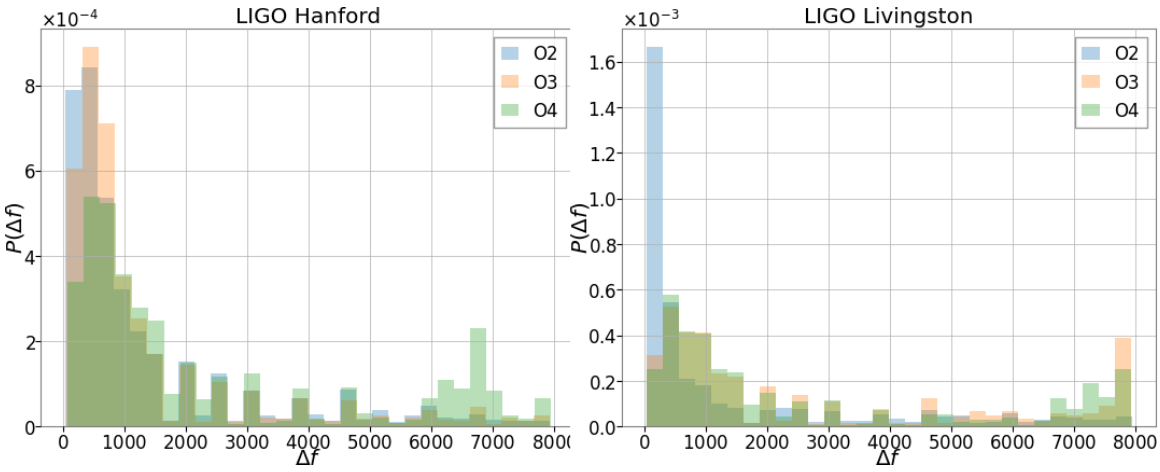


Figure 16. Distribution of blip glitch bandwidths in LHO and LLO in O2-O4 through April 1, 2025.

photodiode, computer timing errors in suspension, controls and arm length stabilization channels, and transients in the power recycling cavity pick-off port photodiode [145]. However, the cause of most blip glitches are unknown. The correlations described above account for only a small fraction of the population of blip glitches seen in the LIGO detectors.

The humidity correlation was reexamined in O3. A possible coupling mechanism for blips could involve increased buildup of static electricity on electronics cooling fans during periods of low relative humidity [145]. Electrical discharges from these fans may affect the electronics that they cool. Periods of low relative humidity in this area could arise from normal weather conditions at LHO or the use of heaters during cold winter months to warm up observatory facilities. Figure 17 shows the hourly blip glitch rate at LHO compared to the humidity of the mass storage room at the observatory—the location where information from LHO's thousands of channels is written to memory. The humidity and blip glitch data exhibit a Spearman correlation of -0.07, indicating that, overall, humidity and blip glitch rate are not strongly statistically anti-correlated. Closer study of the

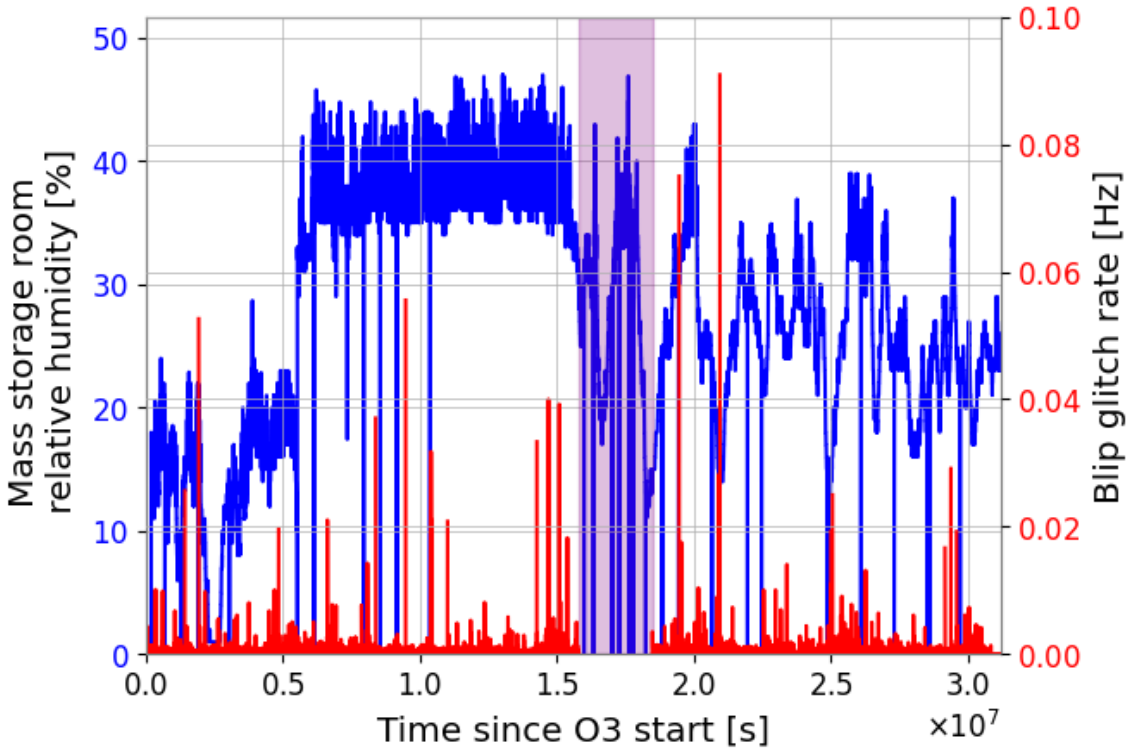


Figure 17. Timeseries of the mass storage room humidity (blue) and the blip glitch rate (red) at LHO in O3. The lavender area represents the O3a-O3b break. The glitch rate calculation was realized by collecting all O3 glitches which were classified as blips by GravitySpy with a confidence of 95% or greater in O3.

blip glitch rate during the lowest-temperature periods of O3 may provide a better test of the static electricity hypothesis.

Cosmic rays could cause blip glitches by imparting momentum to the test masses or changing the charge configuration on the exterior of the vacuum enclosure, affecting the strength of the Coulomb force applied to control the motion of the final stage of the test mass. Four photomultiplier tubes were installed at LHO prior to O1 as a cosmic ray detector which could be used in the GW candidate event validation process. They are located beneath the vacuum chamber which houses the Y-arm input test mass. O2 & O3 data photomultiplier tube data was studied to identify times of high-energy cosmic ray showers at LHO. Figure 18

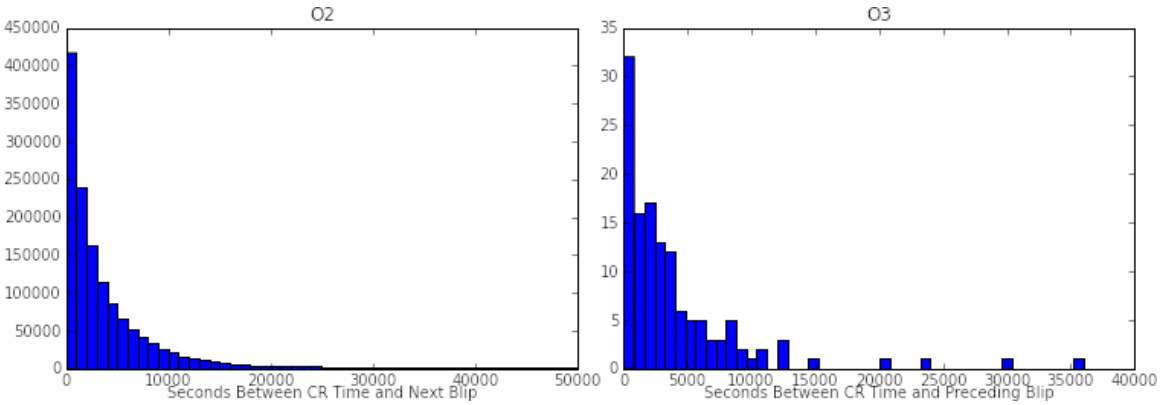


Figure 18. Histograms of time delay between cosmic ray detections in LHO and blip glitches in O2 (left) and O3 (right).

shows the time between cosmic ray showers and blip glitches at LHO. The time distribution is consistent with two uncorrelated Poisson processes, indicating that cosmic rays do not cause blip glitches.

Following the conclusion of O3, LHO operated with its IMC shut down so that no light fell on the photodiodes in the output mode cleaner (OMC) whose output are used to compute the GW strain. Blip glitches could be caused by data corruption or computing problems in the data acquisition systems which would still be present in the no-light data. 85 hours of output photodiode data was examined with the Omicron algorithm [151] using a set of search parameters based on O3 blip glitch properties. None of the Omicron triggers in the no-light data were visually consistent with blip glitches upon manual inspection [152]. Figure 19 shows the behavior of these photodiodes during O3 blip glitches compared to photodiode performance around times identified by the Omicron search in the no-light period.

3.4.1.2 Pre-O4 OMC Characterization Prior to O4, a mock-up of the planned OMC data acquisition system was built at LHO to test its performance [153]. Noise resembling the typical spectra of the OMC photodiodes was injected into this mock-up. The data output by the test stand was analyzed

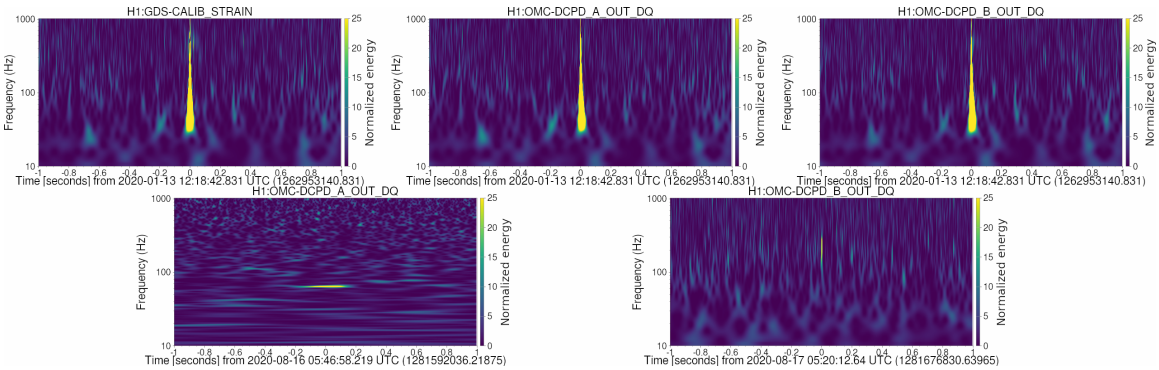


Figure 19. Calibrated strain (top left) and OMC photodiode (top center, top right) data from LHO during an O3 blip glitch and OMC photodiode (bottom) data from the no-light test. Data from the two photodiode channels are combined to produce the observatory's strain measurement. The two Q-transforms in the bottom row were among the highest SNR glitches found by the Omicron algorithm set to find excess non-Gaussian noise which resembled blip glitches.

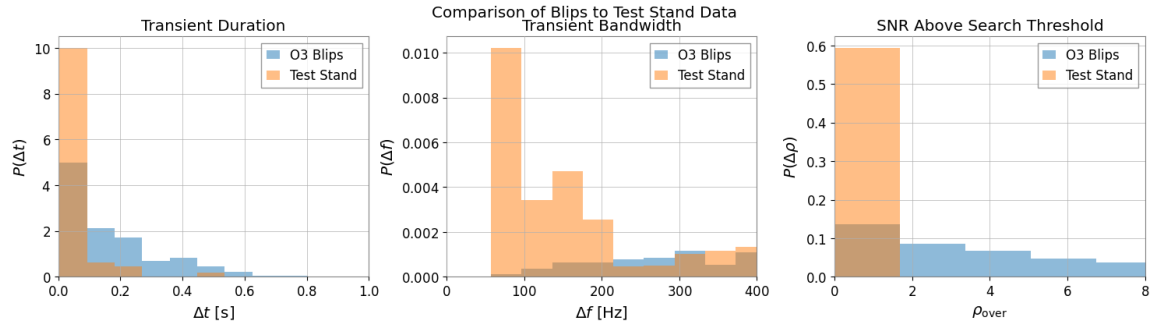


Figure 20. Comparison between blip glitch and Omicron trigger properties for data from the OMC mock-up.

with the same Omicron search settings described in section 3.4.1.1. No blip glitches were found in the mock photodiode data and the duration and SNR distributions of Omicron triggers were substantially different from data surrounding O3 blip glitches, as shown in figure 20. The OMC data acquisition system was not identified as the source of blip glitches [154].

CHAPTER IV

ALGORITHMIC EVALUATION OF ENVIRONMENTAL NOISE IN LIGO

The senses are particularly deceived with regard to the smallest differences of ordinary things and usual objects.

—Vincenzo Galilei, *Dialogue Concerning Ancient and Modern Music* [155]

Sections 4.1.1-4.1.5 of this chapter were published in volume 41 of Classical and Quantum Gravity in July, 2024 [140]. Philippe Nguyen designed an early version of the PEMcheck algorithm described herein based on the hand-vetting work developed by Robert Schofield. Robert Schofield and Raymond Frey suggested methodological improvements to the algorithm while in development and testing. Raymond Frey was the principal investigator for this work.

4.1 Automated Evaluation of Environmental Coupling for Advanced LIGO Gravitational Wave Detections

4.1.1 Introduction The era of GW astronomy began in 2015, when the LIGO detectors directly observed the GWs from a BBH merger [28]. In 2017, the first GWs from a BNS merger were observed by the LIGO detectors [43]. Subsequent sky localization of GW170817's host galaxy was aided by the GW observatory Advanced Virgo, which did not observe GWs from the merger due to the orientation of the detector relative to the source [25, 43, 45]. In total the LIGO detectors, along with Advanced Virgo and KAGRA, have observed 90 GWs from CBCs in the course of the first three observing runs [26, 37, 53, 54, 156].

The LIGO detectors are a pair of nearly-identical observatories. LHO is located near Hanford, Washington, United States and LLO is located near Livingston, Louisiana, United States. Each detector is a kilometer-scale dual-

recycled Fabry-Pérot Michelson interferometer [24, 50]. A GW incident on one of the LIGO detectors produces an optical path length difference between light circulating in the two arm cavities of the interferometer. This varying difference in optical path length creates a time-dependent interference pattern when the light from the interferometer arms are recombined.

The amplitude of GWs is expressed as the GW strain h, where

$$h = \Delta L / L \tag{4.1}$$

with ΔL the DARM between the two interferometer arms and L the unperturbed arm length, i.e. 4 km. Typical GWs observed by the LIGO detectors have strain amplitudes $\mathcal{O}(10^{-21})$. This extreme sensitivity results in local environmental noise easily coupling to the detector output. Examples of environmental noise seen in the O3—which lasted from April 1, 2019 to March 27, 2020 with a commissioning break during the month of October 2019—include ground motion induced by air handling motors at LHO, ground motion from trains traveling near LLO and heightened anthropogenic activity at both sites during the normal workday increasing each detector's local ground motion [53, 54, 111, 157, 158]. Correlated noise between the two LIGO detectors originating, for example, from lightning strokes, could potentially mimic or contaminate a GW signal [159, 160]. Given the precision needed to measure GWs and the diversity of potential environmental noise sources, it is crucial to identify times where the GW data may be contaminated by environmental effects.

When a GW is observed by one or more of the LIGO detectors, detector characterization specialists must examine both the DARM data as well as data from a network of environmental sensors at each of the LIGO sites and rapidly determine: (i) whether the GW candidate was a result of environmental effects in

the DARM data, or (ii) whether there is environmental noise that is contaminating the signal, and if so, at what times and frequencies the noise occurs [111, 124]. While there is no evidence so far that environmental noise has measurably affected a GW detection, the margin for safety grow smaller as the sensitivities of the LIGO detectors improve.

In this chapter, we report on a tool, PEMcheck, developed to rapidly identify times and frequencies where environmental signals may couple to the DARM measurement made by the LIGO detectors. The tool estimates the degree of environmental coupling and produces a recommendation for detector characterization experts to accept or reject a GW candidate event due to the absence or presence of environmental noise contamination in the GW data. This determination is typically completed in under 10 minutes.

This work represents a step forward in automated GW event validation. Prior to O3, any assessment of environmental contamination in a GW candidate was carried out entirely by hand [28, 161, 162]. During O3, a first attempt at automatically highlighting potential environmental contributions to GW signals was added as part of the data quality report (DQR) which was generated for each potential GW candidate [111, 112, 124, 163]. Its implementation led to a number of false positives where potential environmental coupling was identified by human event validators but was subsequently ruled out after PEM experts reviewed PEM sensor data and found the previous version had often been overestimating the degree of environmental coupling. Transients in PEM channels near the GW candidates often showed that the claimed PEM couplings were inconsistent with the actual level of coupling during the event, usually at a frequency where only an upper limit estimate of the coupling was found (see section 4.1.2.2). In

this work, we have improved upon this initial design in several ways. We have designed a metric, the contamination statistic, which LIGO event validators can use to quickly establish whether there is substantial environmental noise in a GW candidate signal. We have also restricted automated coupling estimates to times and frequencies near GW candidates; previously the analysis was restricted only in time. In addition, we have implemented a sanity check for coupling estimates through a tuning procedure where we identify and reduce coupling factors which overestimate coupling to the GW channel. The inclusion of PEMcheck in the O4 DQR means that the environmental coupling assessment is available within minutes of a candidate event for the hundreds of candidate events expected to be observed in O4 [27, 62, 164].

4.1.2 LIGO Environmental Monitoring

4.1.2.1 PEM System Description There are around 100 instruments at each LIGO detector which monitor the detector's local environment. This PEM system is composed of accelerometers, microphones, magnetometers, voltage monitors, weather stations and other sensors. A map of all PEM sensors at each LIGO detector is available at the LIGO PEM group webpage [165]. A thorough description of the PEM sensor network in its O3 configuration is found in [111]. Most PEM sensor data used for this work is sampled at 4096 Hz, although there are a few accelerometers and magnetometers which are sampled at 8192 Hz and 16384 Hz. Detailed information on specific sensors and their configuration may be found in [111].

The LIGO detectors have been modified in advance of the O4 to accommodate frequency-dependent quantum squeezing to improve the sensitivity of the observatories [67]. In addition, test masses at each detector were replaced

due to defects in their mirror coatings [64]. The input laser power was increased. Several baffles were added to reduce scattered light noise and some existing baffles were damped to further reduce scattered light noise [158]. The septum window separating the OMC from the rest of the interferometer was removed due to scattered light concerns as well. Prior to the start of O4, changes were also made to the PEM system. To reduce low-frequency quantum radiation pressure noise introduced by the addition of frequency-independent quantum squeezing in O3 [50], a ∼300 m long filter cavity (FC) was constructed at each LIGO detector prior to O4 in order to realize frequency-dependent squeezing [67]. Accelerometers and magnetometers were added to the newly-constructed FC endstation to monitor new potential noise coupling sites. A magnetometer monitoring the magnetic field near the LLO end-Y station (EY) seismic isolation controllers was added [166]. Large wire coils were installed to generate magnetic fields around the detectors to study the degree of magnetic coupling. The suite of microphones at LHO was replaced with upgraded hardware [167]. At both detectors, more computing space was allocated for PEM data storage so that GW signals up to 4 kHz could be vetted by PEM accelerometers, magnetometers and voltage monitors.

4.1.2.2 Studying Environmental Coupling

PEM sensor data can be used to determine CFs that quantify the degree to which environmental effects contribute to DARM. CFs are determined by an extensive injection campaign prior to, after, and in the case of magnetometers, during each observing run. Detailed descriptions of injection procedures are found in [111, 123]. Here we summarize the process for determining the CF for a PEM sensor. A more thorough discussion is found in [111]. As an example, we will consider L1:PEM-CS_ACC_HAM6_OMC_Z_DQ, a channel associated with an accelerometer at LLO

which records vacuum chamber motion in the vertical direction. This particular sensor is mounted atop horizontal access module (HAM) 6, the vacuum enclosure which contains the OMC—the meter-scale optical cavity which rejects unwanted light from the recombined signal from the interferometer arms, like modulation sidebands and higher order transverse modes [168]. The photodiodes used to measure DARM are also situated in HAM 6 where they witness the transmitted laser light leaving the OMC. Ground motion couples to DARM measurements by shaking the vacuum chamber walls or components on the optics table within this vacuum chamber, causing noise when light scattered from these shaking objects recombines with the main beam [158].

To quantify the response of the LIGO detectors to environmental perturbations, CFs between individual PEM sensors and the DARM data are produced. To measure a CF for a particular sensor, we perform many environmental noise injections across different frequency regimes and compare the response of the PEM sensor to the response in DARM. In the case of the OMC accelerometer, these include playing tones on a nearby speaker and mechanically shaking the nearby vacuum enclosure. To compute the CF for this OMC accelerometer, we compare the frequency-domain response of the PEM sensor and DARM during the injection. Specifically, we compute the ASDs of the accelerometer and DARM, denoted by $X_{\mathrm{inj}}(f)$ and $Y_{\mathrm{inj}}(f)$, respectively. These are compared to ASDs of sensor and DARM data from a quiet reference time where no environmental noise injection is occurring (denoted $X_{\mathrm{bkgd}}(f)$ and $Y_{\mathrm{bkgd}}(f)$, respectively).

At some frequencies, the detector couples strongly to the environment and the injected time DARM ASD clearly differs from the reference time ASD.

For frequencies where this is the case, we compute the CF by equation 3.2 [111]. Here we adopt the notation $M(f)$ indicates that these are "measured" points in the CFsince the detector response to an injection can be directly quantified by comparing the change in DARM and sensor ASDs.

At frequencies where the interferometers are well-isolated from environmental noise sources, a CF cannot be measured since the DARM ASD is unperturbed by the injection. In this case, we may only set an upper limit on the coupling between the PEM sensor and DARM. An upper limit estimate, $U(f)$, of the coupling may be set via equation 3.3 by assuming that at these frequencies, any noise in the DARM ASD is due to noise witnessed by the PEM sensor [111].

The measured points and upper limit estimates on the coupling calculated via equations 3.2 and 3.3 are combined across several injections in different frequency bands to form a CF for each PEM sensor that runs from a few Hz to a few kHz. Each sensor's CF is a mix of measured points and upper limit coupling estimates. The value of the CF at a given frequency is chosen by identifying the highest-amplitude injection in the PEM sensor at that frequency (i.e. the injection with the largest value for $X_{\mathrm{inj}}(f)$ that frequency). the CF at the particular frequency takes the value of the measured or upper limit estimate of the coupling computed by equation 3.2 or 3.3 for this highest-amplitude injection. Figure 21 shows the CF computed for L1:PEM-CS_ACC_HAM6_OMC_Z_DQ by combining several PEM injections which was used during O3.

Potential sources of uncertainty for measured points in the CF arise from, for example, the finite spacing of PEM sensors. An environmental signal may be louder at an unmonitored coupling site than at the nearest sensor, resulting in an underestimation of the signal's effect on the GW data. Occasional

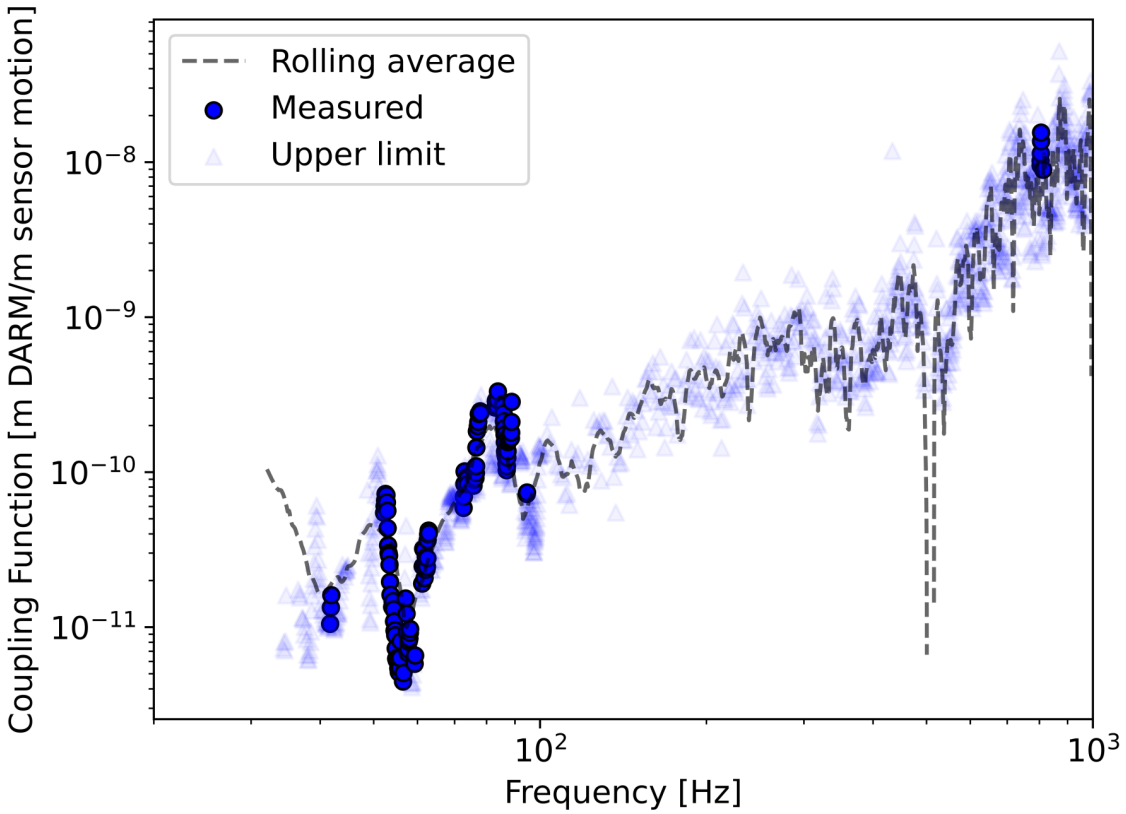


Figure 21. Vibrational coupling between LLO's HAM 6 vacuum chamber Z-axis accelerometer and DARM as measured prior to O3. The vibrational coupling here is likely driven by stray light scattering off of the septum window dividing this vacuum chamber and the adjoining HAM 5 chamber and then recombining with the main beam [169]. The large fraction of upper limit estimates, rather than measured values, for the vibrational coupling is because PEM injections could not be increased to an amplitude such that the injection was visible in the DARM data without saturating the accelerometer signal. We directly convert the acceleration measured by the accelerometer into displacement of the vacuum chamber wall. The resonance near 100 Hz could be a resonance of the vacuum chamber wall, the table, or optics on the table. Near 500 Hz the CF is set to 0 m/m because the detector is insensitive around the frequencies of the test mass suspension resonances (violin modes) [170].

environmental disturbances, such as the thunderclap discussed in section 4.1.4.5, show that predictions for DARM made using PEM and CF data correspond to the recorded value of DARM during the environmental transient with a factor of ~ 2 uncertainty [111]. The true coupling between a PEM sensor and the DARM is given by a log-normal probability distribution since systematic uncertainties in the injection procedure prevent an entirely accurate measurement of the coupling at a given frequency [112].

We may estimate the contribution of environmental noise to the DARM measurement by projecting

$$Y_{\text{noise}}(f) = CF(f) \times X_{\text{GW}}(f) \tag{4.2}$$

where $X_{\text{GW}}(f)$ is the ASD of time series data in a given PEM sensor around the time of a GW candidate, $Y_{\text{noise}}(f)$ is the ASD of the DARM time series recorded at the GW candidate time solely due to environmental influences witnessed by the PEM sensor, and $CF(f)$ the sensor's CF.

For this work, we use CFs measured for O3 [171, 172]. Injection campaigns at both LIGO detectors have been completed to update the CFs for their use in O4 [135, 136].

4.1.3 Quantifying Environmental Coupling

4.1.3.1 Data Access The PEMcheck analysis requires basic information about the GW candidate it is studying. This information can either be input manually by the user or it can be supplied automatically in the form of a GraceDB Superevent ID [173]. If given a Superevent ID, PEMcheck identifies the preferred event if there are a collection of triggers from different search pipelines all associated with the same GW candidate. We use the GWpy software package for data access and signal processing [120].

PEMcheck is designed for data quality assessments of short-duration GW transients. While it is best-suited for studying GWs from CBCs, it can also be extended to analyze brief bursts of GWs from poorly modeled sources (e.g. cosmic strings, highly eccentric BBH mergers, etc.) [76, 106]. For events identified by the low-latency CBC search pipelines GstLAL, MBTA, PyCBC Live and SPIIR, PEMcheck requires the masses and spins of each of the compact objects in the CBC as well as the GW candidate time [174–180]. The waveform parameters can be extracted from the GW candidate's preferred event data on GraceDB. These parameters are used to approximate the time-frequency evolution of the GW signal in the LIGO detectors using a non-precessing waveform model for CBCs which incorporates terms up to order 4 in the post-Newtonian expansion of the effective-one-body gravitational potential. The particular numerical relativity (NR) approximant used by PEMcheck also employs reduced-order modelling of the potential which reduces the time needed to compute the GW waveform with a minimal effect on waveform accuracy [181]. In the case of a short, unmodeled GW transient, PEMcheck requires the time and frequency ranges at which GW strain was observed by the cWB pipeline [75, 182]. This information is also available on GraceDB if a cWB trigger is identified as the preferred event. The time and frequency information restricts the search for environmental coupling to the time and frequency ranges at which the GW candidate is witnessed by the detectors, which was not the case for the pre-O4 tool used to evaluate the presence of environmental noise in the DARM data. In addition to automatic parsing of GraceDB data, PEMcheck also accepts manual entry of waveform parameters or rectangular regions in time-frequency space where excess energy is observed in the GW data. In the case of a noteworthy GW candidate during O4, such as the

Table 1. Basic detection information and initial estimates of source frame masses and dimensionless spins for GW190707. This information is used to estimate the GW waveform shown in figure 24.

Online LIGO detectors	LHO, LLO
t_c (GPS time, s)	1246527224.18
$m_1/M_\odot$	15.51
$m_2/M_\odot$	8.62
χ_1	-0.30
χ_2	0.76

first detection of GWs from a new source type, PEM experts will still vet the data by hand.

Here we use GWTC-3 event GW190707_093326 (hereafter GW190707) as an example to describe how PEMcheck estimates the extent to which environmental noise contaminates the GW data [52, 183]. Table 1 lists the inferred merger properties used by PEMcheck for waveform approximation. We restrict the following discussion to LLO data.

Once the time and frequency ranges of the GW candidate are established, PEMcheck requests DARM and PEM sensor data from around the candidate time. The DARM data is sampled at 16384 Hz. This time series data is split into foreground and background times. For CBCs, the default definition for the foreground time is $t_{\rm fore} = [t_{20}, t_c]$, where t_{20} is the earliest time at which the GW signal is greater than or equal to 20 Hz and t_c is the merger time as specified by the GraceDB preferred event. For each candidate event, a suitable background time period is also identified. For a CBC signal, the minimum background time is $t_{\rm back} = [t_{20} - 32\ s, t_{20})$. For a burst signal, $t_{\rm fore} = [t_{\rm start}, t_{\rm end}]$ and $t_{\rm back} = [t_{\rm start} - 32\ s, t_{\rm start})$, with $t_{\rm start}$ and $t_{\rm end}$ the beginning and end of the time period identified by the burst search pipeline. The foreground time is defined to capture the behavior of the PEM sensors and the GW data during the GW candidate

itself. The background time is chosen to provide the longer-term behavior of these channels. A longer background time means that any glitches in the GW channel which occur during the background are averaged over, reducing the amount they affect this calculation. In the case of a longer-duration GW signal, the background time can extend to up to 256 s prior to t_{20} or t_{start} for a CBC or burst signal, respectively. The background duration is increased from the minimum when the duration of the foreground period is comparable to the minimum background duration of 32 s. In the case of GW190707, t_{20} =1246527219.46 s and t_c is given in table 1.

4.1.3.2 ASD Projection Using the time series data described above, we calculate the ASD of DARM and each PEM sensor data during both the foreground and background time segments. The duration, τ, of each fast Fourier transform used in the ASD calculation is given by

$$\tau = \begin{cases} 0.25\ s & \text{if } t_{\text{fore}} < 2 \text{ s} \\ t_{\text{fore}}/8 & \text{if } 2 \text{ s} \leq t_{\text{fore}} \leq 8 \text{ s} \\ 1\ s & \text{otherwise} \end{cases} \tag{4.3}$$

and the overlap fraction is $\max(1/2, 1 - t_{\text{fore}}/16\tau)$. Welch's method with median averaging and a Hann window is used to calculate the ASD for each channel [184]. Figure 22 shows the ASD of the PEM sensor background data.

We now discuss the projection of environmental noise into the DARM data during t_{fore}. For each PEM sensor studied by PEMcheck, we first linearly interpolate between the CF data points so that the frequency resolution of the CF matches the frequency resolution of the GW data. We then tune the CF for the sensor if the predicted level of noise in DARM due to the PEM data exceeds the actual level of noise during the background time. We next compute the ASD of the

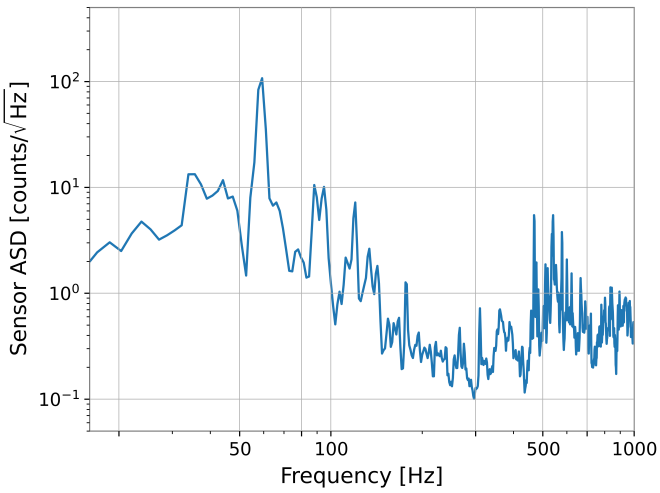


Figure 22. ASD of the Z-axis HAM 6 accelerometer during the background time. Background PEM sensor data is used to compute the tuned CF of section 4.1.3.3. 45.75 s of sensor data were used to calculate this ASD. Note that each sensor count corresponds to 6.1 μms^{-2} of acceleration in the vertical direction [165].

PEM sensor and DARM data using the prescription given in equation 4.3. Then, for each frequency bin in the PEM ASD, we compute the meters of DARM during the GW candidate caused by environmental noise via equation 4.2.

4.1.3.3 CF Tuning Sometimes the CFs used for PEMcheck overestimate the level of environmental noise present in the GW data. To reduce environmental noise coupling overestimation, we *tune* the interpolated CFs supplied to PEMcheck for each GW candidate. This process works by comparing $Y_{\text{noise}}(f)$ during the background time to the actual background time DARM ASD. At frequencies where the environmental noise ASD is predicted to exceed the DARM ASD, we reduce $CF(f)$ at those frequencies such that the predicted environmental noise is equal to the value of the DARM ASD at those frequencies. This process is illustrated in the top plot in figure 23. By reducing the CF at points where there is no evidence for the claimed coupling during t_{back} we limit the instances of overestimating environmental coupling.

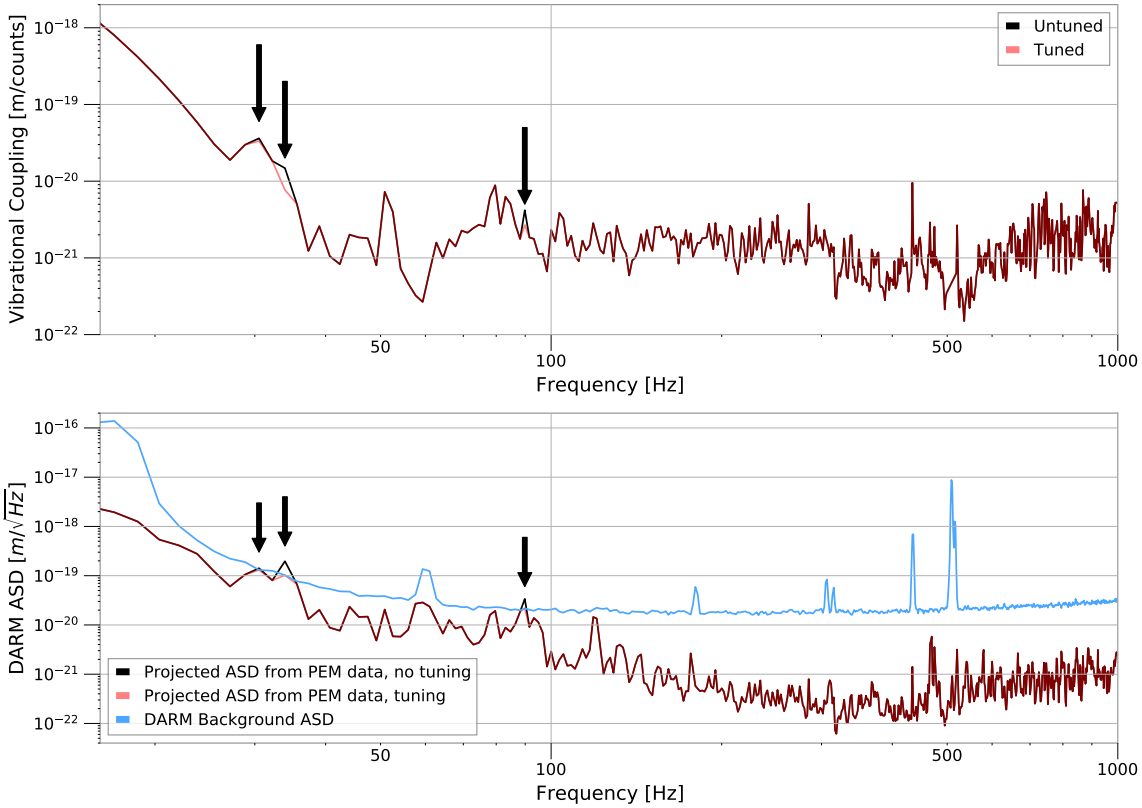


Figure 23. Top: Comparison of the CF interpolated from the data in figure 21 to the interpolated, tuned CF computed by analyzing the DARM background ASD. The untuned and tuned predictions for the ASD largely agree, except near 30 and 90 Hz. The points where environmental contributions to DARM are overestimated and need tuning are derived from upper limit estimates of the chamber motion to DARM coupling. These frequencies are marked with black arrows. Bottom: Comparison of the DARM t_{back} ASD with the estimated contribution from the HAM 6 accelerometer. The result of the tuning procedure is to constrain the predicted environmental contribution from a sensor to be not greater than the observed DARM ASD. As in the top plot, black arrows mark where the untuned CF predicts that the DARM ASD should exceed its observed value to the HAM 6 accelerometer data. These are the points which require tuning to reconcile the predicted and actual DARM ASDs.

Overestimating environmental coupling may lead to event validators spending additional time investigating noise sources identified by PEMcheck that are not truly present in the GW data. Typically this manual review process involves identifying transients in the PEM sensor data at the same frequency as the reported coupling and close to the GW candidate in time and checking whether the predictions for environmental noise contamination are consistent for these loud transients. There may also be difficulties interpreting the astrophysical parameters of a given GW event. The difficulty disentangling the effects of offline noise subtraction from novel features in a GW signal was highlighted in the context of noise subtraction due to glitches—not environmental noise—during O3 [118, 185, 186]. Event validators incorrectly prescribing noise subtraction due to PEMcheck overestimating the degree of environmental noise present in a GW signal may lead to similar parameter estimation issues in O4.

In the case of the LLO HAM 6 accelerometer and GW190707, the CF overestimates the level of environmental noise contribution to the DARM measurement, particularly between ∼30-40 Hz and near 90 Hz, as illustrated in both plots of figure 23. In this case, environmental coupling projections derived from upper limit estimates of the coupling, rather than measured points in the CF exceed the actual level of noise in the detector data. The coupling estimate is tuned at these frequencies to be consistent with the observed GW data. The tuning procedure reduces the need for manual vetting of GW signals by down-weighting spurious predictions like this one.

Disagreement between the HAM 6 accelerometer CF and the observed coupling could arise due to differences between the ASD used in calculating the reference ASD during sub–100 Hz vibrational and acoustic injections and the

background ASD data shown in figure 22 [111]. These differences may arise due to different noise sources being present in the data in March and April 2019, when the CFs were measured and July 2019, when that GW was observed. Additionally, commissioning efforts in the intervening months increased the low–frequency sensitivity of the LLO detector, further constraining upper–limit estimates of the environmental coupling where it was not measured.

By tuning each CF to account for the environmental noise and condition of the LIGO detector at the GW candidate time, we improve the accuracy of environmental noise contamination information presented to LIGO event validators compared to the information given to O3 event validation experts [111, 124].

4.1.3.4 c-statistic Determination From the ASD of the DARM data during the candidate GW event as well as the predicted DARM ASD curve due to environmental noise witnessed by a particular PEM sensor, we quantify the degree to which environmental disturbances may contaminate GW strain data.

Following equation 4.1, we divide the tuned CF by a factor of 4000 m (the length of the LIGO Fabry-Pérot arm cavities) to convert the CF from units of differential arm length per sensor unit observed to units of GW strain per sensor unit [24]. We then compute the spectrogram of the GW strain data during the foreground time as well as the spectrogram of the effective strain measurement due to environmental coupling for each PEM channel, as described in section 4.1.3.2. We denote the predicted value of the GW strain spectrogram tiles due solely to environmental contamination as $\mu(t, f)$, where

$$\mu(t, f) = \Big(CF_{\text{tuned}}(f)/L\Big) \times S_{\text{PEM}}(t, f) \tag{4.4}$$

and $S_{\mathrm{PEM}}(t, f)$ is the foreground-time spectrogram of the PEM sensor data. The predicted spectrogram is then compared to the spectrogram of the GW strain, which we denote as $h(t, f)$.

For frequencies where μ was computed using a measured CF, then—as mentioned in section 4.1.2.2—the probability of observing a strain h due to a local environmental disturbance is given by the log-normal probability density function with a standard deviation of $\ln(2)$, or

$$\rho(h, \mu) = \frac{1}{h(t, f)\ln(2)\sqrt{2\pi}} \exp\left(- \frac{\Big(\ln(h(t, f)) - (\ln(\mu(t, f))\Big)^2}{2\big(\ln(2)\big)^2} \right). \tag{4.5}$$

For frequencies where μ was computed using an upper-limit CF, we use a uniform probability distribution on the range $[0, \mu)$ to estimate the probability density function of observing the GW strain, i.e.

$$\rho(h, \mu) = \begin{cases} \frac{1}{\mu(t,f)} & \text{if } h(t, f) < \mu(t, f) \\ 0 & \text{otherwise.} \end{cases} \tag{4.6}$$

The strict limit on the probability density function here is because the pre-observing run PEM injections are unable to establish a coupling between the sensor data and the GW data at these frequencies. For GW strains that are larger than the stringent upper limits set on the coupling times the PEM sensor data, we assume that the likelihood of environmental noise coupling vanishes.

To describe the likelihood of environmental coupling near a GW event we define the contamination statistic, denoted by c, which quantifies the likelihood of recording a strain value in excess of $h(t, f)$ due to environmental noise alone. We compute it via the cumulative distribution function (CDF) of the distributions in equations 4.5 and 4.6. The c-statistic at each point in the GW spectrogram is given by

$$c(t,f) = \begin{cases} \frac{1}{2}\left[- \operatorname{erf}\left(\frac{\ln(h(t,f)) - \ln(\mu(t,f))}{\sqrt{2}\ln(2)} \right) - 1 \right] & f \in (f_{\text{meas}}) \\ \min\left(\frac{h(t,f)}{\mu(t,f)}, 1 \right) & f \notin (f_{\text{meas}}). \end{cases} \tag{4.7}$$

where f_{meas} denotes the set of frequencies at which the CF was measured, rather than an upper limit on the CF estimated. Here erf() is the error function and min() denotes the minimum of the two numbers.

The c-statistic is distributed over the range $[0, 1]$. A low c-statistic for a given sensor indicates that environmental disturbances witnessed by the PEM sensor could account for some of the data in the GW strain channel at a given time and frequency range. A high c-statistic indicates that it is unlikely that environmental noise witnessed by the PEM sensor is coupling to the GW data. Environmental contamination of the GW data is indicated by one or more sensors reporting low c-value, inconsistent with the low-noise case, where many sensors should report a c-statistic near 1. Results from computing the c-statistic many times over all the PEM data channels are shown in section 4.1.4.1. These distributions largely reflect the expectation for the distribution of the c-statistic for the null hypothesis (negligible environmental contamination), as discussed in section 4.1.4.1.

Not every spectrogram tile's c-statistic is relevant to determining whether there is environmental noise contamination in the GW strain signal. For instance, LIGO detected GWs at a maximum frequency of ∼693 Hz during GW190707; any environmental noise that was present in kHz frequencies, whether it couples strongly or not to the DARM measurement, should not affect the GW signal reconstruction. Therefore, we only consider the c-statistic for spectrogram tiles

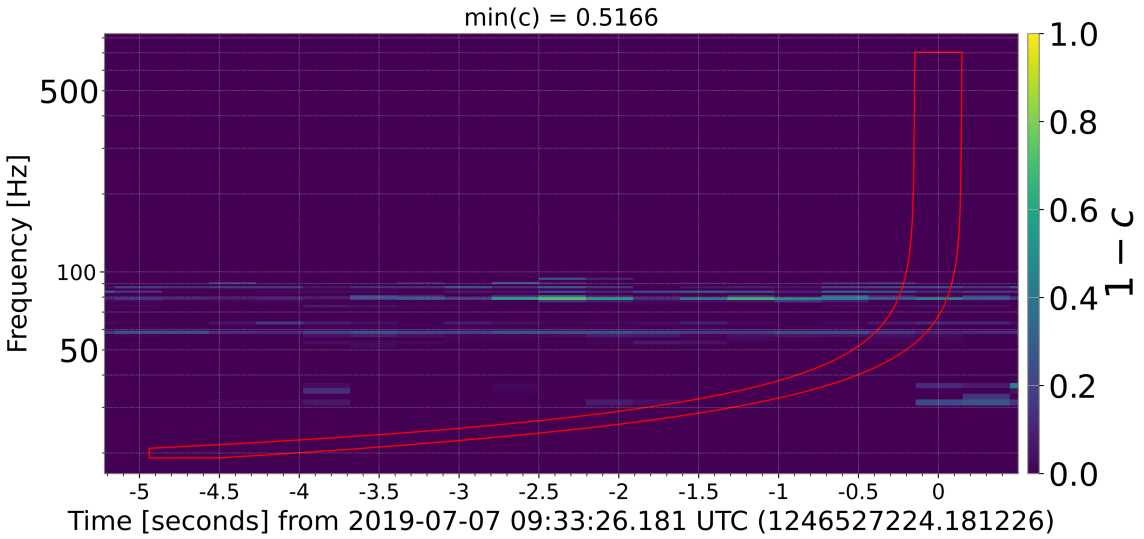


Figure 24. The results of the c-statistic calculation for each spectrogram tile for the LLO HAM 6 accelerometer during GW190707. The value of $1 - c$ is plotted for each tile so that time-frequency tiles with the highest likelihood of contamination, as calculated by PEMcheck, appear brighter. The time-frequency tiles enclosed by the red box track the evolution of the GW signal as predicted by NR. The lowest c-statistic found within the GW track occurs at ∼0.1 s and ∼78 Hz prior to the event's t_c. A minimum c-statistic of 0.52 indicates that it is unlikely that environmental disturbances witnessed by this sensor couple to the GW strain data during the event.

whose central frequencies are within 1–4 Hz of the time-frequency track predicted by the NR waveform approximant or the time-frequency "box" predicted by the GW burst search. The results of the c-statistic calculation for the LLO accelerometer during GW190707 are shown in figure 24.

4.1.3.5 Combining Results

PEMcheck reports to the user the time-frequency region with the lowest c-statistic from the entire collection of PEM channels analyzed. From the results presented in section 4.1.4, we find that a GW candidate with a minimum c-statistic of 0.2 or less for one or more PEM channels seems to be a reasonable threshold in O4 for follow up by environmental noise experts. This threshold identifies GW

candidates with the most significant evidence for environmental coupling while minimizing the number of events needed to be hand-vetted. If this threshold is too restrictive in O4, it may be changed. For each GW, a report may be automatically generated showing the time and frequency location of the minimum c-statistic tile near the GW data for each PEM sensor.

The coupling estimation process outlined here is valid only for linear coupling between one or more PEM channels and the GW data. Analyzing nonlinear coupling—where environmental disturbances at a particular frequency pollute GW data at a different frequency—is typically done from a glitch mitigation perspective, and is beyond the capability of PEMcheck at this time.

4.1.4 Results

4.1.4.1 Real GW Data We report the results of running PEMcheck on data from each LIGO detector around all 79 GW events detected by LIGO in O3 with a probability of astrophysical origin of 0.5 or greater [53, 54, 170, 187]. This amounts to 149 individual runs of PEMcheck, one per GW event per online LIGO detector. The sensor CFs determined prior to the start of O3 were used for the following analyses, with the exception of results presented in table 2.

We find that PEMcheck does not report a c-statistic of 0.1 or less for any of the 149 runs. The distribution of the minimum c-statistic for all 149 instances of PEMcheck is shown in figure 25. Figure 26 shows the cumulative distribution of c-statistics for all channels for all O3 events analyzed in this work. Overall, most GW events report a large c, or a low likelihood of environmental noise contamination. However, there are a few outliers in this set which merit further consideration. While all the steps involved with manually vetting GW candidates is beyond the scope of PEMcheck, it provides a starting point for where to look for

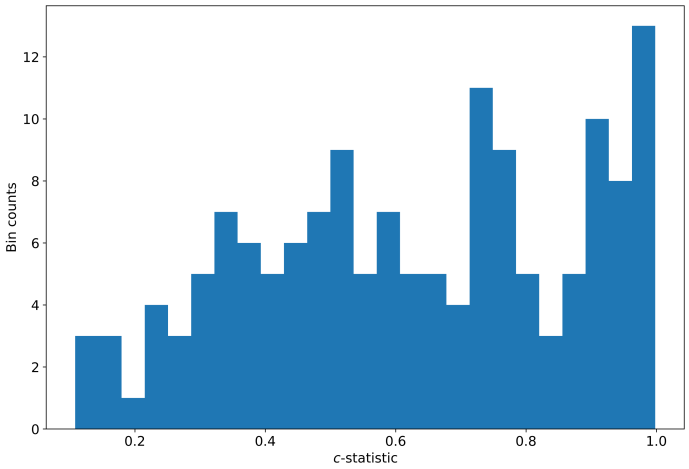


Figure 25. Histogram of the minimum c-statistic calculated by PEMcheck for all O3 events using the pre-O3 coupling data. The PEMcheck analysis identifies 6 of the 149 O3 GW events as having a minimum c below 0.2

.

evidence of environmental coupling. In sections 4.1.4.2-4.1.4.4 we discuss the events with the lowest minimum c-statistics in more detail.

We also find that the tuning procedure was frequently used to down-weight the predicted level of environmental contamination. Table 2 shows the number of events where the time-frequency tile with the highest likelihood of contaminating the GW data was derived from a tuned projection of the PEM channel coupling. The data indicate that the CFs found via the PEM injection procedure predicted realistic estimates of environmental noise about two-thirds of the time. However, about one-third of events had initial noise projections which were inconsistent with the actual DARM ASD and needed to be tuned. In many of these cases an upper limit estimate of the coupling, where no response to a PEM injection is seen in the GW data, turns out to overestimate the environmental noise. This is the intended utility of the tuning procedure. However there were also 22 instances of a measured coupling between a PEM sensor and the GW channel

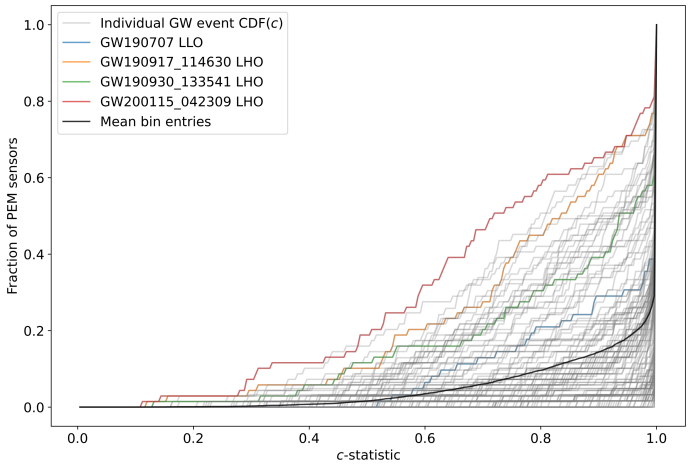


Figure 26. Cumulative distribution of the c-statistic found for each PEM channel studied by PEMCHECK for each GW event in O3 using the pre-O3 coupling data. The coupling analysis was performed on 63 PEM sensors at LLO and 72 PEM sensors at LHO. Each light grey trace corresponds to the CDF of the c-statistic for an individual GW event, while the black trace denotes the mean number of sensors with that particular value of c or less. GW190707 as well as the three events with the lowest c are highlighted.

overestimating the environmental noise contamination. Of these, 16 stem from a measured coupling at either 148 or 196 Hz between an accelerometer, H1:PEM-CS_ACC_ISCT6_SQZLASER_X_DQ, on the optics table which houses many of the components of LHO's squeezer. This accelerometer's coupling consistently needed to be tuned down at 148 Hz starting with GW190814, which was observed the day after the squeezer table configuration was modified due to the original squeezer laser failing [56, 188]. It is possible that the squeezer configuration changes affected the coupling between squeezer optics table motion and the GW channel. After reanalyzing the dataset with this sensor's CF as measured at the conclusion of O3, we find that only 7 minimum c-statistic tiles are derived from tuned, measured values of the coupling. None of the remaining 7 tuned, measured points stem from the LHO squeezer table vibrational coupling being overestimated. For these 7

Table 2. The number of O3 GW events where the tuning procedure was used in calculating the time-frequency tile with the highest likelihood of contamination. The type of point, measured or upper limit, in the worst coupling sensor CF at that frequency is also given. Most, but not all, tuning is done at frequencies where sensor CFs are given by upper limit estimates of the coupling. We compare the fraction of tuned, measured points identified by PEMcheck when the CFs measured prior to O3 are used to the fraction of tuned, measured points identified when the CF data for LHO's squeezer table accelerometer is replaced with the CF data collected after O3 for GW events occurring after August 13, 2019.

	Untuned		Tuned	
CF data used	Measured	Upper Limit	Measured	Upper Limit
Pre-O3	61	35	22	31
Pre-O3 except for LHO squeezer table	65	43	7	34

points, tuning reduced the predicted environmental noise in the GW channel by a median of 18% compared to the untuned prediction for the GW channel ASD at the worst coupling frequency.

The tuning procedure, which was designed primarily to provide better estimates of the coupling between a sensor and the GW data where the coupling could not be measured due to PEM sensor saturations, works as intended for the O3 events once the LHO squeezer accelerometer correction is applied. Event validation experts using PEMcheck no longer have to investigate unrealistically large claims of environmental effects in the GW data. Instead, this is now done automatically by the tuning process. In addition, tracking which measured values of the pre-run CFs are consistently need tuning during events may indicate to detector commissioners that changes to the instrument made during the run may have affected the environmental coupling of the detector and that some subset of the CFs must be re-measured.

4.1.4.2 GW200115_042309 The PEMcheck analysis of data near GW200115_042309 (hereafter GW200115) in LHO produced the lowest single *c*-

statistic of the entire dataset. This GW event, first reported in [60], is likely the result of a neutron star-black hole collision.

The time-frequency tile with the lowest c-statistic is located 0.144 s prior to the merger near 1417 Hz. The PEM channel which produced the lowest c-statistic tile is H1:PEM-CS_MAG_LVEA_VERTEX_XYZ_DQ with c =0.108. This channel is not recorded in LIGO GW frame files but is instead calculated by the PEMcheck code by taking the quadrature sum of three channels, each corresponding to a different axis of the triaxial magnetometer placed near the LHO beamsplitter which directs input light down the two interferometer arms.

We manually investigate magnetometer and GW data near the time-frequency tile identified by PEMcheck to evaluate the claim of environmental coupling. Comparing the constant-Q transforms of the strain and magnetometer channels, we find that there is some signal at that time and frequency in the magnetometer data [189–191]. However, there are other instances of magnetic signals at that frequency near the GW time which are more energetic which do not produce any response in the DARM channel. For this reason, we do not conclude that there is environmental contamination from the local magnetic environment in this instance. The difficulty associated with obtaining a measured magnetic coupling at high frequencies led to the environmental coupling being overestimated. The tuning procedure was not initiated in this instance; the upper limit estimate on the coupling in the region of 1417 Hz is characterized by a comb feature where the upper limit estimate of magnetic field to DARM coupling is considerably larger in a few Hz band. Above 1417 Hz, the coupling is tuned down, but this frequency happens to be the point in the comb that, when the projected ASD is calculated, comes the closest to the actual background DARM ASD

without exceeding it. Since PEMcheck's results are subject to human review, the apparent overestimation of magnetic coupling at this point would have been identified during the internal event validation process.

GW200115 also stands out as having many channels report a moderate c-statistic. Its CDF(c) is almost always the highest of all the other traces shown in figure 26. Of the sensors identified by PEMcheck with a $c \leq 0.7$, 10 corner station accelerometers report the highest evidence for coupling at 50–53 Hz at 3.64 s prior to the merger time. This is above the c threshold of 0.2 proposed as the value of the c-statistic needed to initiate manual review. To confirm that these channels are not coupling to DARM, we examine the distribution of c-statistics at nearby times to determine whether the collection of CS accelerometers at near-threshold c is exceptional. As illustrated in figure 27, the distribution of channel c-statistics changes little when PEMcheck is run using the same parameters inferred in low-latency for the time-frequency track at $\pm$10, 20 and 30 min from the actual GW time. Like the foreground time, the distribution of moderately-valued c-statistics is in each instance of the PEMcheck computation driven by corner station accelerometers. Ground motion at the corner station is heightened due to split mini air handling units operating in the time around the GW detection. No noise transients due to the air handling units are seen in the hour of strain data centered on the real GW event. The lack of evidence for environmental coupling by this channels indicates that that a minimum c of 0.2 or less is likely a reasonable threshold for manual review.

4.1.4.3 GW190917_114630 The event with the second lowest value of min(c) is GW190917_114630 at LHO. PEMcheck finds that the potential environmental contamination may be witnessed by the pair of triaxial

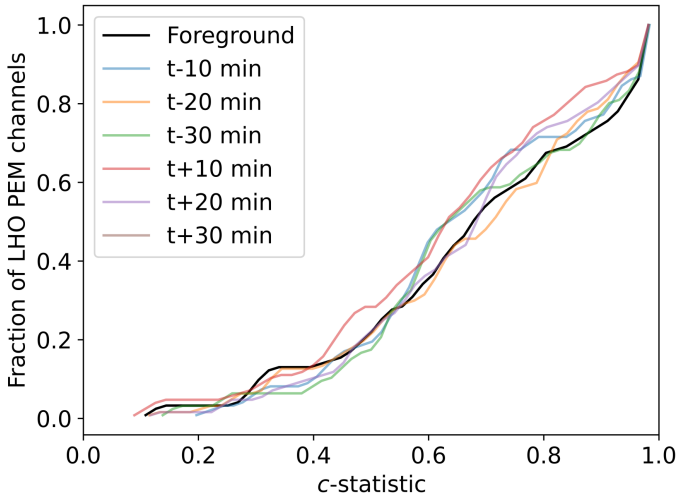


Figure 27. CDF of the c-statistic for each run of PEMcheck at LHO with GW200115's properties. The CDF marked "foreground" corresponds to PEMcheck run at the actual time of the GW event.

magnetometers located in the electronics room at end-X station (EX). The minimum c-statistic tile is at 837 Hz and 0.084 s after the merger time and has c =0.117. Following the same argument as in section 4.1.4.2, the constant Q-transforms of magnetometer and GW data do not support environmental contamination in the data. Again, poorly-constrained high-frequency magnetic CFs are responsible for overestimating the potential for environmental contamination in this case.

4.1.4.4 GW190930_133541

The final event with a low value of c we examine is GW190930_133541 at LHO. An LHO accelerometer monitoring motion of the vacuum enclosure which houses the signal recycling cavity at 50.6 Hz and 0.352 s prior to the merger time is responsible for the c-statistic of 0.129 for this GW event [117, 165]. This purported coupling is not supported by studying constant-Q transforms of the GW strain and PEM channel data near the event. The CF data for this sensor near the frequency identified by PEMcheck is set by

an upper limit estimate of the coupling, which is an order of magnitude estimate rather than a more precise measure of the coupling, as described in section 4.1.2.2. This could explain the discrepancy between the coupling projection and the lack of environmental coupling seen in the GW data from around the event. There is not support for environmental coupling for this event.

While the methodology of manual vetting of GW candidates is beyond the scope of this work, we present some arguments usually employed in the manual vetting process to establish that this event is free from environmental contamination from this PEM sensor. We compare constant Q-transforms of PEM sensor and GW data from the GW event time to look for occurrences of coincident high-energy transients in the two datastreams. These two Q-transforms are shown in figure 28. There are time-frequency tiles at 50.6 Hz in the accelerometer Q-transform with higher energy than the tile identified by PEMcheck as having the lowest c-statistic. Some examples of these transients are found at approximately $t_c-1.5$ s and $t_c+1.1$ s. There is no corresponding response to these transients in the GW data. These higher energy tiles were ignored by PEMcheck because they lie outside the calculated time-frequency track of the GW signal. Second, we investigate the frequency-domain behavior of the signal recycling cavity beamtube accelerometer to see whether it is exceptional in some way near the time of GW190930_133541. Longer-duration spectrograms of channel data indicate that the accelerometer is not witnessing any extraordinary environmental noise at 50.6 Hz during the event time. Lastly, the estimated ambient noise level witnessed by this sensor at this frequency is close to the GW sensitivity when projected into GW data [111, 165]. Because of this, random fluctuations in the PEM ASD data should occasionally lead to claims of coupling that need to be followed up on.

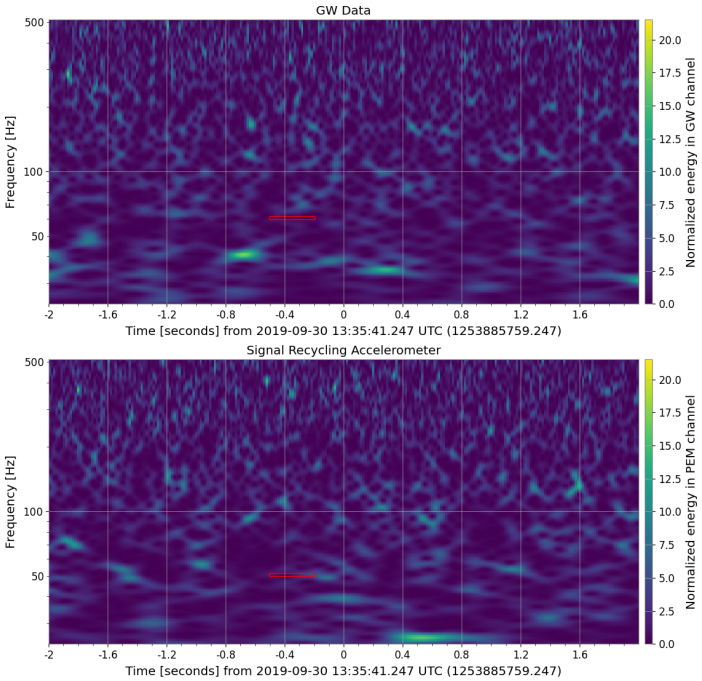


Figure 28. Constant-Q transform of LHO GW strain (top) and signal recycling cavity beamtube accelerometer (bottom) data centered on GW190930_133541's arrival time. A red box is overlaid on each plot showing the time-frequency window identified by PEMcheck as having the highest likelihood of coupling. Higher-energy transients in the accelerometer compared to the tile flagged by PEMcheck appear in the accelerometer data but do not correspond with transients at 50.6 Hz in the GW data. This indicates that CF is overestimating the coupling at this point and that the data is not subject to environmental contamination. Furthermore, the coupling estimate by PEMcheck is driven by the transient beginning near $t_c - 0.2$ s, but the NR-approximated inspiral waveform lies at a higher frequency by the time this transient appears.

Table 3. Estimates of source frame masses and dimensionless spins for GW190521 taken from [58]. These parameters were used to generate the tracks in figure 29. No specific t_c is given, as it differs for each of the 37 GW tracks in the analysis.

Progenitor property	Value
$m_1/M_\odot$	85
$m_2/M_\odot$	66
χ_1	0.69
χ_2	0.73

4.1.4.5 Simulated GW Signals We examine the performance of PEMcheck in an extreme scenario: one or more pipelines claim detection of a GW during a period of high environmental contamination of the DARM data. Thunderclaps can induce a signal in DARM by abruptly increasing ground motion in the tens of Hertz band [111, 124]. An especially loud thunderclap was visible in DARM as well as accelerometers located at LLO's EY station in May of 2019 [192]. We consider the results of running PEMcheck on 37 hypothetical GW signals with the properties of GW190521_030229 (hereafter GW190521) occurring during this particular thunderclap. The properties of GW190521 used for this analysis are given in table 3.

We find that PEMcheck routinely identifies a low c in the fictitious GW signals during the thunderclap shown in figure 29. The frequency identified as the likeliest one to be contaminated is 48±2 Hz in each trial. The tiles with the most normalized energy in the 40–50 Hz band correspond to GW strains of 2.54×10^{-22}. During the thunderclap, the L1:PEM_EY_ACC_BSC5_ETMY_Y_DQ accelerometer recorded a maximum displacement of 1.22×10^{-8} m. Projecting this into the GW strain signal with the sensor's CF, we find that predicted strain value associated with that amount of sensor motion at that frequency is 2.36×10^{-22}. As a point of

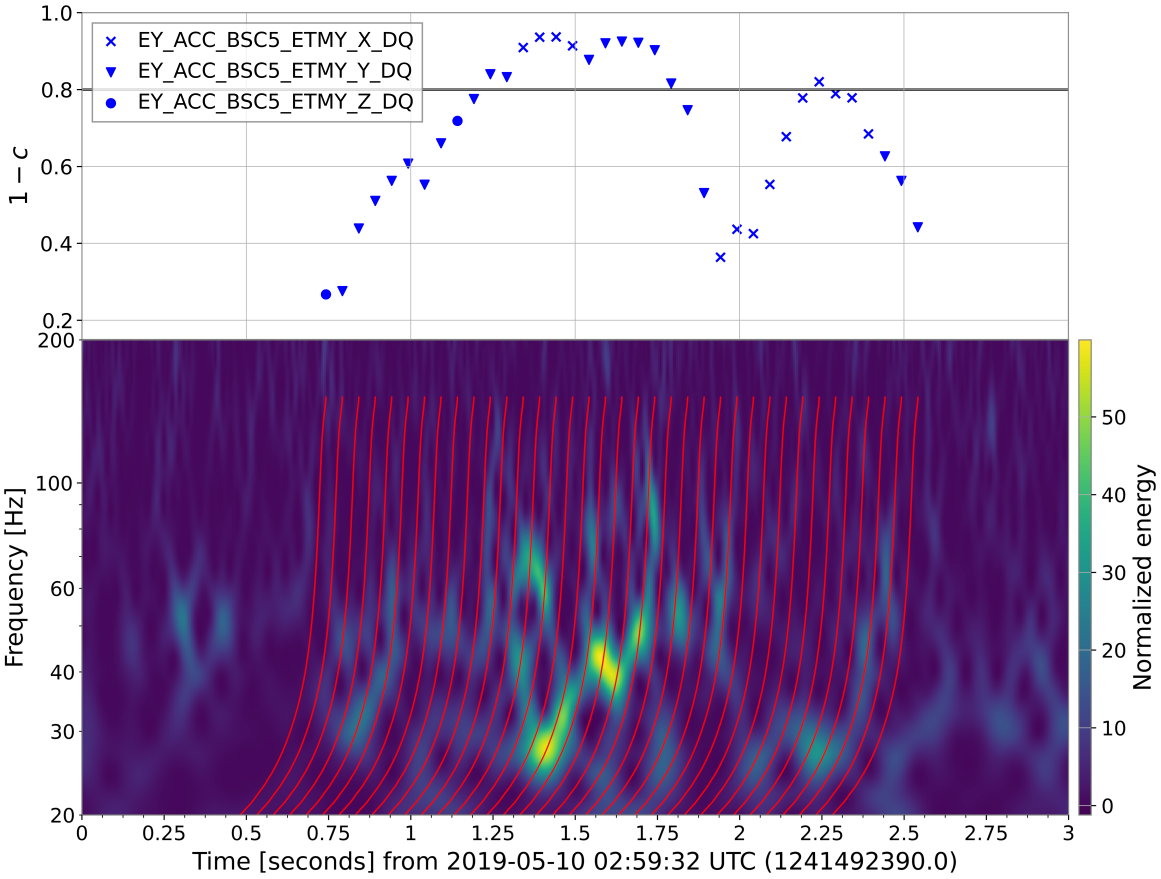


Figure 29. Below: constant-Q transform of LLO GW strain data during a thunderclap witnessed by PEM sensors. The 37 red time-frequency tracks overlaid on the thunderclap data represent 37 hypothetical GW time-frequency tracks with the properties given in table 3 vetted by PEMcheck. Above: the lowest value of c found by PEMcheck for the series of hypothetical GW tracks overlaid on thunderclap data. The channel with the lowest c-statistic for a given trial is denoted by the marker style. The bold line corresponds to $c = 0.2$.

comparison, GW150914's strain reached a maximum amplitude of 2.63×10^{-22} in the same frequency band [41].

Should an event validation expert see a GW candidate with multiple nearby sensors reporting a low c-statistic at similar frequencies, an appropriate recourse would be to contact environmental monitoring and noise subtraction experts for further analysis and study of the environmental noise background local to the candidate event.

4.1.5 Conclusions In this work, we have demonstrated the feasibility of the PEMcheck tool to identify potential coupling between the LIGO detectors and their environment for GW candidate events. PEMcheck uses CFs measured between PEM sensors and the DARM measurement to project noise witnessed by PEM sensors into the GW strain data stream and determine the likelihood that the GW data at a given time and frequency is a result of environmental noise. This is quantified by the contamination (or c) statistic.

We have tested the performance of PEMcheck by analyzing the 79 GW confident events seen by one or more of the LIGO detectors in O3. This amounts to 149 individual runs of PEMcheck. The events with the lowest value of the contamination statistic are studied in further detail. When subject to manual inspection, we conclude that the potential environmental coupling is not borne out in each case. This is juxtaposed with a clear case of environmental coupling caused by a thunder clap. From the results of running PEMcheck on real and simulated GW signals a criterion of $c \leq 0.2$ is suggested as the standard for initiating human review of PEMcheck results by event validation experts.

We show that PEMcheck is capable of warning event validation experts if there is substantial environmental coupling. We find that the tuning procedure

used by PEMcheck provides a rough estimate of the environmental coupling in real-time, reducing the demand for hand-vetting of events by environmental noise experts. However, claims of environmental coupling continue to be checked by hand in the case of a high likelihood of environmental contamination or detections of GWs from novel sources. PEMcheck is being used in the DQR to study environmental noise contamination in every GW observed by that LIGO detectors in O4.

Future directions for development may include closer integration with utilities for characterizing changes in sensor performance over time [193] and designing a framework for constraining coupling from PEM sensors using loud transients seen in those channels and not in DARM to further tune estimates of the CF, similar to the approach demonstrated in section 4.1.4.4 partially manually vetting GW190930_133541. The results of the tuning procedure should be tracked to motivate injected campaigns if CFs tend to become inaccurate as observing runs continue, especially in cases where upper limit estimates consistently need adjusting. Nonlinear coupling is not accounted for by current CFs and thus PEMcheck, but would be an important development for the future. A more rigorous approach to trials factors may improve the interpretability of numerical results. The limitations of this procedure, e.g. in PEM sensor coverage, will inform the designs for future GW detectors, such as Einstein Telescope and Cosmic Explorer, for which environmental noise will continue to be crucial to confront [194, 195]. Since the PEMcheck analysis requires CFs, sensor and DARM data, the same procedure used to search for evidence of environmental coupling could be used in these future GW detectors.

4.2 PEMcheck Performance in O4

4.2.1 Integration with DQR As described in 4.1.5, PEMcheck was integrated into the hour-tier O4 DQR, a set of data quality checks which are automatically run on significant GW candidates identified by search pipelines in either low-latency or offline operation. Should no data quality issues be identified, GW candidate information may be distributed to the public via NASA's General Coordinates Network if the GW data also satisfies separate criteria set by search pipeline maintainers and parameter estimation (PE) experts [196]. The criterion for automated DQR generation is the false alarm rate of the GW candidate. This is determined for each search pipeline via GW injection studies. In O4, the standard for a public alert, and thus DQR generation, is a GW candidate with a false alarm rate $\leq 3.9 \times 10^{-7}$ Hz (one per month) should the event be found with the highest significance by a modeled search or a false alarm rate $\leq 3.2 \times 10^{-8}$ Hz (one per year) in the case of an unmodeled search [197].

Data quality tools run by the DQR assess: whether the detectors involved in the detection were properly set to observing mode, the long-term behavior of the detectors prior to the event, whether a glitch overlapped the GW signal [151, 198–201], if noise in auxiliary channels could have affected the GW channel [121, 122, 140, 202], or if noise artifacts could have affected skymap generation. While one or more of these automated tools may indicate a data quality concern for a particular event, thanks to robust glitch subtraction tools [203, 204], that does not necessarily preclude circulation of a public alert, although a warning may be added to circular text cautioning users that inferred parameters may change subject to glitch mitigation.

4.2.2 Results PEMcheck was automatically run as part of the LIGO DQR on 228 GW candidates in O4 through April 1, 2025. Of these, 203 were not retracted in low-latency or as part of the event validation process. Because PEMcheck is run only on data from one detector in each instance, this represents 375 instances of PEMcheck being run in the subset of O4 analyzed here. Due to computing issues which were later resolved, PEMcheck was not run on one GW candidate at one detector: S231118an at LIGO Hanford [205]. Manual examination of PEM and strain data did not reveal any data quality concerns. Of these non-retracted candidates, there is no evidence for significant environmental contamination witnessed by PEMcheck.

Figure 30 displays the minimum value of c found for each of these **375** instances of PEMcheck. 25 GW candidates had c-statistics which merited human review of the data. The overall performance of PEMcheck is shown in figure 31. Candidate events with low c-statistics were vetted in a similar vein to the vetting procedure described in sections 4.1.4.2-4.1.4.4. Typical causes for claims of coupling include ambient noise in PEM sensor data which does not couple, but is too quiet to be sufficiently tuned away, loud signals seen by floor-mounted accelerometers not seen by nearby sensors mounted to vacuum chamber walls and poorly constrained upper limit estimates for magnetic coupling in the kHz regime overestimating the noise in DARM.

4.2.2.1 S230524x S230524x was a retracted event detected by an early warning search pipeline. These pipelines search at low frequencies for the minutes-long inspiral of BNSs and can produce an alert to be sent out to external observers prior to the actual merger occurring. Ordinarily, the inspiral and chirp from the BNS merger are also detected by other, full-bandwidth search pipelines. Should the

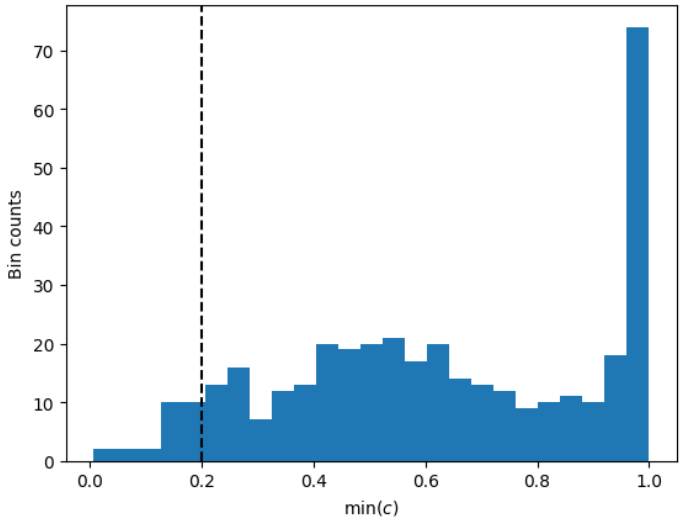


Figure 30. Histogram of the minimum c-statistic found by each PEMCHECK run in O4 through April 1, 2025. The vertical dashed line denotes $c = 0.2$, the threshold for manual follow-up of PEMCHECK results.

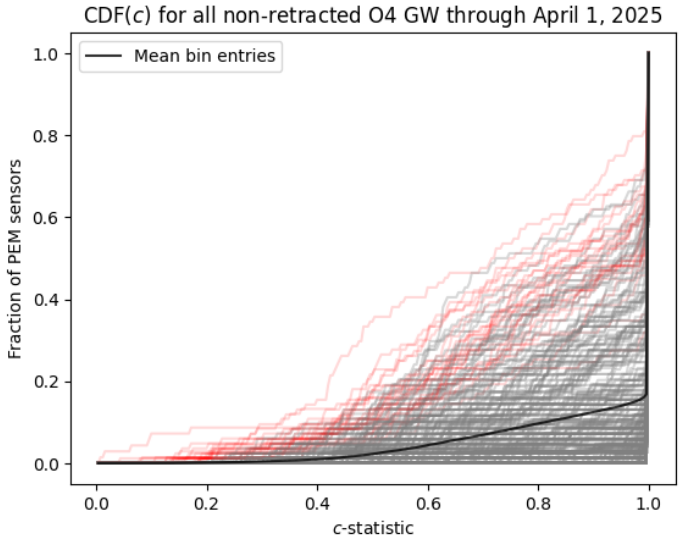


Figure 31. The results of PEMCHECK for each PEM channel for each event in the subset of O4 considered in this work. Light grey traces show $CDF(c)$ for each candidate event, while red traces represent the CDFs for the 25 runs of PEMCHECK with c-statistics below the threshold for review.

full-bandwidth detection not occur, a GW candidate event is not supposed to be produced. However, a computer bug caused a GW candidate to be generated from the early warning search trigger alone, even though no search found a chirp from the putative colliding BNSs. The lack of a full-bandwidth trigger caused the event to be retracted within minutes of the alert being generated.

Since an alert was produced for this event, PEMcheck was automatically run on this event. As shown in figure 32, numerous LHO corner station PEM sensors showed an extremely high likelihood of witnessing noise that could contaminate the strain data based on the sensors' CFs. The worst coupling time-frequency pixel for these sensors was ∼2.4 m prior to the merger time extrapolated from the event's parameters at 26 Hz. Examining spectrograms of PEM sensor data in this period showed a loud, sustained transient at these frequencies. This signal could be replicated by idling an observatory forklift near the output arm of the detector. Forklift activity was erroneously being conducted near the observatory while it was taking data [206].

4.2.2.2 S240624cd S240624cd was a GW candidate found only by an unmodeled search pipeline. Spectrograms of strain data from the LIGO and Virgo detectors surrounding the candidate are shown in figure 33. A statistical test indicated that there was an elevated likelihood of non-Gaussian noise in LLO strain data which was correlated with signals input arm accelerometers [122]. PEMcheck's results for this event agreed with this finding. Two accelerometers mounted to an input arm vacuum chamber, L1:PEM-CS_ACC_HAM2_PRM_Y and L1:PEM-CS_ACC_HAM2_PRM_Z reported a c of 0.020 and 0.000, respectively. The time-frequency tiles with these extraordinarily small c-statistics were located within the time-frequency region identified by the GW search itself. This high likelihood

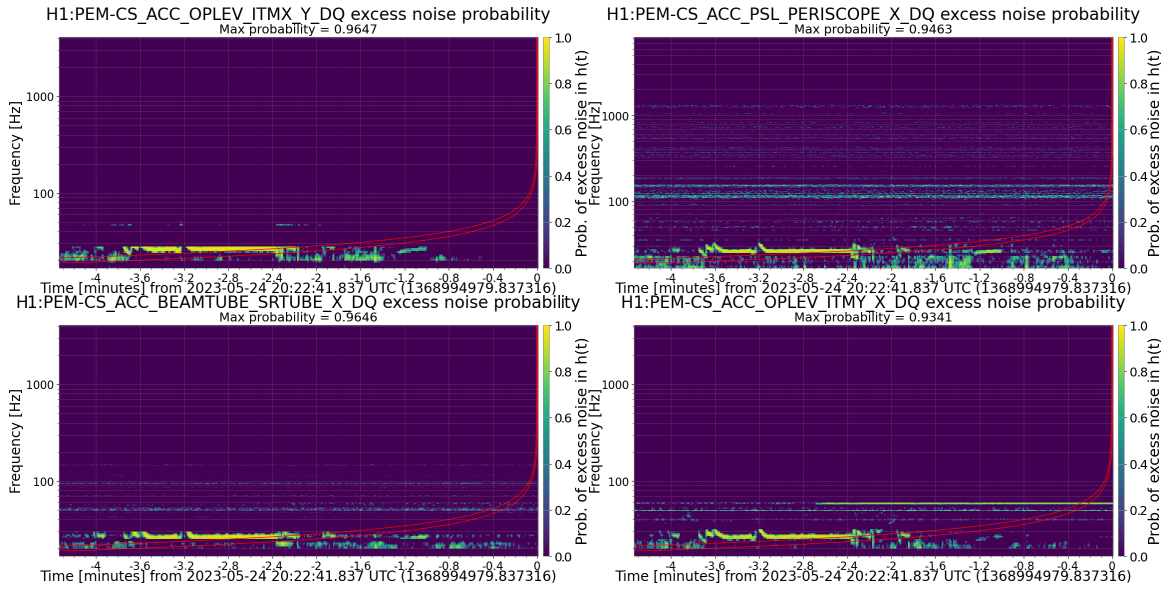


Figure 32. Likelihood of coupling for four LHO PEM sensors during a claimed BNS signal. Sensors in addition to the ones shown here reported a high likelihood for noise contamination.

of environmental noise was found to coincide with a transient of unknown origin witnessed by these accelerometers. Figure 34 shows accelerometer data near the GW candidate event.

It was found that the behavior of the search pipeline which identified this trigger was inconsistent between two realizations running on different computer systems. One instance of the search pipeline generated this trigger, while the other copy of the pipeline, using the same data as the first did not. The event was subsequently retracted. This event represents the first retraction of a high-significance GW candidate based in part on PEM information gathered and analyzed in low-latency. From initial alert to retraction circular [207], the process took less than 90 m.

Further study of this event revealed that the vibrational transient shown in figure 34 excited a vibrational mode of the HAM2 optics table suspension flexure.

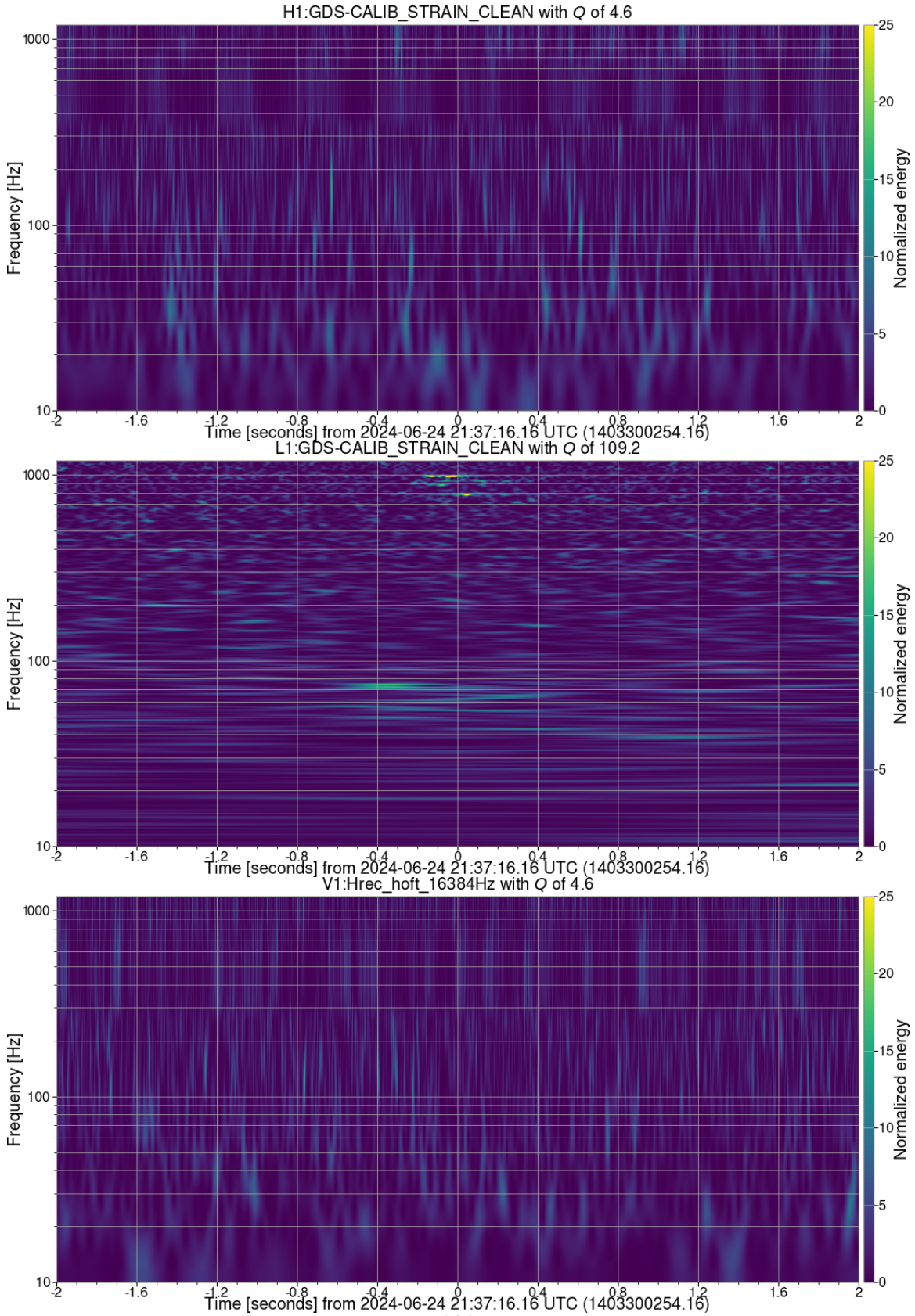


Figure 33. Strain data near the time of the unmodeled search candidate GW S240624cd. Data from LIGO Hanford (top), LIGO Livingston (center), and Virgo (bottom), the three observatories taking science-mode data at the candidate time are shown. Of note is the glitch in the neighborhood of the candidate time between

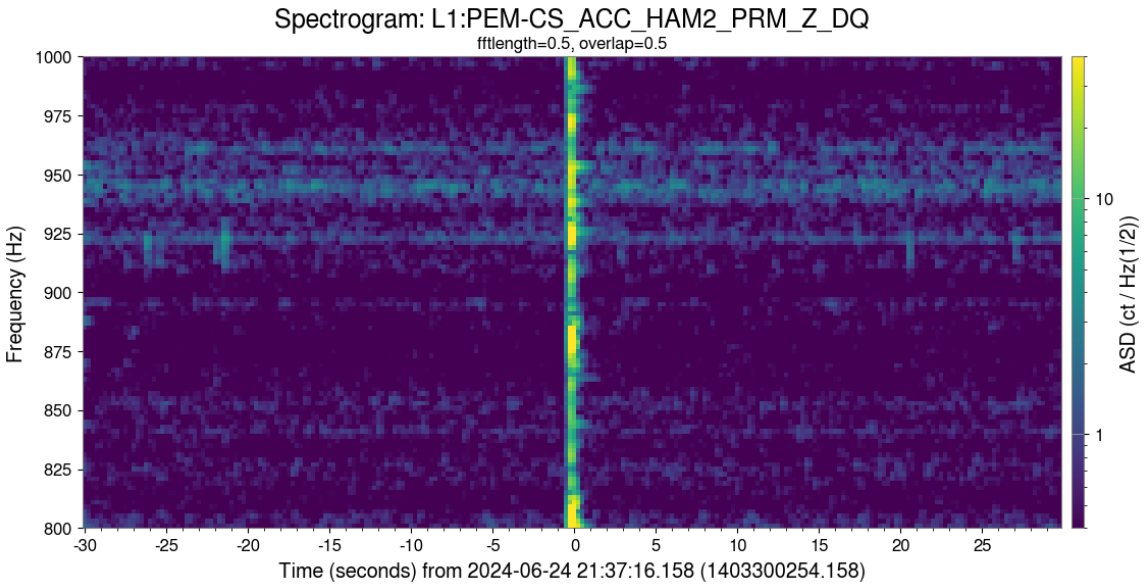


Figure 34. Spectrogram of accelerometer data near the GW candidate time. The claimed GW trigger's central time is set as $t = 0$ on the x-axis. The frequency range of the candidate according to the search pipeline was 883-971 Hz. The worst coupling tile found by PEMcheck for this sensor is located at (-0.2 s, 924 Hz).

Prior to O1, it was found that these flexures were some of the most dominant acoustic coupling sites at LHO [208]. Many flexures were subsequently damped on LLO optics tables to reduce this coupling [209]. However, the HAM2 flexures at LLO still remain undamped. In the course of this investigation, the CF procedure was extended to the Geotech Model S-13 seismometers which are mounted beneath LIGO optics tables. An example GS-13 CF is shown in figure 35

4.2.2.3 O4a All-sky Burst Search Candidates Two offline, unmodeled searches of LIGO data from the first part of the fourth observing were conducted to identify short- or long-duration GW signals via coincident excess power between detectors [68, 210]. While neither search identified new GW candidates with sufficient significance to claim a detection, PEMcheck was run manually on the highest-significance, non-CBC trigger identified by each

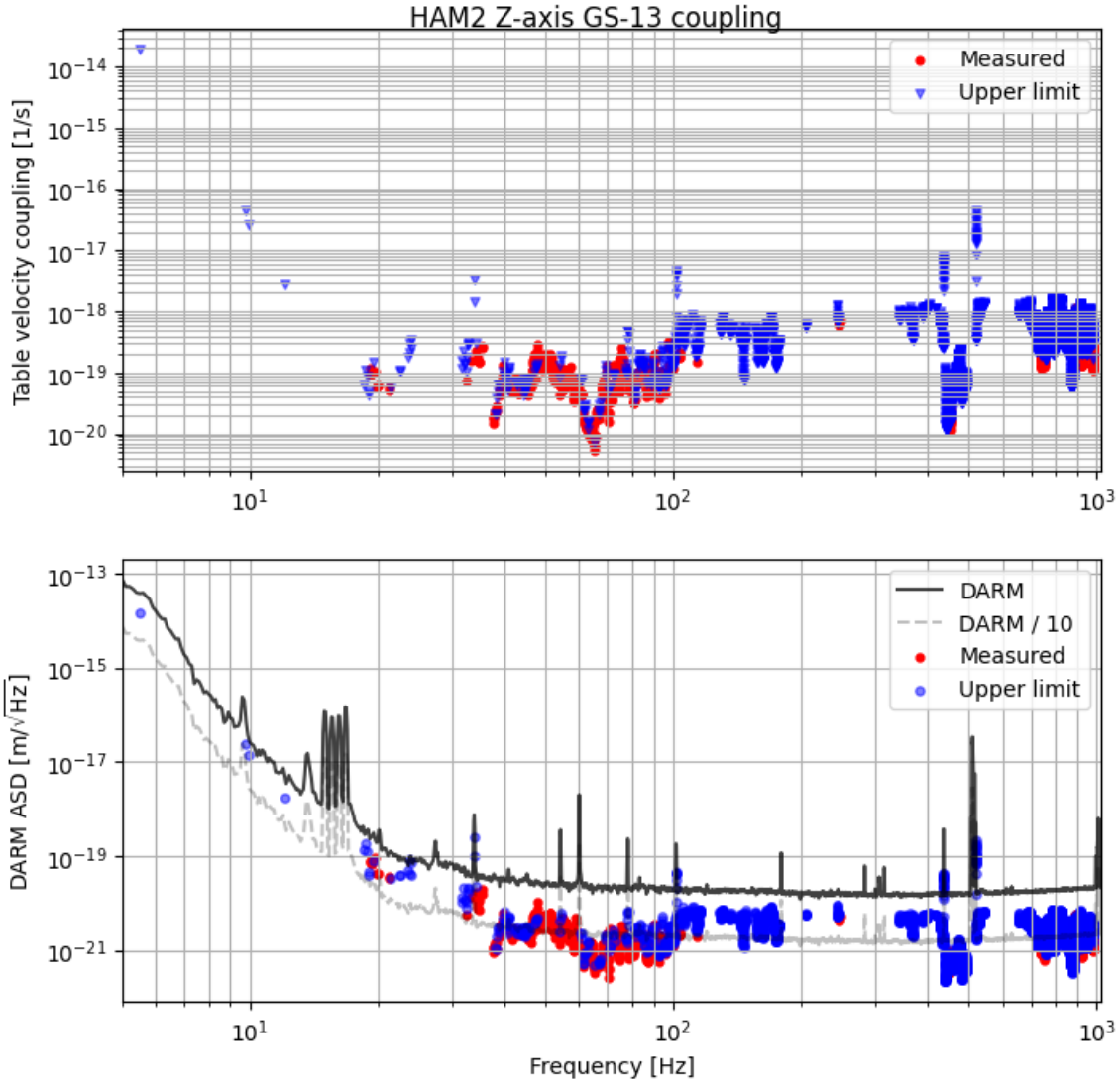


Figure 35. CF (top) and estimated ambient contribution to DARM (bottom) of a LLO GS-13 seismometer. Acoustic and vibration injection data from the pre-O4 campaign [135] was used to compute the GS-13 coupling.

search. Neither trigger showed significant evidence for environmental contamination witnessed by the PEM sensor network.

CHAPTER V

RESULTS OF THE SEARCH FOR COSMIC STRINGS WITH LIGO IN THE FIRST PART OF THE FOURTH OBSERVING RUN

"Look aloft!" cried Starbuck. "The copusants! the corpusants!"

—Herman Melville, *Moby-Dick* [211]

5.1 Search Method

Cosmic strings, should they be present in the universe, are potential sources of GWs. These GWs carry information about the energy scale η of spontaneous symmetry breaking that gave rise to the cosmic strings. Following the conventions for q, which encodes the source type, described in chapter 2.2.2.5, the amplitude of GWs from CSs is given by equation 2.71. The string tension in this expression is proportional to η^2. Therefore, detecting one or more bursts of GWs from cosmic strings could restrict the classes of allowable higher-energies theories which produce the Standard Model in the low-energy limit.

Should a CS not be detected, Poisson statistics can be used to exclude values of string tension which should have produced a sufficiently high-amplitude burst of GWs to be detected by LIGO, given predictions for the number density of CS loops and their GW burst rate [212].

5.1.1 Search Pipeline The CS search in LIGO is realized via a matched-filter search in single-detector data. Search results from multiple detectors are combined and only GW coincident triggers identified by the matched-filter searches are considered for further analysis. Additional trigger parameters, such as the difference in arrival time between detectors or the χ^2 of a given trigger are compared to the distributions of these parameters for known noise sources

and known CS signals in synthetic data [213]. GW triggers identified via this method are the likeliest string candidates. Specific steps in this process are shown in figure 36. The following section details the processes and configurations of individual tasks identified in this flowchart. In this chapter, only the search for GWs from CS cusps is considered.

5.1.2 Search Configuration The search algorithm is largely unchanged from the search described in [106]. It was run on the HTCondor [214, 215] workload management system for high throughput computing using a directed acyclic graph manager [216] generated using utilities in the LIGO Algorithm Library Suite (LALSuite) [217].

5.1.2.1 Data Acquisition and Timesliding O4a ran from 15:00:00 UTC May 24, 2023 to 16:00 UTC January 16, 2024. Of the detectors in the LIGO-Virgo-KAGRA network, only the two LIGO detectors were included in the data for the CS search. Virgo was being upgraded and commissioned during all of O4a and KAGRA ceased observation on June 20, 2023 to undertake upgrades. Time periods when both LIGO detectors were observing were identified. Times associated with category 1 data quality flags were removed from the analysis time [65, 218]. Once times suitable for analysis are found, the locations of corresponding GW frame files containing single-detector calibrated strain data on the LIGO Data Grid are identified.

The final step of the search pipeline relies on estimating the probability that a given GW candidate is due to a CS signal given $\vec{d}$, the strain data witnessed by the two observatories. This is computed via Bayes' theorem: CS signals are injected into detector data to estimate $P(\vec{d}|\mathrm{CS})$ from the population of recovered injections and the response of the detectors due to noise transients in the detectors

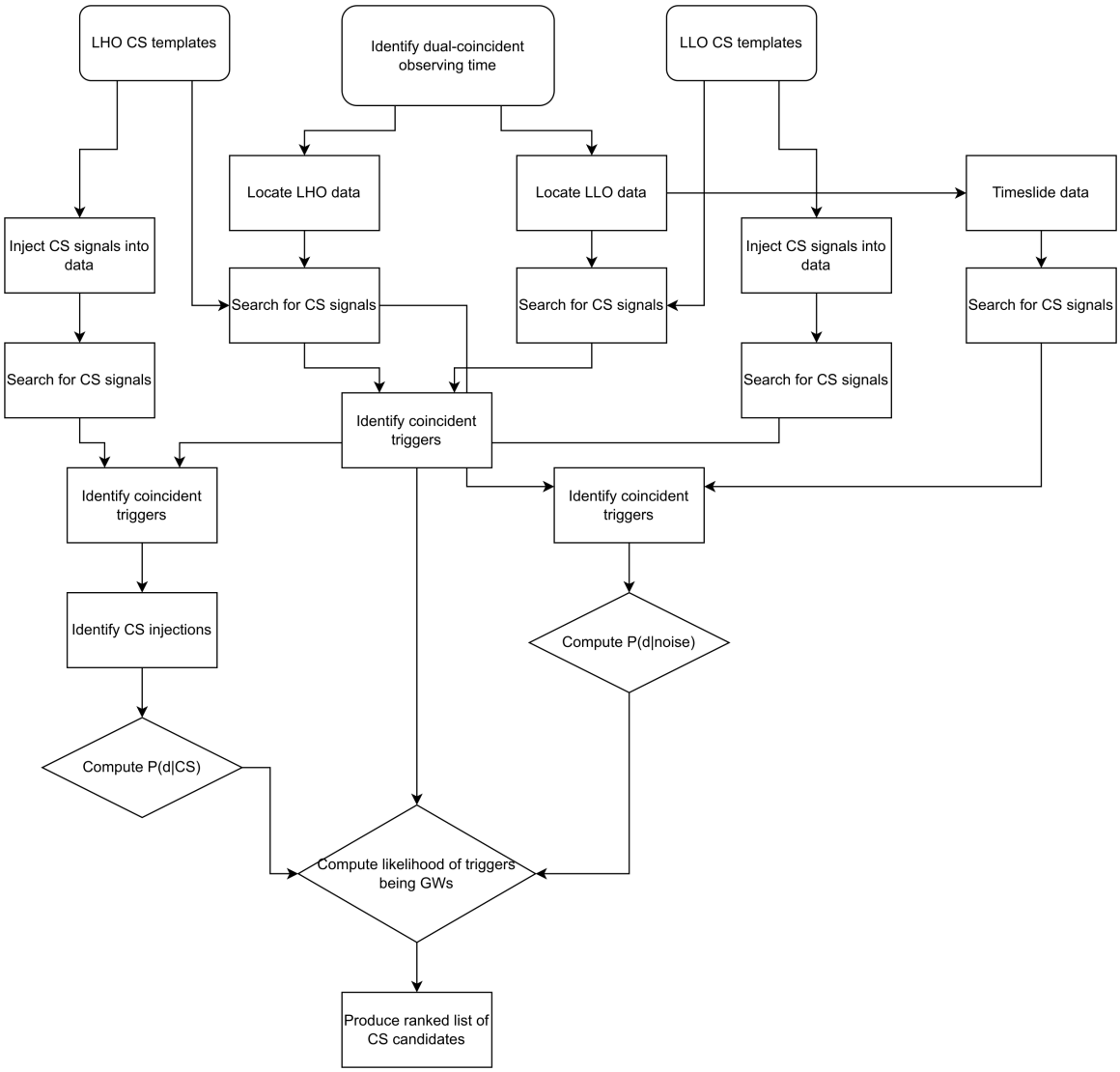


Figure 36. Flowchart of tasks used to find CS candidates in LIGO data.

is computed via establishing a set of triggers guaranteed not to be of astrophysical origin to estimate $P(\vec{d}|\text{noise})$.

The known-CS and known-noise trigger populations are generated by timesliding detector data. For the former, strain data from LLO is time-shifted by 78.76 s. This ensures that noise should not be correlated between the two detectors. GWs are then added to each detector's strain data. For the latter, the population of noise triggers is built up by performing 150 timeslides of LLO data, each one offsetting LLO strain data from LHO by 3.54 s. Since 3.54 s is much greater than the light-travel time between detectors, any coincident triggers found later by the search must be due to coincident—once the timeslide is applied—noise occurring in both detector's strain data.

5.1.2.2 CS Template Bank Preparation and Injection The CS search employs a matched-filter search for CS signals in single-detector data. For a given frequency-domain GW waveform, $h_{\text{template}}(f)$, the matched-filter SNR is [219]

$$\rho = 4\Re \int_0^\infty \frac{s(f)h^*_{\text{template}}(f)}{S_n(f)} e^{2\pi i f t_0} df. \tag{5.1}$$

with $s(f)$ the frequency-domain strain data composed of noise and the putative GW signal in the detector and $S_n(f)$ the one-sided power spectral density of detector strain noise surrounding the signal time. Whenever the SNR exceeds some threshold value, the search identifies a candidate surrounding the SNR peak. To increase the sensitivity of the search, multiple templates are used and the SNR associated with each $h_{\text{template}}(f)$ is continuously computed.

The GW waveform used is the CS completely +-polarized cusp waveform implemented in LALSuite:

$$h_+(f) = Af^{-4/3}\left(1 + \frac{1\ \mathrm{Hz}^2}{f^2}\right)^{-4} \times \begin{cases} e^{1-f/f_h} & f > f_h \\ 1 & \text{otherwise} \end{cases} . \tag{5.2}$$

The template bank used for the single detector search is the smallest collection of CS waveforms, differentiated from one another by varying f_h, such that the SNR loss due to template mismatch is less than 0.1%. Increasing the number of templates used beyond this threshold would increase the time required to conduct the search. Using the square of the O4a ASDs shown in figure 2, the template banks used for the O3 search which consisted of 31 waveforms did not satisfy this criterion. Therefore, the template bank used for each detector had to be iteratively constructed following the method described in [212].

Since the hour with the best BNS range was used to build the O4a template banks, the performance of these template banks had to be tested on data from other times to verify that the mismatch criterion was met. A single-detector search was conducted at LHO and LLO from observing mode data with good data quality from 15:00:00 UTC May 24, 2023 to 15:00:00 UTC June 24, 2023. Each search job covered a maximum of 3,584 s of observing time, amounting to 420 individual search jobs at LHO and 431 jobs at LLO, representing ∼15.0 and 15.7 days of single-detector observing-mode time, respectively. The SNR mismatch realized for each template for each search job was stored and checked to see that none exceeded the 0.1% threshold. A selection of the mismatch distributions is shown in figure 37. In contrast with O3, 42 templates were needed at LHO and 41 templates were needed at LLO to meet this criterion. The collection of waveforms used in each detectors template bank is shown in figure 38. The maximum mismatch found at

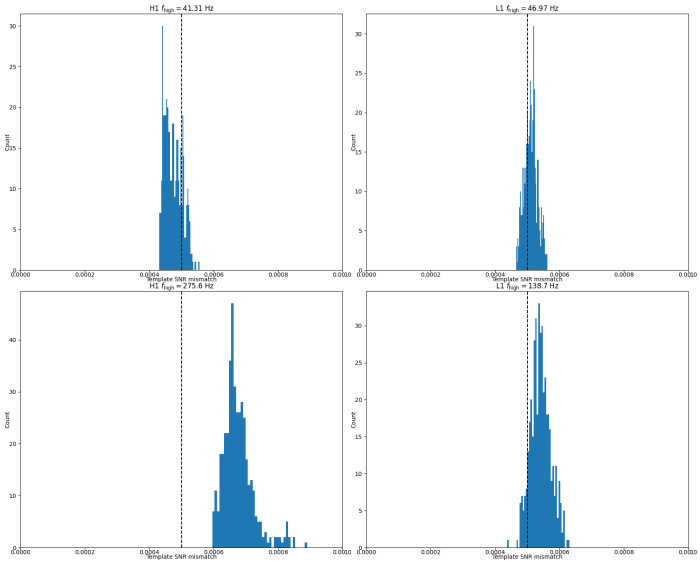


Figure 37. Distribution of the SNR mismatch found for four CS cusp templates in the ∼400 up to hour-long searches conducted at LHO and LLO. The vertical dashed line indicates a mismatch of 0.05%, the target for maximum SNR loss due to mismatch between CS signals and their nearest templates used to construct the template bank on the highest-sensitivity data.

LHO was 0.092% and the maximum mismatch found for the LLO template bank was 0.064% in the testing data.

To the strain datasets used to compute $P(\vec{d}|\text{CS})$, CS cusp signals were added to interferometer data every 83.7 s. This ensures that the GW signals are sufficiently separated in time so as to not interfere with the identification and analysis of one another. Injection parameters were chosen randomly with a $f_h \in [40,\ 4,096]$ Hz and $A \in [2 \times 10^{-22},\ 3 \times 10^{-19}]$ $\text{s}^{-1/3}$.

5.1.2.3 Single-Detector Search To conduct the single-detector search, the strain timeseries of each detector was read from its location in GW frame file storage. This data was down-sampled to 8,192 Hz and triggers with a minimum f_h of 30 Hz were identified using equation 5.1. Only data above 16 Hz was considered in the search. This choice of search starting frequency was motivated by being low enough to capture the lowest sensitive frequencies of the detectors, where most of

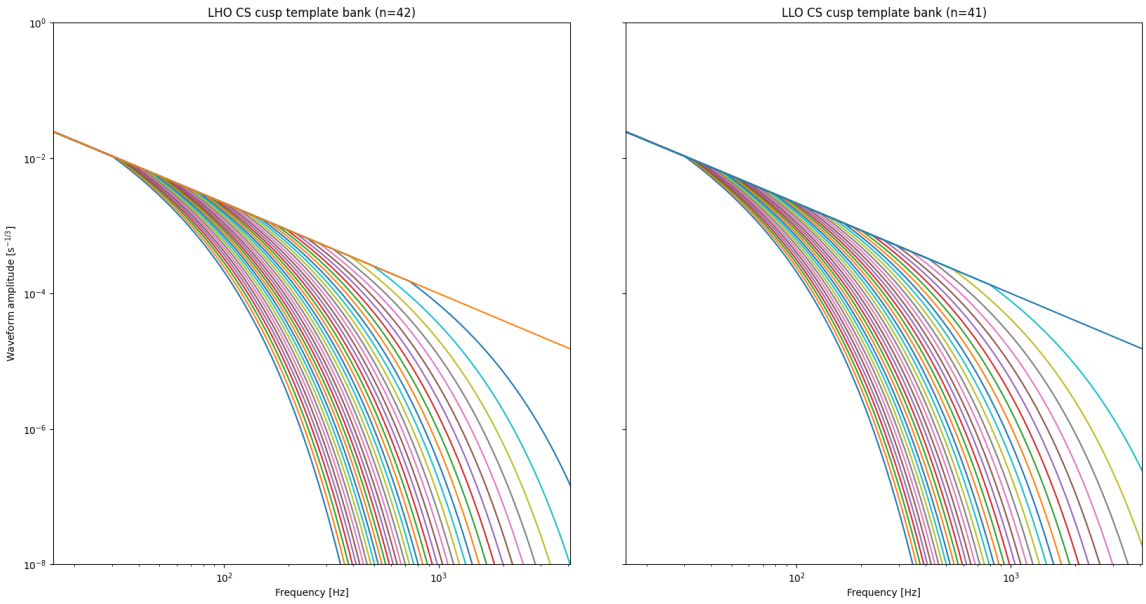


Figure 38. Template banks used for the O4a search. Each color represents a different $h_{\text{template}}(f)$, or equivalently, a different choice of f_h. The actual waveform amplitude used when conducting the search is rescaled to fit the amplitude of variations in $s(f)$. Here, the amplitude is chosen such that it equals 1 $\text{s}^{-1/3}$ at 0 Hz.

the CS signal amplitude resides, while being high enough to exclude low-frequency non-stationary noise and glitches. Adopting 16 Hz was justified by running the CS search on two weeks of O3b data with varying values for the search starting frequency and comparing the sensitivity of the search to the results presented in [106]. The results are shown in figure 39.

Each string search task, which examined up to 3,584 s of data from one observatory, produces a list of triggers identified via the matched filter process with an SNR of 3.75 or greater. This list includes the start time and duration τ of each trigger, its bandwidth and central frequency, its amplitude, SNR and the output of a χ^2 signal consistency test. This χ^2 test, developed in [220], compares the frequency-domain response of the detector to the GW trigger to the expected response of the detector to the waveform template used to identify the trigger.

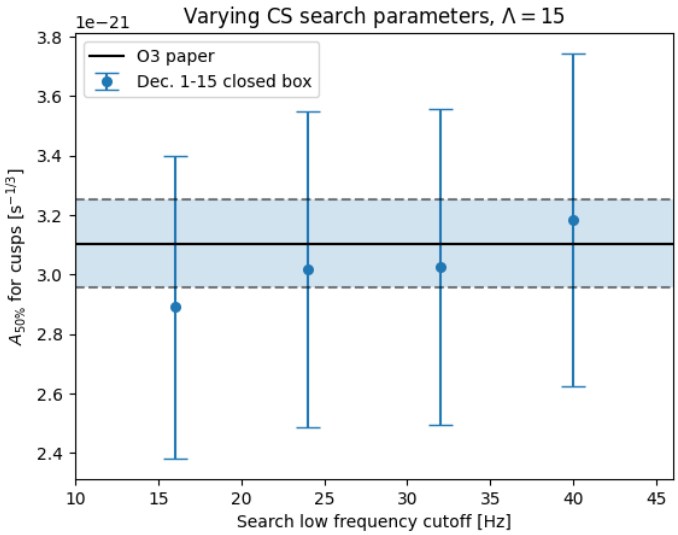


Figure 39. Variation in the CS search sensitivity for different choices of the search starting frequency. The GW amplitude at which 50% or more of injections are recovered with a log-likelihood≥15 increases with increasing search starting frequency. This indicates that more stringent constraints on $G\mu$ are achieved by selecting a lower frequency, such as 16 Hz, to begin the search at. Results from multiple pipeline configurations are compared to the results published in [106].

Detector noise, for example, could be loud enough to cause a trigger. However, the frequency-domain behavior of that noise should likely differ from a CS waveform, especially at moderate frequencies.

5.1.2.4 Coincident Trigger Identification

Once single-detector searches for the CSs complete, trigger lists from the two LIGO detectors are merged and compared against one another. Triggers which occur at both sites within the light-travel time between detectors, $\mathcal{O}(10$ ms), are kept for analysis. For the CS search run on timeslid data with CS signals injected into it, the times of coincident triggers are compared to the times when injections were made into interferometer data to identify which GW injections produced which triggers in the dataset while any other triggers are discarded.

5.1.2.5 Likelihood Calculation The synthetic data is used to study $P(\vec{d}|\text{CS})$ or $P(\vec{d}|\text{noise})$. $\vec{d}$ is the vector of trigger information for coincident triggers produced by the single-detector searches. The elements of $\vec{d}$ are as follows: the coordinates of each single-detector trigger in $(\chi^2,\ \rho^2)$ space, the coordinates of each single-detector trigger in $(\rho^2,\ \tau)$ space, the time difference between the trigger in LHO and LLO, the amplitude difference between the trigger in LHO and LLO and the f_h difference between the trigger in LHO and LLO.

The timeslide and CS injection processes establish the population statistics for each of the elements of $\vec{d}$ given the distributions of $\vec{d}$ that arise when only considering known CS signals and the distributions of $\vec{d}$ that arise when only considering known noise. Bayes' theorem, when applied in this context, states [213],

$$P(\text{trigger is signal}|\vec{d}) = \frac{P(\vec{d}|\text{trigger is signal})P(\text{trigger is signal})}{P(\vec{d})}. \tag{5.3}$$

Manipulating this expression shows that it is equivalent to

$$P(\text{trigger is signal}|\vec{d}) = \frac{P(\vec{d}|\text{trigger is signal})P(\text{trigger is signal})}{P(\vec{d}|\text{trigger is noise}) + \big(P(\vec{d}|\text{trigger is signal}) - P(\vec{d}|\text{trigger is noise})\big)P(\text{trigger is signal})}. \tag{5.4}$$

Defining the *likelihood ratio* $\Lambda(\vec{d})$ as [213]

$$\Lambda(\vec{d}) = \frac{P(\vec{d}|\text{trigger is signal})}{P(\vec{d}|\text{trigger is noise})}, \tag{5.5}$$

equation 5.4 can be rewritten as

$$P(\text{trigger is signal}|\vec{d}) = \frac{\Lambda(\vec{d})P(\text{trigger is signal})}{1 + (\Lambda(\vec{d}) - 1)P(\text{trigger is signal}))}. \tag{5.6}$$

Since $\frac{\partial P(\text{trigger is signal}|\vec{d})}{\partial \Lambda(\vec{d})}$ is everywhere positive, $P(\text{trigger is signal}|\vec{d})$ is a monotonically increasing function of the likelihood ratio [213]. Thus by computing $\Lambda(\vec{d})$, the triggers most consistent with real CS signals can be identified as those

having the highest likelihood ratio. In this case the likelihood ratio is computed as the product of independent probabilities of $\vec{d}$, that is,

$$\Lambda(\vec{d}) = \frac{P((\chi^2_{\mathrm{LHO}},\ \rho^2_{\mathrm{LHO}})|\text{trigger is signal})}{P((\chi^2_{\mathrm{LHO}},\ \rho^2_{\mathrm{LHO}})|\text{trigger is noise})} \times \frac{P(\Delta t_{\mathrm{LHO-LLO}}|\text{trigger is signal})}{P(\Delta t_{\mathrm{LHO-LLO}}|\text{trigger is noise})} \times \ldots. \tag{5.7}$$

In practice, a more useful quantity is $\log_{10}(\Lambda(\vec{d}))$. In the following discussion, when the likelihood or likelihood ratio is referred to, the logarithm of this quantity is what is meant.

Once the parameter distributions are determined for the synthetic data, the likelihood of triggers identified by the search algorithm in real data is computed. For each trigger's parameters, $\prod_i \frac{P(d_i|\text{trigger is signal})}{P(d_i|\text{trigger is noise})}$ produces the trigger likelihood. Information about the highest-Λ triggers are saved.

5.2 Search Results

The O4a cusp search was conducted on 126.0 days of dual-coincident, high-quality LIGO data, representing 53.1% of the total duration of O4a. Through the timeslide process, 103.4 years of background data was also generated and searched to improve search statistics.

5.2.1 Cusp Search Results The full-O4 cosmic string search is ongoing. Therefore, what is shown here are blinded results with the non-timeslid, non-injection data suppressed. The analysis results described herein could be used to justify unblinding the data at the conclusion of O4. In the absence of a claim of a detection or non-detection, blinded data can be used to estimate the sensitivity of the CS search and forecast the constraints it will set on new physics in the absence of a detection. The following results are drawn from the injection and recovery of 26,969,939 GWs into synthetic strain data as part of the search pipeline.

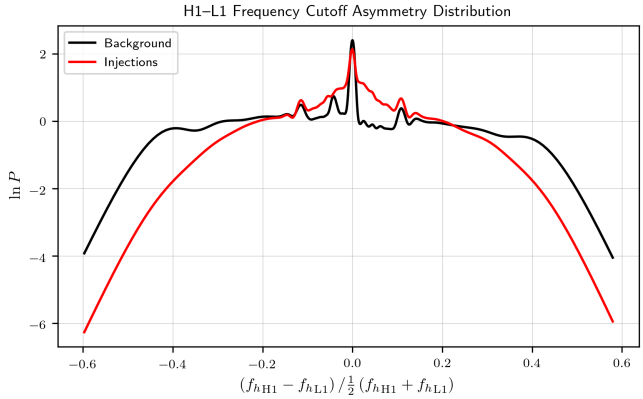


Figure 40. Difference in the f_h inferred from LHO and LLO strain data for the CS injections and the noise background.

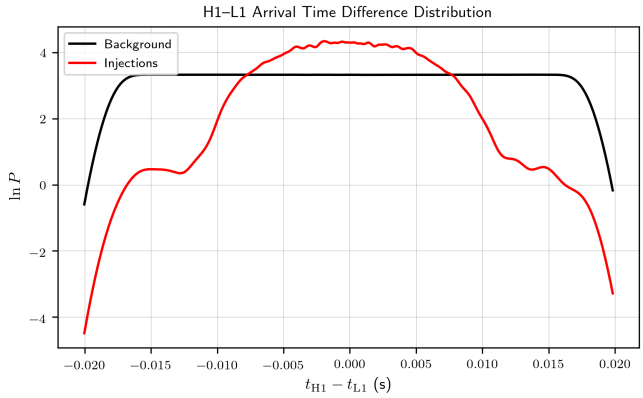


Figure 41. Difference in inferred arrival times for CS injections and CS triggers caused by noise at each LIGO site.

The likelihood ratio is calculated by comparing the distribution of $\vec{d}$ made by CS injections to the distribution generated by background noise. Figure 40 shows the distributions for f_h disagreement between observatories for the blinded data. Figure 41 shows the distribution of arrival times between these two datasets. Figure 42 shows the distribution of CS trigger amplitudes between sites. Figure 43 shows the single-detector two-dimensional histograms used to find $P(\chi^2,\ \rho^2)$.

Following the framework of [212], the most important metric for setting upper limits on the CS population is $A_{50\%}$, the GW amplitude at which 50% of

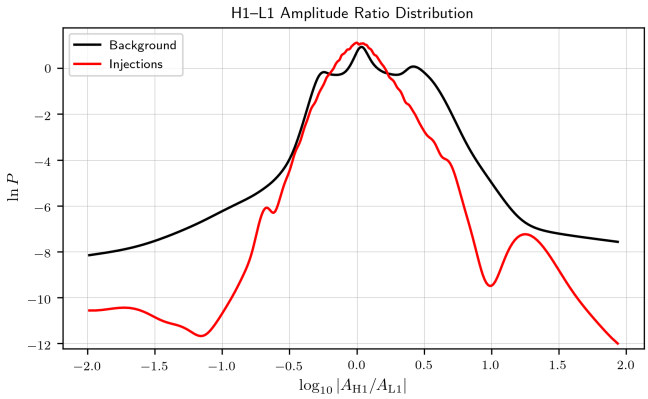


Figure 42. Discrepancy between detector amplitudes for triggers from CS injections and noise.

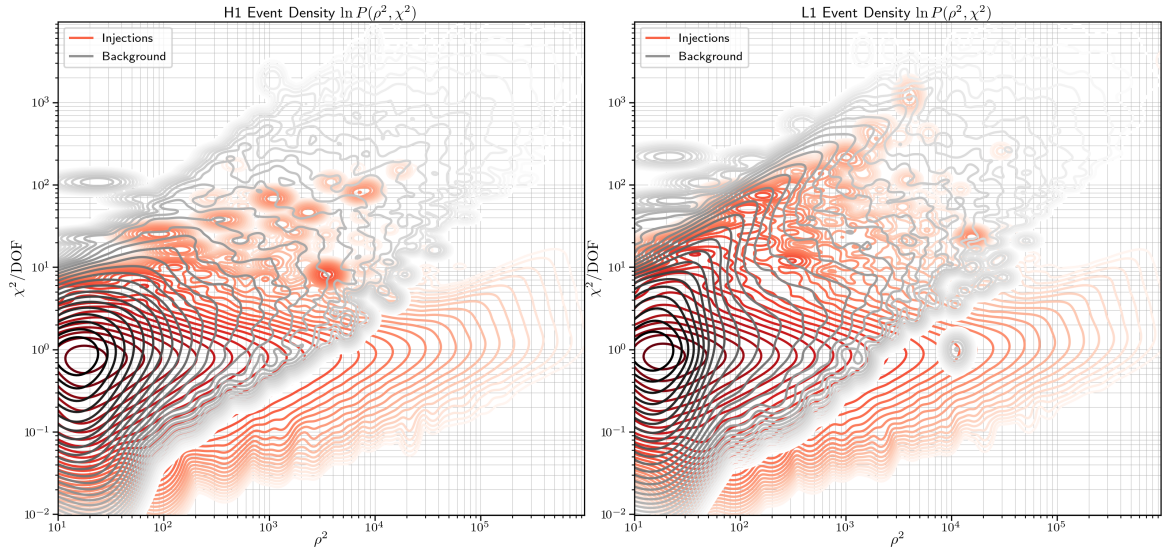


Figure 43. Single-detector signal consistency test results. Since the detector's response to a CS injection should closely resemble the response of the detector to a particular CS template, the reduced-χ^2 for injections is $\sim$1.

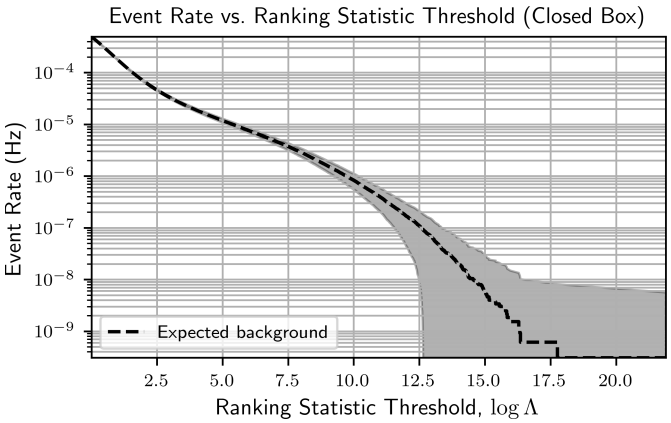


Figure 44. Rate of triggers with a given likelihood found in the O4a blinded results. A search duration of 126.0 days corresponds to a Λ of 12.65. The distribution of Λ is consistent with Poisson statistics, indicating that the search performed well and no major data quality issues were encountered.

injected GWs are recovered by the pipeline above its significance threshold. This significance threshold is found by identifying the value of Λ in the century-long background dataset which occurs with a rate of 1/126.0 days, the duration of the O4a search. The distribution of Λ is shown in figure 44. In the unblinded results, should a CS candidate be detected with high confidence, the black dashed trace in figure 44 would be pushed out to the right hand side of the plot.

Once the likelihood threshold is set, in this case to 12.65, the search pipeline identifies all the CS injections which were found with an Λ >12.65. As figure 45 shows, the recovery rate as a function of injected GW amplitude should increase sigmoidally. This is another indication that the search pipeline is working correctly. $A_{50\%}$ can simply be read from this. As shown in figure 45, the value of $A_{50\%}$ decreased ∼36% between O3 and O4a. This is due to the increased low-frequency sensitivity of the LIGO detectors in their O4a configuration, illustrated in figure 2.

Despite the 35.5% reduction in $A_{50\%}$ between O3 and O4a, some high-amplitude injections were still not recovered by the pipeline. The highest-amplitude

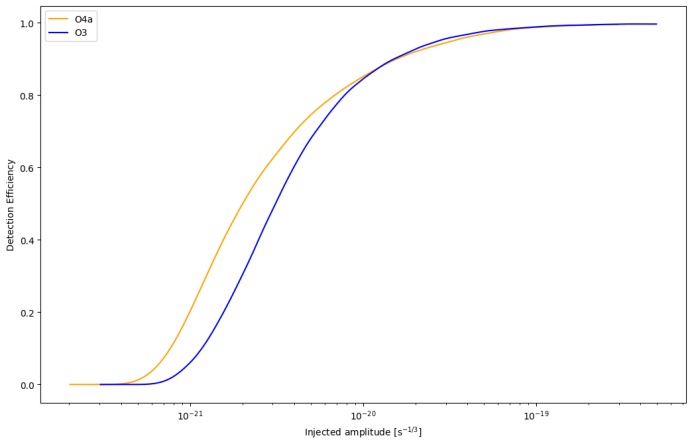


Figure 45. Comparison of $A_{50\%}$ for the O3 and O4a CS cusp searches.

injection which did not produce a coincident trigger had amplitude 3.0×10^{-19} $s^{-1/3}$. The large amplitude mismatch between detectors for this particular injection made identifying a coincident trigger challenging; the value of $\log_{10}|A_{\rm LHO}A_{\rm LLO}|$, the quantity plotted in figure 42, is -2.83. Such an asymmetrical amplitude could arise in a real scenario if a CS burst occurred in a region of the sky where LHO's antenna pattern was poor, while LLO's was good. On the other hand, injections with amplitudes as small as 3.4×10^{-22} $s^{-1/3}$ are occasionally recovered above the likelihood threshold.

Figure 46 shows the highest-ranked background trigger identified by the search. This trigger had a likelihood of 21.90. The CS is still susceptible to glitches; the transient at $\sim$+1 s at LLO is found by GravitySpy to be a tomte-class glitch with a 1.750 s duration.

5.2.2 Constraints on Cosmic String Population

5.2.2.1 Upper Limits Formalism If it is assumed there is no high-likelihood CS candidate in the zero-lag, non-injection dataset, properties of the CS population may still be probed. This is accomplished by comparing the detector efficiency curves of figure 45 against the burst rate predicted by different CS

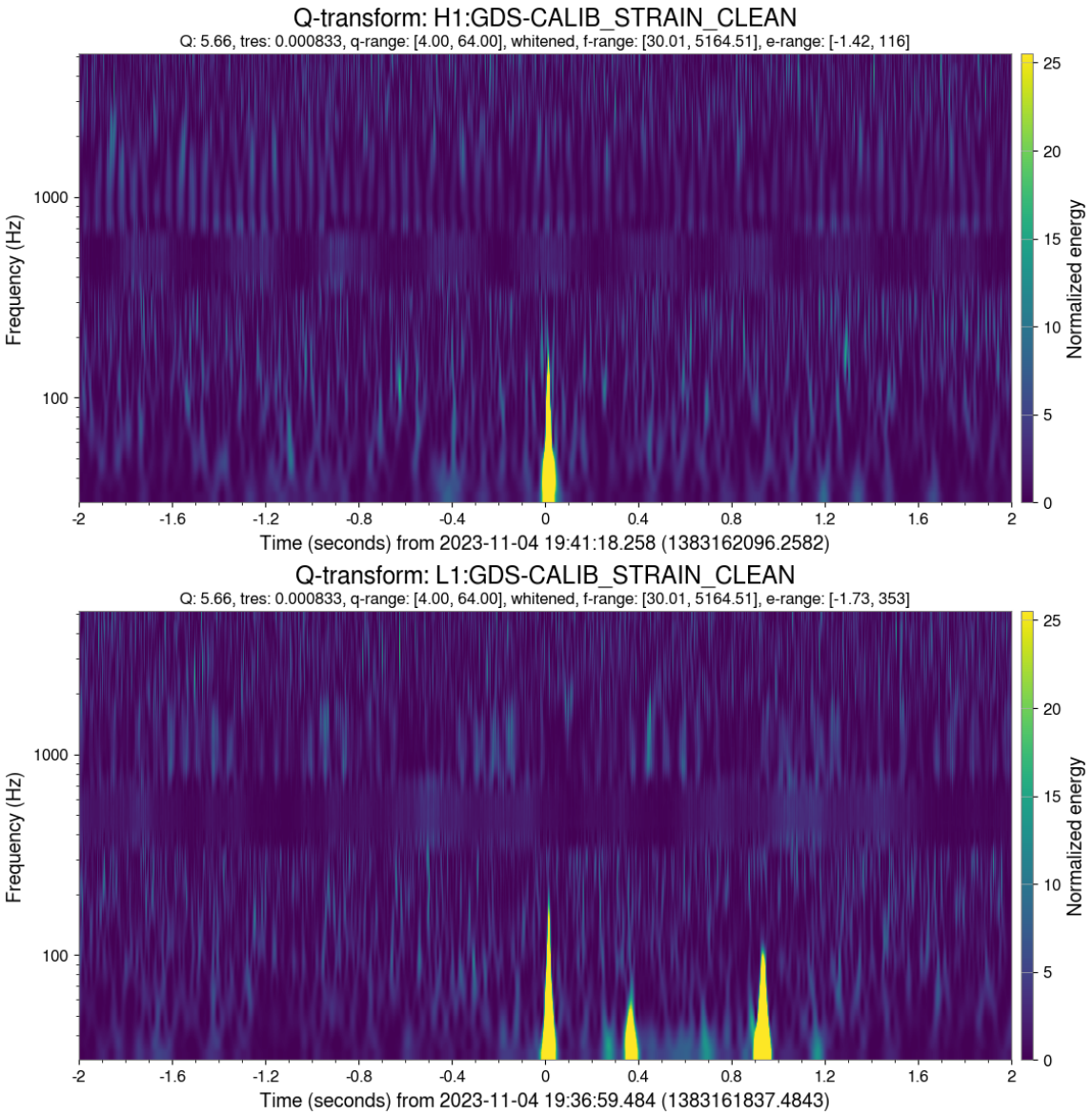


Figure 46. Comparison of LHO (top) and LLO (bottom) strain data near the highest-ranked background event found by the CS search. The large discrepancy in central time is due to the fact that LLO data has been timeslid by 73×3.54 s to produce the noise-only background data set.

population models. The rate R of GWs we expect to see in an amplitude interval is [212]

$$\frac{dR}{dA} = \frac{3}{4H_0^3}\int_0^\infty dz \frac{\varphi_{\rm V}(z)}{1+z}\frac{n(\ell(A,\ z),\ z)}{A}\frac{\Theta(1-(g_2(1+z)\ell\times 30\text{ Hz})^{-1/3})}{(g_2(1+z)\ell\times 30\text{ Hz})^{2/3}}. \tag{5.8}$$

This expression states that the burst rate depends on the proper volume that the search is sensitive to, the number density of loops $n(\ell,\ z)$ as a function of the invariant loop length $ell(A,\ z)$ and redshift z and is suppressed by cosmological expansion and the extreme geometric beaming of high-frequency GWs from CSs. Here H_0 is Hubble's constant, $\varphi_{\rm V}(z)$ is one of the so-called "interpolating functions" used in [102–104, 212], g_2 is a numerical factor of $\mathcal{O}(1)$ but whose exact values depends on assumptions made about the fraction of the string length is occupied by cusps and kinks. Following [221], [106] assumes a value of $\sqrt{3}/4$ for g_2, positing that cusps and kinks are small compared to the total CS loop arc length. The factor of 30 Hz arises from the search settings of section 5.1.2.3 - it is the lowest value of f_h that the CS search algorithm can confidently detect.

Given a prescription for the loop number density, one can compute the number of cusps per unit spacetime volume which produce GWs with amplitudes in the range $[A,\ A+dA]$. Given the configuration choices for the search, one can determine what fraction of these events should be observable due to geometric concerns. Once $\frac{dR}{dA}$ is found, the rate of detectable GW bursts from CSs is [106]

$$R = \int_{2\times10^{-22}\ \text{s}^{-1/3}}^{3\times10^{-19}\ \text{s}^{-1/3}} dA\frac{dR}{dA}\varepsilon(A). \tag{5.9}$$

Where $\varepsilon(A)$ is the O4a detection efficiency curve shown in figure 45 and the limits of integration set by the smallest and largest amplitude GW injections performed as part of the search pipeline.

5.2.2.2 Loop Distribution Models The number of CS loops and the size of those loops are difficult quantities to study. CSs are thin compared to their length, with thicknesses $\mathcal{O}(\sqrt{\mu})$ [92]. At these small length scales, effects such as gravitational backreaction affect the appearance and evolution of cusps and kinks [222, 223]. But in order to study the behavior and evolution of a network of CSs, like that expected to be formed in the early universe, large volumes of spacetime must be simulated. There is considerable difficulty reconciling simulation results from small- and large-length scale simulations [224]. This simulation problem is compounded by any additional string physics simulators want to impose on the string network, e.g. adding currents to be carried by the strings, modifying their interactions with one another and changing the scaling behavior of the network [225].

An additional difficulty in understanding the CS cusp burst rate is the number of kinks that reside on a CS loop. Kinks arise from the collision of two segments of CS. Their length is diminished via gravitational backreaction with nearby string segments as well as energy loss via GW emission. The presence of many kinks on a CS loop suppresses cusp formation [226].

Despite these significant challenges in understanding the population of GW emitters, three loop distribution models are considered at varying values of $G\mu$ and N_k, the number of kinks which travel along the CS loops. The first model has loop number density given by the sum of [106, 227]:

$$\left.\frac{d^2N}{d\ell dV}\right|_{\rm rad} = \frac{1}{t^4}\begin{cases} \frac{0.08}{(\gamma+\Gamma G\mu)^{3-2\chi_{\rm rad}}} & \text{if } \Gamma G\mu < \gamma \\ \frac{0.04-0.16\chi_{\rm rad}}{(2-2\chi_{\rm rad})\Gamma G\mu\gamma^{2-2\chi_{\rm rad}}} & \text{if } \gamma_c < \gamma < \Gamma G\mu \\ \frac{0.04-0.16\chi_{\rm rad}}{(2-2\chi_{\rm rad})\Gamma G\mu\gamma_c^{2-2\chi_{\rm rad}}} & \text{if } \gamma < \gamma_c \end{cases} \tag{5.10}$$

from loops formed in the radiation-dominant era of the universe,

$$\left.\frac{d^2N}{d\ell dV}\right|_{\rm mat} = \frac{1}{t^4}\begin{cases} \frac{0.015}{(\gamma+\Gamma G\mu)^{3-2\chi_{\rm mat}}} & \text{if } \Gamma G\mu < \gamma \\ \frac{0.015(1-2\chi_{\rm mat})}{(2-2\chi_{\rm mat})\Gamma G\mu\gamma^{2-2\chi_{\rm mat}}} & \text{if } \gamma_c < \gamma < \Gamma G\mu \\ \frac{0.015(1-2\chi_{\rm mat})}{(2-2\chi_{\rm mat})\Gamma G\mu\gamma_c^{2-2\chi_{\rm mat}}} & \text{if } \gamma < \gamma_c \end{cases} \tag{5.11}$$

for loops formed in the matter-dominated era of the universe, and

$$\left.\frac{d^2N}{d\ell dV}\right|_{\rm rad-mat} = \frac{\gamma t + \Gamma G\mu(t-t_{\rm eq})}{t} Big(\frac{1+z}{1+z_{\rm eq}}\Big)^3 \left(\left.\frac{d^2N}{d\ell dV}\right|_{\rm rad}\right)^3 \tag{5.12}$$

for loops which were formed in the radiation-dominant era but gravitationally decay during the matter-dominant era. Here γ is the dimensionless loop size ℓ/t, Γ is a decay constant which encodes how much power is gravitationally radiated away from a CS loop via oscillations of the loop for a particular string tension [228]. In the following, Γ =50 is adopted based off previous numerical simulations of CS networks [229]. γ_c is the dimensionless gravitational backreaction scale below which loop production is suppressed. It takes the value $20G\mu^{1+2\chi_{\rm rad/mat}}$. $\chi_{\rm rad/mat}$ is the *Polchinski-Rocha exponent* which characterizes the mean root-mean-squared sting velocity in radiation or matter dominated regimes [230, 231]. They also describe the fractal dimension of long strings. Here the Polchinski-Rocha exponents take the values $\chi_{\rm rad} = 0.45$, $\chi_{\rm mat} = 0.295$.

This model, informed by the simulation results of [232], describes CS loops as being formed at all length scales subject to a power law. The slope of this loop production function changes depending on radiation- or matter-dominance and it is truncated at low loop sizes.

The second and third models interpolate between the above loop distribution hypothesis and a second hypothesis for the loop distribution depending on the time of loop production. This is accomplished by summing the radiation-era

loop distribution function [106, 231]

$$\left.\frac{d^2N}{d\ell dV}\right|_{\rm rad} = \frac{1}{t^4}\frac{2c_{\rm rad}}{1-4\chi_{\rm rad}}\begin{cases}(\gamma+\Gamma G\mu)^{2\chi_{\rm rad}-3} - \frac{\gamma_\infty^{2\chi_{\rm rad}-1/2}}{(\gamma+\Gamma G\mu)^{5/2}} & \text{if } \Gamma G\mu < \gamma \\ \frac{\gamma^{2\chi_{\rm rad}-2}}{(2-2\chi_{\rm rad})\Gamma G\mu}\frac{\gamma_\infty^{2\chi_{\rm rad}-1/2}}{(\gamma+\Gamma G\mu)^{5/2}} & \text{if } \gamma_c < \gamma < \Gamma G\mu \\ (\gamma_c+\Gamma G\mu)^{2\chi_{\rm rad}-3} - \frac{\gamma_\infty^{2\chi_{\rm rad}-1/2}}{(\gamma+\Gamma G\mu)^{5/2}} & \text{if } \Gamma G\mu < \gamma \\ \frac{\gamma^{2\chi_{\rm rad}-2}}{(2-2\chi_{\rm rad})\Gamma G\mu}\frac{\gamma_\infty^{2\chi_{\rm rad}-1/2}}{(\gamma+\Gamma G\mu)^{5/2}} & \text{if } \gamma < \gamma_c\end{cases} \tag{5.13}$$

and the matter era loop distribution

$$\left.\frac{d^2N}{d\ell dV}\right|_{\rm mat} = \frac{1}{t^4}\frac{2c_{\rm mat}}{1-4\chi_{\rm mat}}\begin{cases}(\gamma+\Gamma G\mu)^{2\chi_{\rm mat}-3} - \frac{\gamma_\infty^{2\chi_{\rm mat}-1/2}}{(\gamma+\Gamma G\mu)^{5/2}} & \text{if } \Gamma G\mu < \gamma \\ \frac{\gamma^{2\chi_{\rm mat}-2}}{(2-2\chi_{\rm mat})\Gamma G\mu}\frac{\gamma_\infty^{2\chi_{\rm mat}-1/2}}{(\gamma+\Gamma G\mu)^{5/2}} & \text{if } \gamma_c < \gamma < \Gamma G\mu \\ (\gamma_c+\Gamma G\mu)^{2\chi_{\rm mat}-3} - \frac{\gamma_\infty^{2\chi_{\rm mat}-1/2}}{(\gamma+\Gamma G\mu)^{5/2}} & \text{if } \Gamma G\mu < \gamma \\ \frac{\gamma^{2\chi_{\rm mat}-2}}{(2-2\chi_{\rm mat})\Gamma G\mu}\frac{\gamma_\infty^{2\chi_{\rm mat}-1/2}}{(\gamma+\Gamma G\mu)^{5/2}} & \text{if } \gamma < \gamma_c\end{cases} \tag{5.14}$$

where γ_∞ is the dimensionless size of the largest loops considered. $c_{\rm rad/mat}$ are normalizing constants used to fit the distributions to numerical results from simulations.

The second model tested draws its radiation-dominant era loop distribution function directly from a population of loops extracted from a simulation [233]. For loops formed in the matter-dominated era, equation 5.11 is used. The third model is the converse of the second model: equation 5.10 describes the loop distribution from loops formed in the radiation-dominant era and simulation results are used to determine the contribution to the total loop distribution from CS loops formed during the matter-dominant era. Compared to the first model, these models directly incorporating simulation results feature fewer small loops being formed [106]. Varying the normalizing constants and Polchinski-Rocha exponents between these two models allows for the radiation and matter-dominant era loop distributions from multiple sources to be combined.

Table 4. Naming conventions used for CS loop population models.

Work	Model names		
[106]	B	C-1	C-2
This dissertation	RSB	ARMS-RSB-mat	ARMS-RSB-rad

In the following, I refer to the first model described here as the "RSB" model, the second model tested as "ARMS-RSB-mat," and the final model as "ARMS-RSB-rad." This is different from the nomenclature used in [106]. Table 4 lists the model names in the style of the O3 LIGO-Virgo-KAGRA and this work.

5.2.2.3 Cosmic String Population Constraints from the O4a Search

The objective of the loop distribution models is to produce predictions for the number of observable CS GW bursts. From Poisson statistics, if the number of GW bursts observed during an observing run of duration T is zero, then theories predicting observable bursts which occur at $R > \frac{2.996}{T}$ can be ruled out at the 95% credible level. It is therefore possible to make statements about Beyond the Standard Model physics by evaluating the each model's observable burst production rate at various values of string tension and identifying which values of $G\mu$ produce burst rates which can be confidently excluded by LIGO search data.

Figure 47 shows the consequences of a non-observation for the LRM model in the case of O4a. Figure 48 shows the same result for model ARMS-LRM-mat and figure 49 shows values of $G\mu$ excluded should the CS population follow the ARMS-RSB-rad model. Each of these rate upper limits assume that the number of cusps on a given string loop is one and the number of kinks per loop, N_k, is zero.

For all three models, O4a data sets ∼22% more stringent upper limits on string tension compared to O3. The upper limits on possible string tensions excluded for each model are shown in table 5. The increased stringency of these new upper limits is in spite of the fact that O3's duration was about twice as long

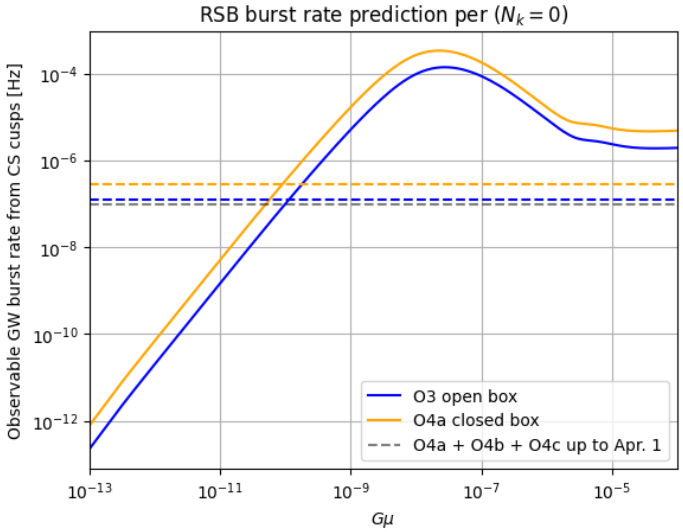


Figure 47. Allowed and excluded values of the string tension in the RSB model due to their non-observation in O3 and assuming a non-observation in the unblinded O4a search data. The dashed horizontal lines denote $1/T$ for each of the three observing run scenarios.

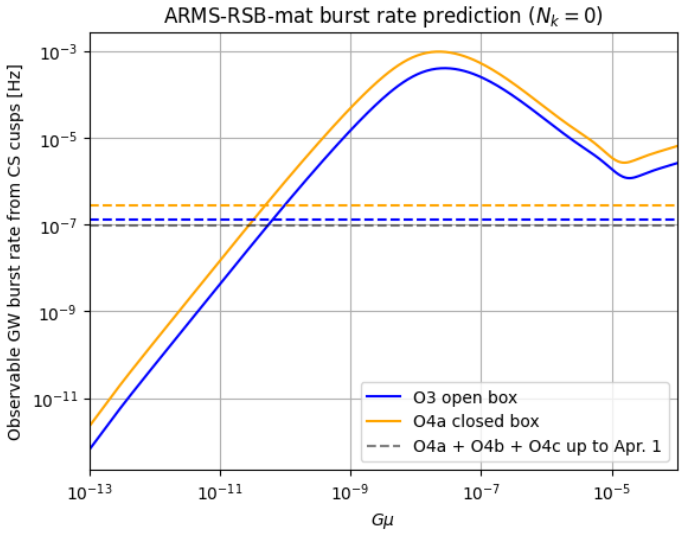


Figure 48. Allowed and excluded values of the string tension in the ARMS-RSB-mat model due to their non-observation in O3 and assuming a non-observation in the unblinded O4a search data.

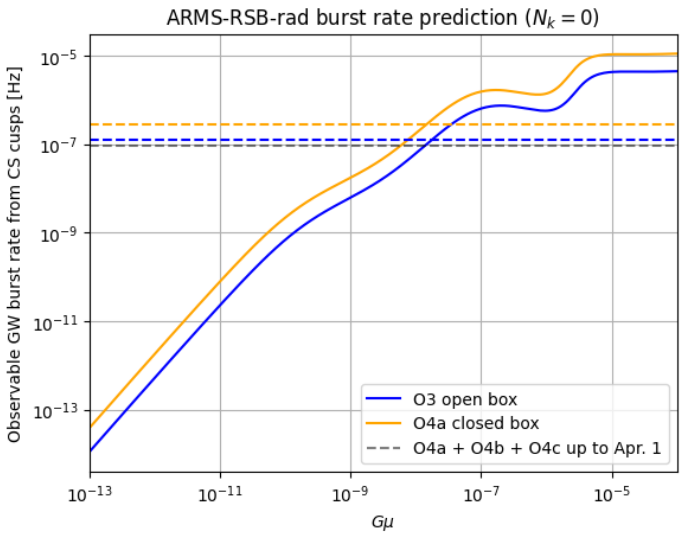


Figure 49. Allowed and excluded values of the string tension in the ARMS-RSB-rad model due to their non-observation in O3 and assuming a non-observation in the unblinded O4a search data.

as O4a. Despite the shorter observing time considered in the O4a cusp search, the improved sensitivity of the detectors, as illustrated in figure 2, means that the rate of observable bursts for a given $G\mu$ is higher in O4a compared to O3. Figures 47, 48, and 49 also show a forecast for what string tensions can be excluded based on the added duration of high-quality observing mode data from O4b and O4c up to April 1, 2025 in the event of a non-detection. LIGO plans to conclude O4c on November 18, 2025 [234]. The addition of Virgo data in O4b onward improved the 2+ interferometer duty factor by ∼13% through April 1, 2025. The forecast for improved upper limits is only valid as long as the injection efficiency curve does not meaningfully change from its O4a behavior shown in figure 45.

Even though no search for CS kinks is carried out directly in this work, the relative absence or presence of kinks should increase or decrease the amount of GW power radiated via cusps, respectively. The results in figures 47- 49 and table 5 are presented under the assumption of zero kinks per CS loops. By introducing kink

Table 5. Upper limit on CS tension for each model set by non-observation. The final column represents a forecast at the upper limit set assuming a non-observation through April 1, 2025. Discussion of the O3 results is found in [106].

Model	O3	O4a	O4a-c until April 1, 2025
RSB	$G\mu < 1.18 \times 10^{-10}$	$< 9.20 \times 10^{-11}$	$< 4.73 \times 10^{-11}$
ARMS-RSB-mat	$G\mu < 6.60 \times 10^{-11}$	$< 5.14 \times 10^{-11}$	$< 2.87 \times 10^{-11}$
ARMS-RSB-rad	$G\mu < 1.74 \times 10^{-8}$	$< 1.36 \times 10^{-8}$	$< 5.90 \times 10^{-9}$

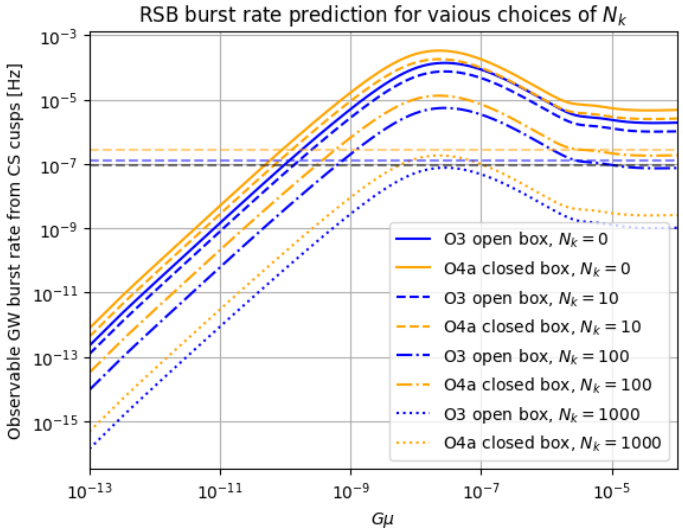


Figure 50. Upper limit on $G\mu$ for past and current CS cusp searches for a variety of N_k per CS loop in the RSB model, assuming a non-detection in the O4a search data.

populations to the loops, the rate of observable GW bursts should decline, as more energy is radiated away via the kink and kink-kink collision modalities. Figures 50 and 51 show the effect of introducing kinks on the observable burst rate and table 6 records the upper limit on $G\mu$ inferred from the data.

The preceding discussion is founded on no detection in the O4a data. The following chapter discusses strategies that may be employed in the case of a detection in the O4a or complete O4 data sets.

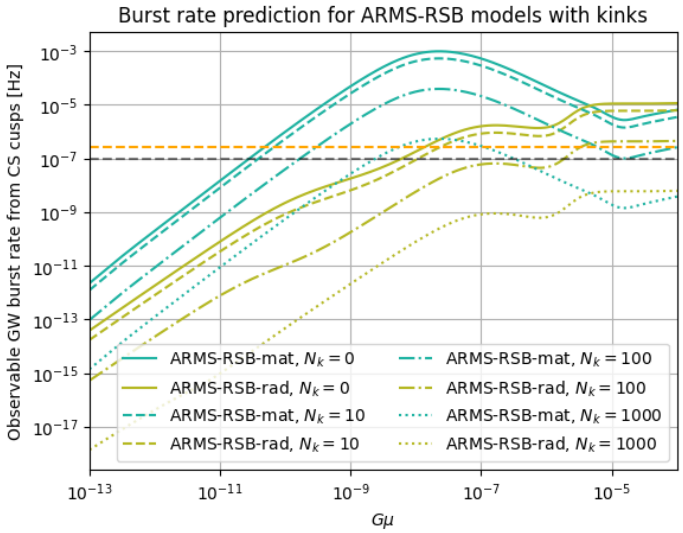


Figure 51. Observable O4a burst rate for the ARMS-RSB-mat and ARMS-RAD-rad models for different N_ks. The orange dashed line denotes $1/T$ for O4a and the grey dashed line denotes $1/T$ for O4 through April 1, 2025.

Table 6. Limits on the CS tension inferred from O4a for several choices for N_k. Because the rate as a function of the tension is non-monotonic, large string tensions are not excluded for 100 kinks per loop for two of the three models. The observable burst rate for loops with 1,000 kinks is too low to set a limit on the string tension in the analysis framework used in this work. These figures assume no detection in the unblinded O4a data set. Burst rates were calculated for $G\mu \in [10^{-13},\ 10^{-4}]$.

N_k	$G\mu$ exclusion		
	RSB	ARMS-RSB-mat	ARMS-RSB-rad
0	$G\mu < 9.20 \times 10^{-11}$	$G\mu < 5.14 \times 10^{-11}$	$G\mu < 1.36 \times 10^{-8}$
10	$G\mu < 1.28 \times 10^{-10}$	$G\mu < 7.17 \times 10^{-11}$	$G\mu < 2.64 \times 10^{-8}$
100	$G\mu \notin (5.74 \times 10^{-10},\ 3.89 \times 10^{-6})$	$G\mu \notin (2.95 \times 10^{-10},\ 5.90 \times 10^{-6})$	$G\mu < 3.58 \times 10^{-6}$
1,000	—	$G\mu \notin (5.90 \times 10^{-9},\ 1.09 \times 10^{-7})$	—

CHAPTER VI

PARAMETER ESTIMATION FOR GRAVITATIONAL WAVES FROM COSMIC STRINGS

> *"This is an all-or-nothing proposition, ain't it? If we make a find, we'll be lightin' our cigars with hundred dollar bills. If we don't, the difference between what you put up and what I put up ain't enough to keep me from being right back where I was this afternoon, polishing a bench with the seat of my pants."*
>
> —Fred Dobbs, *The Treasure of the Sierra Madre* [235]

The PE routine developed and characterized here was developed by me. Daichi Tsuna contributed helpful suggestions regarding parameter ranges and waveform systematics to test. I led the study design, analysis and writing of this unpublished work. Daichi Tsuna provided helpful suggestions to the text. Raymond Frey is the principal investigator for this work.

6.1 Introduction

CSs are one-dimensional topological defects which are generic predictions of classes of unified theories which feature one or spontaneous symmetry breaking phase transitions that reduce to the Standard Model of particle physics in the low-energy limit [91]. CSs are characterized by their tension, $G\mu$ in units of speed of light $c = 1$, with G being Newton's gravitational constant and μ the mass per unit length. A string's tension is proportional to the square of the energy scale of the spontaneous symmetry breaking [92]. Astrophysical searches for CSs provide a probe of physics at much higher energies than what can be tested in terrestrial particle colliders.

Numerous phenomena resulting from a network of CSs formed in the early Universe have been suggested as probes for the existence and properties of CSs.

Examples of these phenomena include double images of faraway objects due to gravitational lensing by a CS [236, 237], discontinuities in measurements of the temperature of the cosmic microwave background [238, 239], high-energy cosmic ray production [240], measurable contributions to the mass function of galactic dark matter halos [241] and more.

In addition to possible electromagnetic observations, loops of CSs emit collimated bursts of radiation in the form of GWs from cusps, points along the string which move at the speed of light [102, 242], kinks, deformations of the string from inter-commutation with other CSs which propagate along the string's length [103, 243]. In addition, kink-kink collisions along a string are expected to isotropically emit GWs [244].

Searches for GW transients ("bursts") from these CS features as well as the superpositions of GWs from CSs to the stochastic GW background have been conducted [106–109, 245]. Their non-observation have set stringent bounds on allowed values for $G\mu$ and therefore on the energy scale(s) of spontaneous symmetry breaking in the early Universe.

Despite their continued non-observation, searches for GWs from CSs represent a promising opportunity to explore high-energy, beyond the Standard Model physics and refine our understanding of CS-CS interactions. Ongoing searches for GW bursts from CSs using data from the LIGO detectors represent a possible means to detect these signals. Given the success of PE methods in understanding the population properties of compact object mergers observed by the LIGO detectors, in conjunction with the Advanced Virgo [25] and KAGRA [26] GW observatories (e.g. [61, 62]), we extend extant GW PE methods to bursts of GWs from CSs.

In this work, we study the extent to which CS parameters can be accurately reconstructed for GW bursts seen by the LIGO detectors in their O3 sensitivity. Using these results, including results from PE routines run on O3 noise artifacts which limit the current CS burst search [106], we outline the conditions needed for successful PE in future realizations of terrestrial GW observatories, including LIGO operating at its projected fifth observing run (O5) sensitivity [27]. Should PE routines like the method described herein be applied to potential CS signals in coming observing campaigns, we stand to learn a great deal about string dynamics. This work represents the first systematic study of the feasibility of PE using GW bursts from cusps and kinks along CSs.

6.2 Methods

6.2.1 CS Gravitational Waveforms GW bursts from CSs are sourced from cusps, kinks, and collisions of kinks. They are known to have simple forms in the frequency domain as power laws in frequency [103, 244], where the power law index q depends on the GW source – $q = 4/3,\ 5/3,\ 2$ for cusps, kinks, and kink-kink collisions, respectively. For cusps (kinks), GW emission is restricted to a narrow cone (fan) in certain directions [103], while in kink-kink collisions, the resulting GW emission is isotropic [244]. This geometric consideration imposes a cutoff frequency $f_{\rm high}$ on cusp and kink signals dependent on the viewing angle, above which the GW emission is exponentially suppressed.

The lowest frequency where GW emission occurs is dictated by the size of the emitting feature. However, the practical lower limit of the observed signal is set by the low-frequency sensitivity of GW observatories, which in turn is dictated by the position of the so-called "seismic wall." In this work, we suppress contributions to the CS signal below 10 Hz.

Combining the high and low frequency cutoffs and the general behavior of the waveform described above, we arrive at the frequency-domain waveform injected in this study, similar to the CS waveform used by LALSuite [217]:

$$\tilde{h}(f) = Af^{-q}\left(1 + \left(\frac{10\text{ Hz}}{f}\right)^2\right)^{-4} \times \begin{cases} e^{1-f/f_{\text{high}}} & f > f_{\text{high}} \text{ and } q \neq 2 \\ 1 & f \leq f_{\text{high}} \text{ or } q = 2 \end{cases}. \quad (6.1)$$

Here A is the GW amplitude and has units of s^{q-1}.

Following this prescription, completely plus-polarized GWs were injected into realistic interferometer noise. Injections were made into noise drawn from LIGO O3 sensitivity curves and proposed A+ sensitivity curves. The noise spectra used for data generation are shown in figure 52. The GWs were injected from a variety of sky locations to account for variations in detector sensitivity as a result of each detector's antenna pattern. The injected waveforms also include a phase term, but this is marginalized over.

6.2.2 Frequency-domain Inference Using injected GWs made with the custom GW waveform of equation 6.1, frequency-domain PE is performed with Bilby [246]. For each injected combination of GW $\mathcal{A}$, f_{high}, and q, two attempts at frequency-domain inference are made: one where Bilby attempts to infer the parameters of the injected signal with q known and one where q is a free parameter to be inferred. The former scenario could correspond to a CS trigger found with high likelihood [213] by only one instance of the cosmic string search pipeline, which performs three independent searches for bursts of GWs from cusps, kinks, and kink-kink collisions [106], while the latter could be applicable where a string

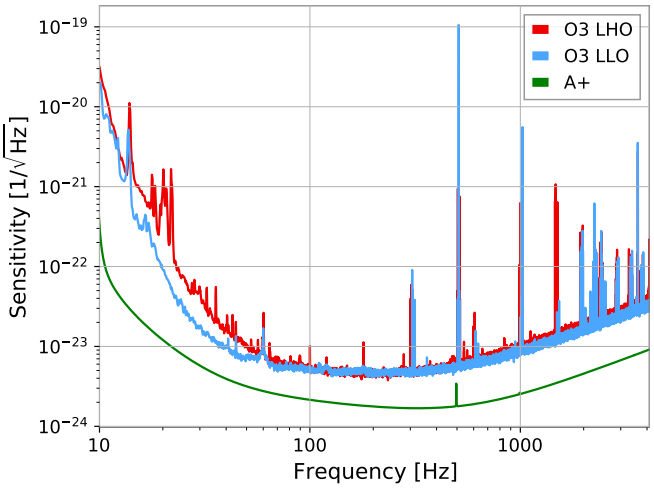


Figure 52. Amplitude spectral densities used to generate realistic detector noise for this chapter. The O3 traces correspond to already realized detector sensitivities, while the A+ curve represents a hypothetical noise budget for these facilities in the future.

candidate is identified by multiple searches. Further discussion of discriminating between signal modalities is found in section 6.4.2.

For both methods, nested sampling using Bilby's implementation of Dynesty [247] was employed to perform PE using the custom waveform of equation 6.1.

6.3 Results

6.3.1 O3 Results We performed more than 25,000 injections into noise generated from cleaned, 60-Hz subtracted, O3 LIGO sensitivity curves representing detector performance in the second half of the third observing run [248–250]. One quarter of these injections were made with the intention of treating the emission modality, represented by the power law index q, as a free parameter to infer. Table 7 describes the ranges over which injected parameters varied. Table 8 shows the prior distributions on the parameters used to conduct the nested sampling.

Parameter	Range
A [s^{q-1}]	10^{-22}–10^{-19}
Power law index q	4/3, 5/3, 2
$f_{\rm high}$ [Hz]	16–1024
Right ascension [rad]	0–$\frac{12\pi}{7}$
Declination [rad]	$-\frac{\pi}{2}$–$\frac{\pi}{2}$
GW polarization [rad]	Completely +

Table 7. Parameter combinations for the waveforms injected into O3 noise. When the power law index was set to 2, representing a kink-kink collision, $f_{\rm high}$ was not used to compute the waveform.

Parameter	Prior distribution
t_c	$\mathcal{U}[-1, 1]$ s
$\log_{10} A$	$\mathcal{U}[-25, -17]$
$\log_2 f_{\rm high}$	$\mathcal{U}[4, 13]$
α	$\mathcal{U}[0, 2\pi)$ rad
δ	$\mathcal{U}[-\frac{\pi}{2}, \frac{\pi}{2}]$ rad
ϕ	$\mathcal{U}[0, 2\pi)$ rad
ψ	$\mathcal{U}[0, \pi)$ rad
q	$\mathcal{U}[\frac{4}{3}, 2]$

Table 8. Prior choices for the O3 injections. The upper bound on the amplitude prior was chosen by identifying at what amplitude a CS signal would be detected with near certainty by the search pipeline described in [106]. For kink-kink injections where q is sampled over (and thus a high frequency cutoff is allowed), the expectation for the posterior distribution on $f_{\rm high}$ is to recover the prior distribution on the high frequency cutoff.

Because CS signals are poorly constrained due to their continued non-observation, broad prior choices were used.

In general, PE is possible for CS signals due to their simplicity with a small number of parameters. Depending on the SNR of the injected signal in the detectors, accurate recovery of injected parameters can be achieved. This is illustrated in figure 53. In this example, injections were made into O3-style noise. At the GW amplitude chosen for these injections, the dedicated O3 CS search

pipeline found 95% of cusp signals, 81% of kink signals and 37% of kink-kink signals added to timeslid data as part of its search process [106, 213].

Even with the poor recovery of kink-kinks at this amplitude, the kink-kink PE accurately recovers the injected amplitude within the 90% credible interval, as shown in the left pane of figure 53c. Accurate amplitude recovery is critical to understanding the underlying symmetry that produced the CSs. The amplitude of a CS GW burst is given by equation 2.70 [106]. Accurately recovering the amplitude, with the estimated event rate from a detection, can constrain the tension of the CS $G\mu$ given a theoretical model for the spatial distribution of the string loops (and vice versa). Observation and proper amplitude estimation of GWs from a CS, in conjunction with models for the string loop size distribution and CS number density could reveal evidence for beyond the Standard Model physics which are hidden at ordinary energy scales.

As figure 53 and the related discussion shows, whether the assumed waveform is modality-specific or generic affects the performance of this PE method at accurately reconstructing waveform parameters. We now consider the scenario that a CS is detected by multiple instances of the extant pipeline with good significance and determine under what conditions we can confidently infer the emission modality.

We employ two statistics calculated for each injection: the combined optimal SNR of each injected GW as calculated by Bilby

$$\rho = \sqrt{|\rho_{\mathrm{LHO,\ opt}}|^2 + |\rho_{\mathrm{LLO,\ opt}}|^2} \tag{6.2}$$

and, once the sampling is complete, the logarithm of the signal versus noise Bayes factor $\mathcal{B}^{\mathrm{signal}}_{\mathrm{noise}}$ [251]. The relation between these two quantities is shown in figure 54. The latter is especially useful in comparing the outcomes of different PE runs

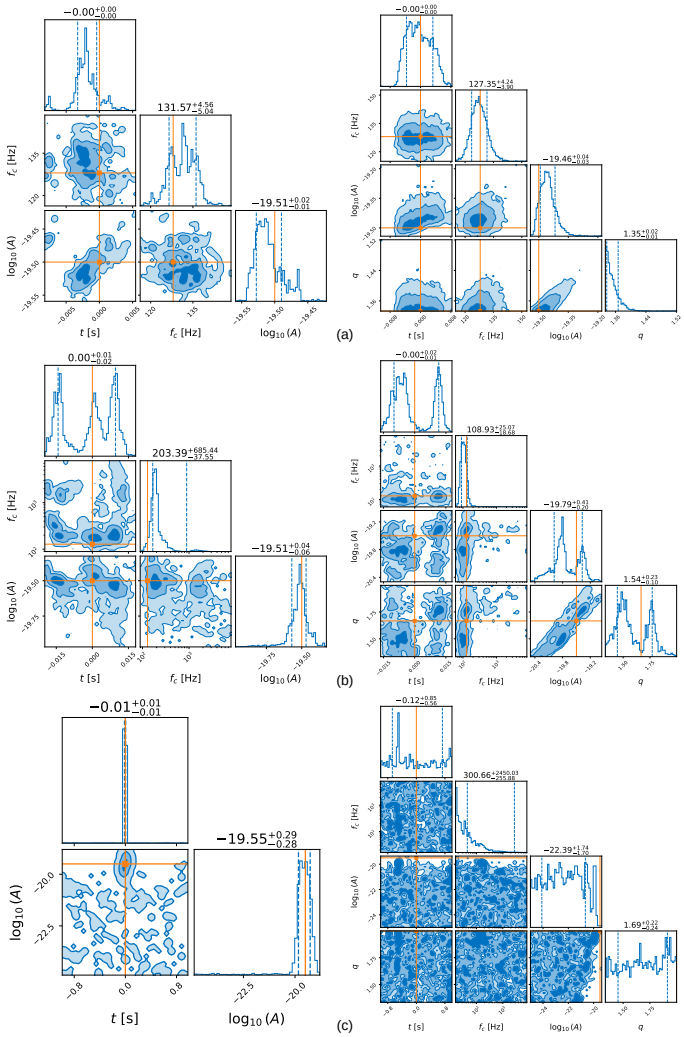


Figure 53. Performance of the PE method described herein on a (a) cusp, (b) kink, (c) kink-kink collision signal. Each injection was made in O3-style noise at GPS time of 0 s with an amplitude of $A = 10^{-19.5}\ \mathrm{s}^{1-q}$, with $f_{\mathrm{high}} = 128$ Hz for the cusp and kink injections. The SNR of the three injections were ~ 61, 6 and 4, respectively. The corner plots on the left for each modality show the performance of PE when q is fixed to be the true value of the power-law index, while the right-hand column shows the results when the power law index is left as a free parameter. Orange bars on the 1- and 2-D histograms identify the true values of the injected parameters and the dashed lines indicate the extent of the 90% credible interval for each inferred parameter. For the modality-independent injection where the true signal was a kink-kink, the PE is uninformative, essentially returning the prior distributions on the parameters.

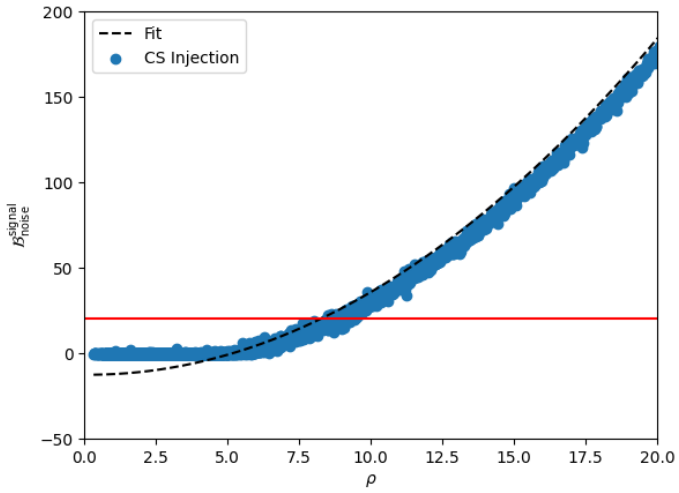


Figure 54. Comparison between the logarithm of the signal versus noise Bayes factor and SNR of the injected dataset. The recovered waveform Bayes factor is fit well by a curve proportional to ρ^2 at $\rho \gtrsim 5$, as expected in the limit of high SNR [147, 254]. A detection of a CS would likely require extraordinary confidence in its PE. The red horizontal line denotes $\mathcal{B}^{\text{signal}}_{\text{noise}} = 20$, which is surpassed by the fit at $\rho \approx 8.25$.

on the same injected waveform, as each individual run's $\mathcal{B}^{\text{signal}}_{\text{noise}}$ can be combined to determine—as an example $\mathcal{B}^{\text{kink}}_{\text{cusp}}$—for the purposes of model selection. This is similar to the model selection approach used in [252] which found substantial evidence disfavoring a CS origin for GW190521 [58], a GW event observed by both LIGO detectors as well as the Virgo detector. A more recent analysis which compared the CS signals studied here, equation 6.1, to GWs emitted as a CS loop collapses to a black hole showed that the data is more consistent with this latter scenario, though the compact binary coalescence scenario is still strongly preferred overall [253].

We use the $\mathcal{B} - \rho$ relation in figure 54 to focus on the most salient subset of injected CS signals: those with a high enough SNR to feasibly be detected but with a low enough SNR that their origin may be ambiguous until PE is performed, i.e. $\rho \approx 8$–10 CS signals.

6.3.2 A+ Results

Improved sensitivity to CS signals is best accomplished by improving detector sensitivity at low frequencies due to the power-law nature of the GW waveform. Below ∼30 Hz, the LIGO detectors in their A+ configuration are expected to be more than 10 times more sensitive to GWs compared to their configurations in O3, as shown in figure 52.

To determine the increased ability to resolve CS GW parameters afforded by this expected increase in sensitivity, we inject over 4,700 CS signals into simulated data.

6.4 Discussion

6.4.1 CS Signal Type Sensitivity

One limitation of the current CS search conducted by the LIGO-Virgo-KAGRA Collaboration is that it is possible that a candidate GW time is identified by two or more of the independent searches for GW bursts from cusps, GW bursts from kinks, and GW bursts from kink-kink collisions. PE provides a method to distinguish between CS source types. Correct identification of the GW emission modality for the case of a single observation would begin to inform estimates of the number of cusps or kinks per CS loop [106, 244]. Kinks arise from CS collisions and their population is modulated by the strength of gravitational backreaction of the string. If backreaction is strong enough, simulations suggest that the kink population will diminish and cusps will form more readily on the CS [244, 255, 256]. The first step in ascertaining the particulars of CS physics impact GW emission in the case of a detection will be to establish whether the source of the GW burst was from a cusp, kink, or kink-kink collision.

We evaluate the efficacy of the PE code to correctly infer the type of CS emission by injecting a moderate SNR cusp, kink and kink-kink signal into O3

		Bayes factor denominator				
		Noise	Cusp	Kink	Kink-kink	Generic
Bayes factor numerator	Cusp	$21.00^{+7.81}_{-6.29}$	–	$0.07^{+1.13}_{-0.85}$	$0.14^{+1.14}_{-0.67}$	$0.22^{+0.80}_{-1.11}$
	Kink	$22.30^{+6.96}_{-5.58}$	$-0.15^{+0.60}_{-0.41}$	–	$-0.02^{+0.78}_{-0.59}$	$-0.08^{+0.75}_{-0.68}$
	Kink-kink	$22.51^{+6.08}_{-5.87}$	$0.02^{+0.68}_{-0.70}$	$0.06^{+0.56}_{-0.45}$	–	$0.07^{+0.56}_{-0.54}$

Table 9. The result of model selection for $8 \leq \rho \leq 10$ CS injections. Table entries indicate the median of the logarithm of the Bayes factor computed for each numerator-denominator pair. The numerator of the Bayes factor corresponds to the actual CS waveform type injected into mock data, i.e. the top right cell indicates the median $\mathcal{B}^{\text{cusp}}_{\text{generic}}$ computed for all moderate SNR cusps waveform injections. The values of the tenth and ninetieth percentiles for each $\mathcal{B}$ distribution are also indicated. These results were drawn from 142 cusp injections, 124 kink injections and 100 kink-kink injections.

noise and then trying to perform PE with the four waveforms at hand: the cusp, kink and kink-kink waveforms as well as the "generic" waveform with q treated as a free parameter. The Bayesian evidence for each signal model used in the PE can be compared to perform model selection for the preferred emission mechanism for injected GWs by computing $\mathcal{B}$, the logarithm of the Bayes factors for one signal model versus another, from the evidence [251]. The results of this procedure are shown in table 9.

6.4.2 Instrumental Artifacts Past searches for GW transients from CSs have been hindered by the presence of short-duration, large bandwidth instrumental artifacts of unknown origin which appear in both LHO and LLO data [106, 108, 109]. These artifacts—blip glitches [145]—occurred at the rate of about once per hour at each observatory in O3 [124] and frequently confuse the CS search pipeline, with a blip glitch at a single detector frequently being identified as a high-likelihood CS candidate in the search. Figure 55 illustrates how these blips resemble CS signals.

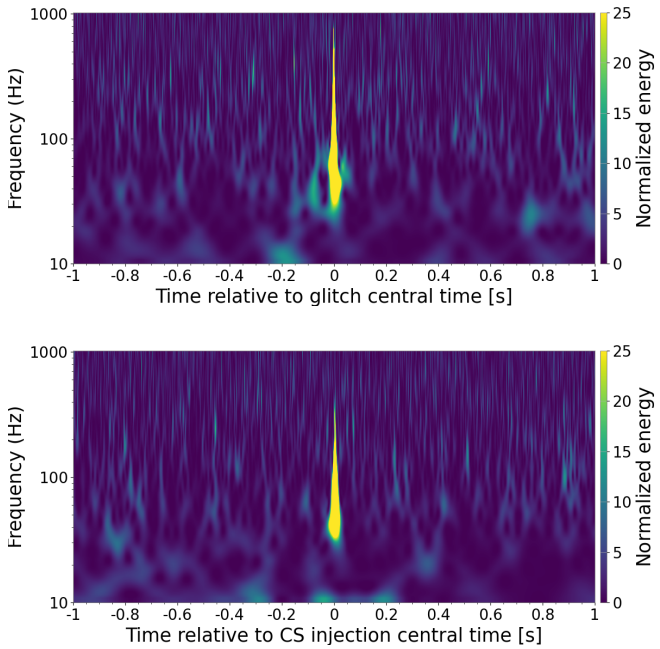


Figure 55. Q-transforms [191] of (top) a blip glitch, as identified by GravitySpy in O3 data from LLO and (bottom) a CS cusp waveform injected into noise drawn from the O3 LHO noise spectral density shown in figure 52. The injected signal was a cusp with amplitude 10^{-20} $s^{1/3}$ and a $f_{\rm high}$ of 256 Hz.

It is therefore important to check whether this CS PE method can provide any insight into distinguishing between blip glitches and reals CS signals. To do this, we performed PE with the modality-free waveform model on 58 blip glitches identified by GravitySpy [144] in O3 data, representing about 1% of blip glitches identified with 95% or greater confidence. These were randomly selected from the list of GravitySpy glitch candidates subject to the condition that the both LIGO detectors were operating, as the CS transient search requires data from two or more detector data streams to select CS candidates. Sometimes in this sample, blip glitches at one detector were coincident with non-stationary noise at the other LIGO observatory. Other times, the other observatory's data quality was good during the blip glitch. Figure 56 shows an example corner plot produced by the PE routine when run on data surround a blip glitch in one detector and coincident data with no apparent noise artifacts from the other LIGO detector. On the surface, this particular blip glitch matches the modality-independent signal model well, with a $\mathcal{B}^{\text{signal}}_{\text{noise}}$ of 261.507. However, the CS signal inferred is one that is most likely of kink-kink origin according to the posterior distribution of q. However, the posterior of f_{high} distributed narrowly around 16 Hz is in tension with the isotropic, high frequency cutoff independent, emission model for kink-kink collisions. PE results which disqualify blips due to contradictions in their inferred parameters could be use to supplement glitch removal methods, such as the "glitch surgery" approach suggested in [257], which attempt to remove short-duration, high-bandwidth noise transients from GW detector data, while preserving real GW signals.

Another approach that could be used to discriminate between blip glitches and CS candidates comes from studying the properties of many PE realizations on blips. Figure 57 shows that performing CS waveform PE on blips reveals two

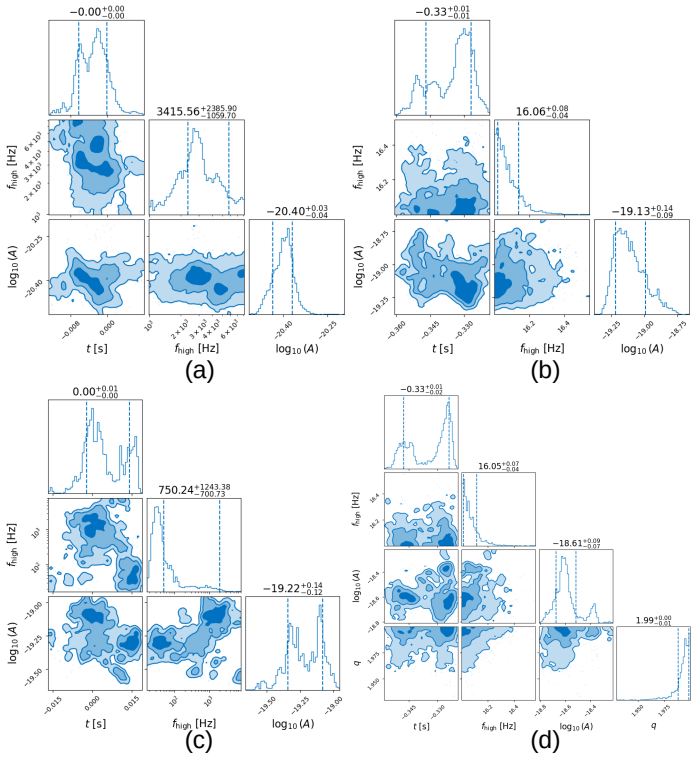


Figure 56. Results of PE around a blip glitch that occurred in O3. The inferred waveform type is (a) cusp, (b) kink, (c) kink-kink, and (d) generic. The inferred time of arrival is displayed in terms of the time difference relative to the central time of the blip as identified by GravitySpy. The preferred waveform modality by Bayes factor is the generic, followed by the cusp. The railing of the posterior of the modality distribution against $q = 2$ and the posterior of $f_{\rm high}$ being well-constrained to the neighborhood of 16 Hz are in tension with one another. This is am indication that the data analyzed does not contain a signal of astrophysical origin.

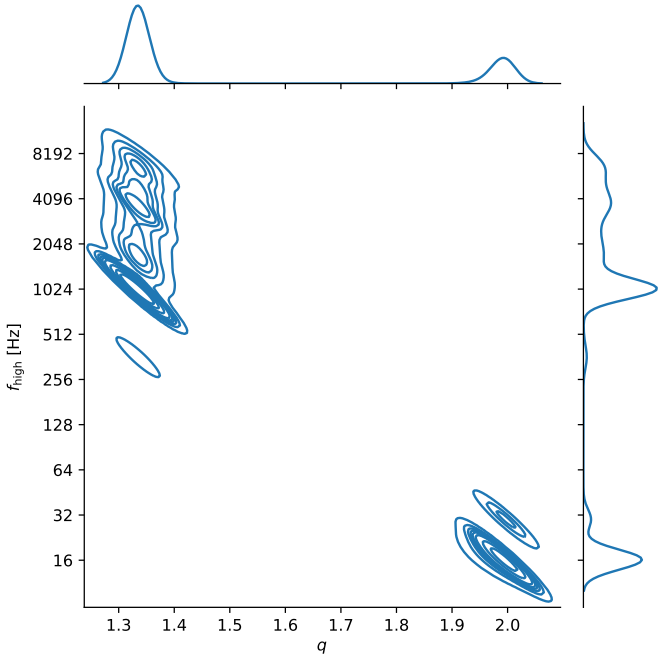


Figure 57. Kernel density estimate of inferred power law index and high frequency cutoff distributions for the 58 O3 blip glitches considered in this work. The PE method tends to classify blip glitches as kink-kink signals with a very low-frequency high frequency cutoff, which is not physical, or cusp signals with a high frequency cutoff in the kHz regime. Each parameter's marginal distributions are plotted around the two-dimensional distribution.

distinct populations in inferred $f_{\text{high}} - q$ space. Should this relation hold true for future glitch populations, an argument for or against the astrophysical origin of a CS candidate may be made by comparing the candidate's inferred properties against the distribution of glitch properties.

CHAPTER VII

CONCLUSION

> *So my story is told, except for the tacking on of a few not very important details I failed to cover elsewhere.*
>
> —Kurt Vonnegut, *Galápagos* [258]

The fields of GW astronomy and multi-messenger astrophysics are less than a decade old. In that decade, these fields have shifted from discovering "firsts" to inferring small features in the parameter distributions of the population of CBCs and studying the remnants of NSs seen by GW interferometers in the entire electromagnetic spectrum. The resulting discoveries have advanced our collective understanding of nuclear physics, stellar evolution, and perhaps our origin as a species [259].

This revolution in astronomy is only possible through the challenging process of commissioning and improving GW detectors and their instrumentation. The environmental noise investigations of chapter III highlight my contributions to this ongoing effort. To conduct detailed population studies of the universe's CBCs, a large number of GWs must be detected, and we must be very confident about the quality of detector data surrounding each GW event. Of course, the requirements of the former pose a challenge for the latter due to the limited amount of time in which data quality investigations can be conducted as more events are detected. Chapter IV traces the development and deployment of an automated data quality assessment tool I designed which reduces the effort required to verify GW candidate event data quality in O4.

Identification and mitigation of data quality issues improves LIGO's searches for GWs. One particularly compelling search is the search for GWs from CS.

Chapter V contains the first results of this search in O4 data which I conducted. The underlying mathematical framework of the CS search assumes a non-detection. Chapter VI shows the performance of PE tools I adapted from their ordinary CBC use on injected CS signals in GW data. The results of this study can be used to assess the highest-likelihood CS candidates in the search in chapter V and future searches.

The LIGO detectors are only able to detect the loudest GWs from the nearest sources. Future observatories, such as Cosmic Explorer will be capable of seeing nearly all BNS mergers and 30-30 $M_{\odot}$ BBH mergers that occur in the universe [195]. They will provide the most sensitive probe for as-of-yet unobserved GW sources like CSs. Proposed future terrestrial detectors like Cosmic Explorer or the Einstein Telescope will be limited in their sensitivity by the same sorts of noise sources which affect the LIGO detectors. The same noise monitoring and noise hunting techniques discussed in this work will be applicable for future proposed facilities too.

Bibliography

[1]F. Nietzsche, *Thus spoke Zarathustra*, trans. by C. Martin (Barnes & Noble Books, 2005).

[2]I. Newton, *Keynes MS. 28*, edited by W. R. Newman, (2010) `https://webapp1.dlib.indiana.edu/newton/mss/norm/ALCH00017/` (visited on 19/08/2024).

[3]I. Newton, *Mathematical principles of natural philosophy*, trans. by I. B. Cohen and A. Whitman (University of California Press, 1999).

[4]S. Navas et al. (Particle Data Group Collaboration), "Review of particle physics", Phys. Rev. D **110**, 030001 (2024).

[5]S. Hawking, "Newton's *Principia*", in *Three hundred years of gravitation*, edited by S. Hawking and W. Israel (Cambridge University Press, 1987), pp. 1–4.

[6]J. Renn, "Classical physics in disarray: the emergence of the riddle of gravitation", in *The genesis of general relativity*, Vol. 1, edited by J. Renn (Springer, 2007), pp. 21–80.

[7]C. Montgomery, W. Orchiston and I. Whittingham, "Michell, Laplace and the origin of the black hole concept", Journal of Astronomical History and Heritage **12**, 90–96 (2009).

[8]W. M. Smart, "John Couch Adams and the discovery of Neptune", Nature **158**, 648–652 (1946).

[9]J. Lequeux, ed., *Le Verrier—Magnificent and Detestable Astronomer*, Vol. 397, Astrophysics and Space Science Library (Jan. 2013).

[10]J. Stachel, "The first two acts", in *The genesis of general relativity*, Vol. 1, edited by J. Renn (Springer, 2007), pp. 81–111.

[11]A. Einstein, "On the electrodynamics of moving bodies", trans. by A. Beck, Ann. Phys. **322**, 891–921 (1989).

[12]A. Einstein, "On the principle of relativity", trans. by A. Engel, Vossische Zeitung **209**, 33–34 (1997).

[13]J. B. Hartle, *Gravity: an introduction to Einstein's general relativity* (Cambridge University Press, 2021).

[14]C. W. Misner, K. S. Thorne and J. A. Wheeler, *Gravitation* (Princeton University Press, 2017).

[15]J. Creighton and W. Anderson, *Gravitational-Wave Physics and Astronomy: An Introduction to Theory, Experiment and Data Analysis.* (2011).

[16]K. Schwarzschild, "On the gravitational field of a mass point according to Einstein's theory", trans. by S. Antoci and A. Loinger, Sitzungsber. Preuss. Akad. Wiss. Berlin, 189–196 (1999).

[17]L. C. Loveridge, "Physical and geometric interpretations of the Riemann tensor, Ricci tensor, and scalar curvature", (2004), arXiv:gr-qc/0401099.

[18]S. M. Carroll, "Lecture notes on general relativity", (1997), arXiv:gr - qc / 9712019.

[19]L. Blanchet, T. Damour, B. R. Iyer, C. M. Will and A. G. Wiseman, "Gravitational-Radiation Damping of Compact Binary Systems to Second Post-Newtonian Order", Phys. Rev. Lett. **74**, 3515–3518 (1995), arXiv:gr - qc/9501027 [gr-qc].

[20]R. A. Hulse and J. H. Taylor, "Discovery of a pulsar in a binary system.", Astrophys. J. Lett. **195**, L51–L53 (1975).

[21]J. H. Taylor and J. M. Weisberg, "A new test of general relativity - Gravitational radiation and the binary pulsar PSR 1913+16", Astrophys. J. **253**, 908–920 (1982).

[22]J. M. Weisberg and Y. Huang, "Relativistic Measurements from Timing the Binary Pulsar PSR B1913+16", Astrophys. J. **829**, 55 (2016), arXiv:1606.02744 [astro-ph.HE].

[23]J. M. Weisberg, J. H. Taylor and L. A. Fowler, "Gravitational waves from an orbiting pulsar", Sci. Am. **245**, 74–82 (1981).

[24]J. Aasi et al. (LIGO Scientific Collaboration), "Advanced LIGO", Class. Quantum Gravity **32**, 074001 (2015), arXiv:1411.4547 [gr-qc].

[25]F. Acernese et al. (Virgo Collaboration), "Advanced Virgo: a second-generation interferometric gravitational wave detector", Class. Quantum Gravity **32**, 024001 (2015), arXiv:1408.3978 [gr-qc].

[26]T. Akutsu et al. (KAGRA Collaboration), "Overview of KAGRA: Detector design and construction history", Prog. Theor. Exp. Phys. **2021**, 05A101 (2021), arXiv:2005.05574 [physics.ins-det].

[27]B. P. Abbott et al. (KAGRA Collaboration, LIGO Scientific Collaboration, Virgo Collaboration), "Prospects for observing and localizing gravitational-wave transients with Advanced LIGO, Advanced Virgo and KAGRA", Living Rev. Relativ. **23**, 3 (2020).

[28]B. P. Abbott et al. (LIGO Scientific Collaboration, Virgo Collaboration), "Observation of Gravitational Waves from a Binary Black Hole Merger", Phys. Rev. Lett. **116**, 061102 (2016), arXiv:1602.03837 [gr-qc].

[29]B. P. Abbott et al. (LIGO Scientific Collaboration, Virgo Collaboration), "Tests of General Relativity with GW150914", Phys. Rev. Lett. **116**, 221101 (2016), arXiv:1602.03841 [gr-qc].

[30]B. P. Abbott et al. (LIGO Scientific Collaboration, Virgo Collaboration), "Astrophysical Implications of the Binary Black-hole Merger GW150914", Astrophys. J. Lett. **818**, L22 (2016), arXiv:1602.03846 [astro-ph.HE].

[31]B. P. Abbott et al. (LIGO Scientific Collaboration, Virgo Collaboration), "The Rate of Binary Black Hole Mergers Inferred from Advanced LIGO Observations Surrounding GW150914", Astrophys. J. Lett. **833**, L1 (2016), arXiv:1602.03842 [astro-ph.HE].

[32]S. Adrián-Martínez et al. (Antares Collaboration, IceCube Collaboration, LIGO Scientific Collaboration, Virgo Collaboration), "High-energy neutrino follow-up search of gravitational wave event GW150914 with ANTARES and IceCube", Phys. Rev. D **93**, 122010 (2016), arXiv:1602.05411 [astro-ph.HE].

[33]B. P. Abbott et al. (LIGO Scientific Collaboration, Virgo Collaboration, Australian Square Kilometer Array Pathfinder (ASKAP) Collaboration, BOOTES Collaboration, Dark Energy Survey and Dark Energy Camera GW-EM Collaborations, Fermi GBM Collaboration, GRAvitational Wave Inaf TeAm (GRAWITA), INTEGRAL Collaboration, Intermediate Palomar Transient Factory (iPTF) Collaboration, InterPlanetary Network, J-GEM Collaboration, La Silla–QUEST Survey, Liverpool Telescope Collaboration, Low Frequency Array (LOFAR) Collaboration, MASTER Collaboration, MAXI Collaboration, Murchison Wide-field Array (MWA) Collaboration, Pan-STARRS Collaboration, PESSTO Collaboration, Pi of the Sky Collaboration, SkyMapper Collaboration, Swift Collaboration, TAROT, Zadko, Algerian National Observatory, C2PU

Collaboration, TOROS Collaboration, VISTA Collaboration), "Localization and Broadband Follow-up of the Gravitational-wave Transient GW150914", Astrophys. J. Lett. **826**, L13 (2016), arXiv:1602.08492 [astro-ph.HE].

[34]D. V. Martynov et al., "Sensitivity of the Advanced LIGO detectors at the beginning of gravitational wave astronomy", Phys. Rev. D **93**, 112004 (2016), arXiv:1604.00439 [astro-ph.IM].

[35]B. P. Abbott et al. (LIGO Scientific Collaboration, Virgo Collaboration), "GW150914: The Advanced LIGO Detectors in the Era of First Discoveries", Phys. Rev. Lett. **116**, 131103 (2016), arXiv:1602.03838 [gr-qc].

[36]B. P. Abbott et al. (LIGO Scientific Collaboration, Virgo Collaboration), "Binary Black Hole Mergers in the First Advanced LIGO Observing Run", Phys. Rev. X **6**, 041015 (2016), arXiv:1606.04856 [gr-qc].

[37]B. P. Abbott et al. (LIGO Scientific Collaboration, Virgo Collaboration), "GWTC-1: A Gravitational-Wave Transient Catalog of Compact Binary Mergers Observed by LIGO and Virgo during the First and Second Observing Runs", Phys. Rev. X **9**, 031040 (2019), arXiv:1811.12907 [astro-ph.HE].

[38]M. Walker, A. F. Agnew, J. Bidler, A. Lundgren, A. Macedo, D. Macleod, T. J. Massinger, O. Patane and J. R. Smith, "Identifying correlations between LIGO's astronomical range and auxiliary sensors using lasso regression", Class. Quantum Gravity **35**, 225002 (2018), arXiv:1807.02592 [astro-ph.IM].

[39]H.-Y. Chen, D. E. Holz, J. Miller, M. Evans, S. Vitale and J. Creighton, "Distance measures in gravitational-wave astrophysics and cosmology", Class. Quantum Gravity **38**, 055010 (2021), arXiv:1709.08079 [astro-ph.CO].

[40]L. S. Finn and D. F. Chernoff, "Observing binary inspiral in gravitational radiation: One interferometer", Phys. Rev. D **47**, 2198–2219 (1993), arXiv:gr-qc/9301003 [gr-qc].

[41]R. Abbott et al. (LIGO Scientific Collaboration, Virgo Collaboration), "Open data from the first and second observing runs of Advanced LIGO and Advanced Virgo", SoftwareX **13**, 100658 (2021), arXiv:1912.11716 [gr-qc].

[42]B. P. Abbott et al. (LIGO Scientific Collaboration, Virgo Collaboration), "GW170814: A Three-Detector Observation of Gravitational Waves from a Binary Black Hole Coalescence", Phys. Rev. Lett. **119**, 141101 (2017), arXiv:1709.09660 [gr-qc].

[43]B. P. Abbott et al. (LIGO Scientific Collaboration, Virgo Collaboration), "GW170817: Observation of Gravitational Waves from a Binary Neutron Star Inspiral", Phys. Rev. Lett. **119**, 161101 (2017), arXiv:1710.05832 [gr-qc].

[44]B. P. Abbott et al. (LIGO Scientific Collaboration, Virgo Collaboration, Fermi Gamma-Ray Burst Monitor, INTEGRAL), "Gravitational Waves and Gamma-Rays from a Binary Neutron Star Merger: GW170817 and GRB 170817A", Astrophys. J. Lett. **848**, L13 (2017), arXiv:1710.05834 [astro-ph.HE].

[45]B. P. Abbott et al. (LIGO Scientific Collaboration, Virgo Collaboration, Fermi GBM, INTEGRAL, IceCube Collaboration, AstroSat Cadmium Zinc Telluride Imager Team, IPN Collaboration, The Insight-Hxmt Collaboration, ANTARES Collaboration, The Swift Collaboration, AGILE Team, The 1M2H Team, The Dark Energy Camera GW-EM Collaboration, the DES Collaboration, The DLT40 Collaboration, GRAWITA: GRAvitational Wave Inaf TeAm, The Fermi Large Area Telescope Collaboration, ATCA: Australia Telescope Compact Array,

ASKAP: Australian SKA Pathfinder, Las Cumbres Observatory Group, OzGrav, DWF (Deeper, Wider, Faster Program), AST3, CAASTRO Collaborations, The VINROUGE Collaboration, MASTER Collaboration, J-GEM, GROWTH, JAGWAR, Caltech- NRAO, TTU-NRAO, NuSTAR Collaborations, Pan-STARRS, The MAXI Team, TZAC Consortium, KU Collaboration, Nordic Optical Telescope, ePESSTO, GROND, Texas Tech University, SALT Group, TOROS: Transient Robotic Observatory of the South Collaboration, The BOOTES Collaboration, MWA: Murchison Widefield Array, The CALET Collaboration, IKI-GW Follow-up Collaboration, H.E.S.S. Collaboration, LOFAR Collaboration, LWA: Long Wavelength Array, HAWC Collaboration, The Pierre Auger Collaboration, ALMA Collaboration, Euro VLBI Team, Pi of the Sky Collaboration, The Chandra Team at McGill University, DFN: Desert Fireball Network, ATLAS, High Time Resolution Universe Survey, RIMAS, RATIR, SKA South Africa/MeerKAT), "Multi-messenger Observations of a Binary Neutron Star Merger", Astrophys. J. Lett. **848**, L12 (2017), arXiv:1710.05833 [astro-ph.HE].

[46]A. Balasubramanian, A. Corsi, K. P. Mooley, K. Hotokezaka, D. L. Kaplan, D. A. Frail, G. Hallinan, D. Lazzati and E. J. Murphy, "GW170817 4.5 Yr After Merger: Dynamical Ejecta Afterglow Constraints", Astrophys. J. **938**, 12 (2022), arXiv:2205.14788 [astro-ph.HE].

[47]B. P. Abbott et al. (LIGO Scientific Collaboration, Virgo Collaboration, 1M2H Collaboration, Dark Energy Camera GW-EM Collaboration, DES Collaboration, DLT40 Collaboration, Las Cumbres Observatory Collaboration, VINROUGE Collaboration, MASTER Collaboration), "A gravitational-wave standard siren

measurement of the Hubble constant", Nature **551**, 85–88 (2017), arXiv:1710.05835 [astro-ph.CO].

[48]B. P. Abbott et al. (LIGO Scientific Collaboration, Virgo Collaboration), "Tests of General Relativity with GW170817", Phys. Rev. Lett. **123**, 011102 (2019), arXiv:1811.00364 [gr-qc].

[49]B. P. Abbott et al. (LIGO Scientific Collaboration, Virgo Collaboration), "GW170817: Measurements of Neutron Star Radii and Equation of State", Phys. Rev. Lett. **121**, 161101 (2018), arXiv:1805.11581 [gr-qc].

[50]A. Buikema et al., "Sensitivity and performance of the Advanced LIGO detectors in the third observing run", Phys. Rev. D **102**, 062003 (2020), arXiv:2008.01301 [astro-ph.IM].

[51]M. Tse et al., "Quantum-Enhanced Advanced LIGO Detectors in the Era of Gravitational-Wave Astronomy", Phys. Rev. Lett. **123**, 231107 (2019).

[52]R. Abbott et al. (LIGO Scientific Collaboration, Virgo Collaboration), "GWTC-2: Compact Binary Coalescences Observed by LIGO and Virgo during the First Half of the Third Observing Run", Phys. Rev. X **11**, 021053 (2021), arXiv:2010.14527 [gr-qc].

[53]R. Abbott et al. (LIGO Scientific Collaboration, Virgo Collaboration), "GWTC-2.1: Deep extended catalog of compact binary coalescences observed by LIGO and Virgo during the first half of the third observing run", Phys. Rev. D **109**, 022001 (2024), arXiv:2108.01045 [gr-qc].

[54]R. Abbott et al. (LIGO Scientific Collaboration, Virgo Collaboration, KAGRA Collaboration), "GWTC-3: Compact Binary Coalescences Observed by LIGO

and Virgo during the Second Part of the Third Observing Run", Phys. Rev. X **13**, 041039 (2023), arXiv:2111.03606 [gr-qc].

[55]R. Abbott et al. (LIGO Scientific Collaboration, Virgo Collaboration), "GW190412: Observation of a binary-black-hole coalescence with asymmetric masses", Phys. Rev. D **102**, 043015 (2020), arXiv:2004.08342 [astro-ph.HE].

[56]R. Abbott et al. (LIGO Scientific Collaboration, Virgo Collaboration), "GW190814: Gravitational Waves from the Coalescence of a 23 Solar Mass Black Hole with a 2.6 Solar Mass Compact Object", Astrophys. J. Lett. **896**, L44 (2020), arXiv:2006.12611 [astro-ph.HE].

[57]B. P. Abbott et al. (LIGO Scientific Collaboration, Virgo Collaboration), "GW190425: Observation of a Compact Binary Coalescence with Total Mass $\sim$ 3.4 $M_\odot$", Astrophys. J. Lett. **892**, L3 (2020), arXiv:2001.01761 [astro-ph.HE].

[58]R. Abbott et al. (LIGO Scientific Collaboration, Virgo Collaboration), "GW190521: a binary black hole merger with a total mass of 150 $M_\odot$", Phys. Rev. Lett. **125**, 101102 (2020), arXiv:2009.01075 [gr-qc].

[59]C. L. Fryer, S. E. Woosley and A. Heger, "Pair-Instability Supernovae, Gravity Waves, and Gamma-Ray Transients", Astrophys. J. **550**, 372–382 (2001), arXiv:astro-ph/0007176 [astro-ph].

[60]R. Abbott et al. (LIGO Scientific Collaboration, Virgo Collaboration, KAGRA Collaboration), "Observation of Gravitational Waves from Two Neutron Star-Black Hole Coalescences", Astrophys. J. Lett. **915**, L5 (2021), arXiv:2106.15163 [astro-ph.HE].

[61]R. Abbott et al. (LIGO Scientific Collaboration, Virgo Collaboration), "Population Properties of Compact Objects from the Second LIGO-Virgo

Gravitational-Wave Transient Catalog", Astrophys. J. Lett. **913**, L7 (2021), arXiv:2010.14533 [astro-ph.HE].

[62]R. Abbott et al. (LIGO Scientific Collaboration, Virgo Collaboration, KAGRA Collaboration), "Population of Merging Compact Binaries Inferred Using Gravitational Waves through GWTC-3", Phys. Rev. X **13**, 011048 (2023), arXiv:2111.03634 [astro-ph.HE].

[63]R. Abbott et al. (LIGO Scientific Collaboration, Virgo Collaboration, KAGRA Collaboration), "First joint observation by the underground gravitational-wave detector KAGRA with GEO 600", Prog. Theor. Exp. Phys. **2022**, 063F01 (2022), arXiv:2203.01270 [gr-qc].

[64]A. F. Brooks et al., "Point absorbers in Advanced LIGO", Appl. Opt. **60**, 4047 (2021), arXiv:2101.05828 [physics.ins-det].

[65]S. Soni et al., "LIGO Detector Characterization in the first half of the fourth Observing run", Class. Quantum Gravity **42**, 085016 (2025), arXiv:2409.02831 [astro-ph.IM].

[66]E. Capote et al., "Advanced LIGO detector performance in the fourth observing run", Phys. Rev. D **111**, 062002 (2025), arXiv:2411.14607 [gr-qc].

[67]D. Ganapathy et al., "Broadband Quantum Enhancement of the LIGO Detectors with Frequency-Dependent Squeezing", Phys. Rev. X **13**, 041021 (2023).

[68]A. G. Abac et al., "All-sky search for short gravitational-wave bursts in the first part of the fourth LIGO-Virgo-KAGRA observing run", (2025), arXiv:2507.12374 [astro-ph.HE].

[69]A. G. Abac et al. (LIGO Scientific Collaboration, Virgo Collaboration, KAGRA Collaboration), "Observation of Gravitational Waves from the Coalescence of a 2.5–4.5 M $_\odot$ Compact Object and a Neutron Star", Astrophys. J. Lett. **970**, L34 (2024), arXiv:2404.04248 [astro-ph.HE].

[70]B. Ewing et al., "Performance of the low-latency gstlal inspiral search towards ligo, virgo, and kagra's fourth observing run", Phys. Rev. D **109**, 042008 (2024).

[71]C. Alléné et al., "The MBTA pipeline for detecting compact binary coalescences in the fourth LIGO-Virgo-KAGRA observing run", Class. Quantum Gravity **42**, 105009 (2025), arXiv:2501.04598 [gr-qc].

[72]T. Dal Canton, A. H. Nitz, B. Gadre, G. S. Cabourn Davies, V. Villa-Ortega, T. Dent, I. Harry and L. Xiao, "Real-time Search for Compact Binary Mergers in Advanced LIGO and Virgo's Third Observing Run Using PyCBC Live", Astrophys. J. **923**, 254 (2021), arXiv:2008.07494 [astro-ph.HE].

[73]Q. Chu et al., "SPIIR online coherent pipeline to search for gravitational waves from compact binary coalescences", Phys. Rev. D **105**, 024023 (2022).

[74]K. Chandra, V. Villa-Ortega, T. Dent, C. McIsaac, A. Pai, I. W. Harry, G. S. C. Davies and K. Soni, "Optimized PyCBC search for gravitational waves from intermediate-mass black hole mergers", Phys. Rev. D **104**, 042004 (2021), arXiv:2106.00193 [gr-qc].

[75]S. Klimenko et al., "Method for detection and reconstruction of gravitational wave transients with networks of advanced detectors", Phys. Rev. D **93**, 042004 (2016), arXiv:1511.05999 [gr-qc].

[76]A. G. Abac et al. (LIGO Scientific Collaboration and Virgo Collaboration and KAGRA Collaboration), "Search for Eccentric Black Hole Coalescences during

the Third Observing Run of LIGO and Virgo", Astrophys. J. **973**, 132 (2024), arXiv:2308.03822 [astro-ph.HE].

[77]C. D. Kilpatrick et al., "SN 2023ixf in Messier 101: A Variable Red Supergiant as the Progenitor Candidate to a Type II Supernova", Astrophys. J. Lett. **952**, L23 (2023), arXiv:2306.04722 [astro-ph.SR].

[78]A. G. Abac et al. (LIGO Scientific Collaboration, Virgo Collaboration, KAGRA Collaboration), "Search for gravitational waves emitted from SN 2023ixf", arXiv:2410.16565 (2024), arXiv:2410.16565 [astro-ph.HE].

[79]R. Abbott et al. (LIGO Scientific Collaboration, Virgo Collaboration, KAGRA Collaboration), "Search for Gravitational Waves Associated with Gamma-Ray Bursts Detected by Fermi and Swift during the LIGO-Virgo Run O3b", Astrophys. J. **928**, 186 (2022), arXiv:2111.03608 [astro-ph.HE].

[80]R. Abbott et al. (LIGO Scientific Collaboration, Virgo Collaboration, KAGRA Collaboration, CHIME/FRB Collaboration), "Search for Gravitational Waves Associated with Fast Radio Bursts Detected by CHIME/FRB during the LIGO–Virgo Observing Run O3a", Astrophys. J. **955**, 155 (2023), arXiv:2203.12038 [astro-ph.HE].

[81]R. Abbott et al. (LIGO Scientific Collaboration, Virgo Collaboration, KAGRA Collaboration), "All-sky search for short gravitational-wave bursts in the third Advanced LIGO and Advanced Virgo run", Phys. Rev. D **104**, 122004 (2021), arXiv:2107.03701 [gr-qc].

[82]A. G. Abac et al. (LIGO Scientific Collaboration, Virgo Collaboration, KAGRA Collaboration), "Search for continuous gravitational waves from known

pulsars in the first part of the fourth LIGO-Virgo-KAGRA observing run", arXiv:2501.01495 (2025), arXiv:2501.01495 [astro-ph.HE].

[83]R. Abbott et al. (LIGO Scientific Collaboration, Virgo Collaboration, KAGRA Collaboration), "Search for continuous gravitational wave emission from the Milky Way center in O3 LIGO-Virgo data", Phys. Rev. D **106**, 042003 (2022), arXiv:2204.04523 [astro-ph.HE].

[84]R. Abbott et al. (LIGO Scientific Collaboration, Virgo Collaboration, KAGRA Collaboration), "Model-based Cross-correlation Search for Gravitational Waves from the Low-mass X-Ray Binary Scorpius X-1 in LIGO O3 Data", Astrophys. J. Lett. **941**, L30 (2022), arXiv:2209.02863 [astro-ph.HE].

[85]R. Abbott et al. (LIGO Scientific Collaboration, Virgo Collaboration), "Search of the early O3 LIGO data for continuous gravitational waves from the Cassiopeia A and Vela Jr. supernova remnants", Phys. Rev. D **105**, 082005 (2022), arXiv:2111.15116 [gr-qc].

[86]R. Abbott et al. (LIGO Scientific Collaboration, Virgo Collaboration, KAGRA Collaboration), "Upper limits on the isotropic gravitational-wave background from Advanced LIGO and Advanced Virgo's third observing run", Phys. Rev. D **104**, 022004 (2021), arXiv:2101.12130 [gr-qc].

[87]M. A. McLaughlin, "The North American Nanohertz Observatory for Gravitational Waves", Class. Quantum Gravity **30**, 224008 (2013), arXiv:1310.0758 [astro-ph.IM].

[88]S. Ransom et al., "The NANOGrav Program for Gravitational Waves and Fundamental Physics", Bull. AAS **51**, 195 (2019), arXiv:1908 . 05356 [astro-ph.IM].

[89]R. N. Manchester (IPTA), "The International Pulsar Timing Array", Class. Quantum Gravity **30**, 224010 (2013), arXiv:1309.7392 [astro-ph.IM].

[90]G. Agazie et al. (NANOGrav Collaboration), "The NANOGrav 15 yr Data Set: Evidence for a Gravitational-wave Background", Astrophys. J. Lett. **951**, L8 (2023), arXiv:2306.16213 [astro-ph.HE].

[91]T. W. B. Kibble, "Topology of cosmic domains and strings", J. Phys. A **9**, 1387–1398 (1976).

[92]A. Vilenkin and E. P. S. Shellard, *Cosmic Strings and Other Topological Defects* (Cambridge University Press, July 2000).

[93]J. Goldstone, "Field Theories with Superconductor Solutions", Nuovo Cimento **19**, 154–164 (1961).

[94]S. Coleman and E. Weinberg, "Radiative corrections as the origin of spontaneous symmetry breaking", Phys. Rev. D **7**, 1888–1910 (1973).

[95]J. C. Baez and J. Huerta, "The Algebra of Grand Unified Theories", Bull. Am. Math. Soc. **47**, 483–552 (2010), arXiv:0904.1556 [hep-th].

[96]A. Vilenkin, "Gravitational Field of Vacuum Domain Walls and Strings", Phys. Rev. D **23**, 852–857 (1981).

[97]Y. Nambu, "DUALITY AND HADRODYNAMICS", in Winter School in Theoretical Particle Physics (1986), pp. 573–596.

[98]T. Goto, "Relativistic quantum mechanics of one-dimensional mechanical continuum and subsidiary condition of dual resonance model", Prog. Theor. Phys. **46**, 1560–1569 (1971).

[99]N. Turok, "Grand Unified Strings and Galaxy Formation", Nucl. Phys. B **242**, 520–541 (1984).

[100]D. Garfinkle and T. Vachaspati, "Radiation From Kinky, Cuspless Cosmic Loops", Phys. Rev. D **36**, 2229 (1987).

[101]T. Vachaspati, "Gravity of cosmic loops", Phys. Rev. D **35**, 1767–1775 (1987).

[102]T. Damour and A. Vilenkin, "Gravitational Wave Bursts from Cosmic Strings", Phys. Rev. Lett. **85**, 3761–3764 (2000), arXiv:gr-qc/0004075 [gr-qc].

[103]T. Damour and A. Vilenkin, "Gravitational wave bursts from cusps and kinks on cosmic strings", Phys. Rev. D **64**, 064008 (2001), arXiv:gr-qc/0104026 [astro-ph].

[104]T. Damour and A. Vilenkin, "Gravitational radiation from cosmic (super)strings: Bursts, stochastic background, and observational windows", Phys. Rev. D **71**, 063510 (2005), arXiv:hep-th/0410222 [hep-th].

[105]P. Binétruy, A. Bohé, T. Hertog and D. A. Steer, "Gravitational wave bursts from cosmic superstrings with Y-junctions", Phys. Rev. D **80**, 123510 (2009), arXiv:0907.4522 [hep-th].

[106]R. Abbott et al. (LIGO Scientific Collaboration and Virgo Collaboration and KAGRA Collaboration), "Constraints on Cosmic Strings Using Data from the Third Advanced LIGO–Virgo Observing Run", Phys. Rev. Lett. **126**, 241102 (2021), arXiv:2101.12248 [gr-qc].

[107]J. Aasi et al. (LIGO Scientific Collaboration and Virgo Collaboration), "Constraints on Cosmic Strings from the LIGO-Virgo Gravitational-Wave Detectors", Phys. Rev. Lett. **112**, 131101 (2014), arXiv:1310.2384 [gr-qc].

[108]B. P. Abbott et al. (LIGO Scientific Collaboration and Virgo Collaboration and KAGRA Collaboration), "Constraints on cosmic strings using data from the first

Advanced LIGO observing run", Phys. Rev. D **97**, 102002 (2018), arXiv:1712.01168 [gr-qc].

[109]B. P. Abbott et al. (LIGO Scientific Collaboration and Virgo Collaboration), "All-sky search for short gravitational-wave bursts in the second Advanced LIGO and Advanced Virgo run", Phys. Rev. D **100**, 024017 (2019), arXiv:1904.08976 [astro-ph.CO].

[110]J. L. Borges, *Collected fictions*, trans. by A. Hurley (The Penguin Group, 1998).

[111]P. Nguyen et al., "Environmental noise in advanced LIGO detectors", Class. Quantum Gravity **38**, 145001 (2021), arXiv:2101.09935 [astro-ph.IM].

[112]P. Nguyen, "Environmental Noise in Gravitational Wave Detectors and the Search for Gravitational Wave Signals Associated with Gamma-Ray Burst During LIGO'S Third Observing Run", PhD thesis (University of Oregon, 2022).

[113]O. D. Aguiar, "The Past, Present and Future of the Resonant-Mass Gravitational Wave Detectors", Res. Astron. Astrophys. **11**, 1–42 (2011), arXiv:1009.1138 [astro-ph.IM].

[114]J. Levine and R. Stebbins, "Upper Limit on the Gravitational Flux Reaching the Earth from the Crab Pulsar", Phys. Rev. D **6**, 1465–1468 (1972).

[115]C.-M. Chen, J. M. Nester and W.-T. Ni, "A brief history of gravitational wave research", Chin. J. Phys. **55**, 142–169 (2017), arXiv:1610.08803 [gr-qc].

[116]P. Kwee et al., "Stabilized high-power laser system for the gravitational wave detector advanced ligo", Opt. Express **20**, 10617–10634 (2012).

[117]M. A. Arain and G. Mueller, "Design of the advanced ligo recycling cavities", Opt. Express **16**, 10018–10032 (2008).

[118]M. C. Huber and D. Davis, "Mitigating the effects of instrumental artifacts on source localizations", (2022), arXiv:2208.13844 [astro-ph.IM].

[119]J. S. Areeda, J. R. Smith, A. P. Lundgren, E. Maros, D. M. Macleod and J. Zweizig, "LigoDV-web: Providing easy, secure and universal access to a large distributed scientific data store for the LIGO scientific collaboration", Astron. Comput. **18**, 27–34 (2017), arXiv:1611.01089 [astro-ph.IM].

[120]D. M. Macleod, J. S. Areeda, S. B. Coughlin, T. J. Massinger and A. L. Urban, "GWpy: A Python package for gravitational-wave astrophysics", SoftwareX **13**, 100657 (2021).

[121]J. R. Smith, T. Abbott, E. Hirose, N. Leroy, D. MacLeod, J. McIver, P. Saulson and P. Shawhan, "A hierarchical method for vetoing noise transients in gravitational-wave detectors", Class. Quantum Gravity **28**, 235005 (2011), arXiv:1107.2948 [gr-qc].

[122]R. Essick, P. Godwin, C. Hanna, L. Blackburn and E. Katsavounidis, "Idq: statistical inference of non-gaussian noise with auxiliary degrees of freedom in gravitational-wave detectors", Mach. Learn.: Sci. Technol. **2**, 015004 (2020).

[123]A. Effler, R. M. S. Schofield, V. V. Frolov, G. González, K. Kawabe, J. R. Smith, J. Birch and R. McCarthy, "Environmental influences on the LIGO gravitational wave detectors during the 6th science run", Class. Quantum Gravity **32**, 035017 (2015), arXiv:1409.5160 [astro-ph.IM].

[124]D. Davis et al., "LIGO detector characterization in the second and third observing runs", Class. Quantum Gravity **38**, 135014 (2021), arXiv:2101.11673 [astro-ph.IM].

[125]B. K. Berger et al., "Searching for the causes of anomalous Advanced LIGO noise", Appl. Phys. Lett. **122**, 184101 (2023).

[126]G. Vajente, *Comment to "Comparing DARM spectra and range integrands for 80, 83, and 83 Mpc locks"*, `https://alog.ligo-wa.caltech.edu/aLOG/index.php?callRep=45346`.

[127]J. Bidler, J. Smith and M. Walker, *48 Hz bumps found in DQ shift*, `https://alog.ligo-wa.caltech.edu/aLOG/index.php?callRep=46045`.

[128]P. Fritschel, *Broad noise peaks at 48 Hz & 96 Hz: where do they come from?*, `https://alog.ligo-wa.caltech.edu/aLOG/index.php?callRep=47202`.

[129]M. Ball, A. Helmling-Cornell, J. Warner and R. Schofield, *Status of 48 Hz investigation: often enhanced by fixable chiller fans, no vibrometry evidence for coupling at TCS mirror 2, or that it is related to 48 Hz peak in ISI ST2 Z*, `https://alog.ligo-wa.caltech.edu/aLOG/index.php?callRep=50315`.

[130]B. Canuel, E. Genin, G. Vajente and J. Marque, "Displacement noise from back scattering and specular reflection of input optics in advanced gravitational wave detectors", Opt. Express **21**, 10546–10562 (2013).

[131]J. Marque and G. Vajente, "Stray light issues", in *Advanced interferometers and the search for gravitational waves: lectures from the first VESF school on advanced detectors for gravitational waves*, edited by M. Bassan (Springer, 2014), pp. 275–290.

[132]M. Ball, A. Helmling-Cornell and R. Schofield, *Black Glass Blocking Stray Beam at HAM 3 Viewport as part of 48 Hz Investigation*, `https://alog.ligo-wa.caltech.edu/aLOG/index.php?callRep=52136`.

[133]M. Ball, A. Helmling-Cornell, D. Shoemaker, C. Vorvick, S. Banagiri and R. Schofield, *New beating-shaker technique localizes coupling site of 48 Hz DARM peak, and black glass eliminates it*, https://alog.ligo-wa.caltech.edu/aLOG/index.php?callRep=52184.

[134]A. Helmling-Cornell, R. Schofield and T. Schafer, *EY Anemometers Installed and Operational*, https://alog.ligo-wa.caltech.edu/aLOG/index.php?callRep=59432.

[135]A. Effler et al., *PEM injections status*, https://alog.ligo-la.caltech.edu/aLOG/index.php?callRep=64609.

[136]R. Short, J. Glanzer, A. Helmling-Cornell, A. Effler and R. Schofield, *PEM injections successfully completed - will inform HVAC experiments*, https://alog.ligo-wa.caltech.edu/aLOG/index.php?callRep=69745.

[137]K. S. Thorne, "Nonradial Pulsation of General-Relativistic Stellar Models. III. Analytic and Numerical Results for Neutron Stars", ApJ **158**, 1 (1969).

[138]W. C. G. Ho, D. I. Jones, N. Andersson and C. M. Espinoza, "Gravitational waves from transient neutron star f-mode oscillations", Phys. Rev. D **101**, 103009 (2020), arXiv:2003.12082 [gr-qc].

[139]M. Ball, R. Frey and K. Merfeld, "Prospects for neutron star parameter estimation using gravitational waves from f-modes associated with magnetar flares", Mon. Not. R. Astron. Soc., stae1987 (2024), arXiv:2310.15315 [astro-ph.HE].

[140]A. F. Helmling-Cornell, P. Nguyen, R. M. S. Schofield and R. Frey, "Automated evaluation of environmental coupling for Advanced LIGO gravitational wave

detections", Class. Quantum Gravity **41**, 145003 (2024), arXiv:2312.00735 [gr-qc].

[141]R. Schofield, *Does vibration coupling tend to increase with main laser power? Coupling dropped at PSL by roughly two and at EX by three when power was dropped from 75W to 60W*, https://alog.ligo-wa.caltech.edu/aLOG/index.php?callRep=70808.

[142]C. Compton, *Next lock at 60W input power.* https://alog.ligo-wa.caltech.edu/aLOG/index.php?callRep=70648.

[143]L. K. Nuttall et al., "Improving the data quality of Advanced LIGO based on early engineering run results", Classical and Quantum Gravity **32**, 245005 (2015), arXiv:1508.07316 [gr-qc].

[144]M. Zevin et al., "Gravity Spy: integrating advanced LIGO detector characterization, machine learning, and citizen science", Classical and Quantum Gravity **34**, 064003 (2017), arXiv:1611.04596 [gr-qc].

[145]M. Cabero et al., "Blip glitches in Advanced LIGO data", Classical and Quantum Gravity **36**, 155010 (2019), arXiv:1901.05093 [physics.ins-det].

[146]D. Davis et al., "Improving the sensitivity of Advanced LIGO using noise subtraction", Class. Quantum Gravity **36**, 055011 (2019), arXiv:1809.05348 [astro-ph.IM].

[147]N. J. Cornish and T. B. Littenberg, "Bayeswave: Bayesian inference for gravitational wave bursts and instrument glitches", Classical and Quantum Gravity **32**, 135012 (2015), arXiv:1410.3835 [gr-qc].

[148]R. Ormiston, T. Nguyen, M. Coughlin, R. X. Adhikari and E. Katsavounidis, "Noise reduction in gravitational-wave data via deep learning", Physical Review Research **2**, 033066 (2020), arXiv:2005.06534 [astro-ph.IM].

[149]N. J. Cornish, "Time-frequency analysis of gravitational wave data", Phys. Rev. D **102**, 124038 (2020), arXiv:2009.00043 [gr-qc].

[150]J. D. Merritt, B. Farr, R. Hur, B. Edelman and Z. Doctor, "Transient glitch mitigation in Advanced LIGO data", Phys. Rev. D **104**, 102004 (2021), arXiv:2108.12044 [gr-qc].

[151]F. Robinet, N. Arnaud, N. Leroy, A. Lundgren, D. Macleod and J. McIver, "Omicron: A tool to characterize transient noise in gravitational-wave detectors", SoftwareX **12**, 100620 (2020), arXiv:2007.11374 [astro-ph.IM].

[152]A. Helmling-Cornell and R. Schofield, *Blip glitches not seen when DCPDs dark*, https://alog.ligo-wa.caltech.edu/aLOG/index.php?callRep=57011.

[153]M. Pirello et al., *O4 DAQ test stand update: request for DetChar to look at glitches and lines in data; programable-frequency ADC clock chips eliminated drifting lines*, https://alog.ligo-wa.caltech.edu/aLOG/index.php?callRep=58635.

[154]A. Helmling-Cornell, *Comment to: "O4 DAQ test stand update: request for DetChar to look at glitches and lines in data; programable-frequency ADC clock chips eliminated drifting lines"*, https://alog.ligo-wa.caltech.edu/aLOG/index.php?callRep=59831.

[155]R. Herman, "Dialogo della musica antica et della moderna of Vincenzo Galilei: Translation and Commentary", PhD thesis (North Texas State University, 1973).

[156]F. Acernese et al. (Virgo Collaboration), "Increasing the Astrophysical Reach of the Advanced Virgo Detector via the Application of Squeezed Vacuum States of Light", Phys. Rev. Lett. **123**, 231108 (2019).

[157]J. Glanzer, S. Soni, J. Spoon, A. Effler and G. González, "Noise in the LIGO Livingston gravitational wave observatory due to trains", Class. Quantum Gravity **40**, 195015 (2023), arXiv:2304.07477 [astro-ph.IM].

[158]S. Soni et al., "Reducing scattered light in LIGO's third observing run", Class. Quantum Gravity **38**, 025016 (2021), arXiv:2007.14876 [astro-ph.IM].

[159]K. Janssens et al., "Correlated 1-1000 Hz magnetic field fluctuations from lightning over Earth-scale distances and their impact on gravitational wave searches", Phys. Rev. D **107**, 022004 (2023), arXiv:2209.00284 [gr-qc].

[160]T. Washimi et al., "Effects of lightning strokes on underground gravitational waves observatories", J. Instrum. **16**, P07033 (2021), arXiv:2103.06516 [gr-qc].

[161]B. P. Abbott et al. (LIGO Scientific Collaboration and Virgo Collaboration), "Characterization of transient noise in Advanced LIGO relevant to gravitational wave signal GW150914", Class. Quantum Gravity **33**, 134001 (2016), arXiv:1602.03844 [gr-qc].

[162]R. Schofield et al., *H1 L1 PEM vetting report for the Aug. 17, 2017 BNS candidate*, https://dcc.ligo.org/LIGO-T1800508/public.

[163]The LIGO Scientific Collaboration and The Virgo Collaboration, *Data quality report user documentation*, https://docs.ligo.org/detchar/data-quality-report/, 2018.

[164]The LIGO-Virgo-KAGRA Collaboration, *Dqrtasks user documentation*, https://detchar.docs.ligo.org/dqrtasks/, 2022.

[165] *Pem Central*, https://pem.ligo.org/.

[166] J. A. Malaquias-Reis and A. Effler, *PEM sensor work at EY*, https://alog.ligo-la.caltech.edu/aLOG/index.php?callRep=64021.

[167] F. Clara and A. Helmling-Cornell, *PEM Microphone upgrade*, https://alog.ligo-wa.caltech.edu/aLOG/index.php?callRep=69448.

[168] K. Arai, S. Barnum, P. Fritschel, J. Lewis and S. Waldman, *Output Mode Cleaner Design*, https://dcc.ligo.org/LIGO-T1000276/public.

[169] R. Schofield, *HAM5/6 vibration coupling much reduced after septum window removal, 35.5 Hz DARM peak is from residual coupling in the area*, https://alog.ligo-wa.caltech.edu/aLOG/index.php?callRep=66470.

[170] R. Abbott et al., "Open Data from the Third Observing Run of LIGO, Virgo, KAGRA, and GEO", Astrophys. J. Suppl. Ser. **267**, 29 (2023), arXiv:2302.03676 [gr-qc].

[171] P. Nguyen et al., *Pre-O3 PEM injection summary and links to individual logs*, https://alog.ligo-wa.caltech.edu/aLOG/index.php?callRep=49521.

[172] R. Schofield, C. Austin, N. P. and A. Effler, *LLO Magnetic Injections - O3 couplings*, https://alog.ligo-la.caltech.edu/aLOG/index.php?callRep=45371.

[173] *Gracedb — the gravitational-wave candidate event database*, https://gracedb.ligo.org/.

[174] C. Messick et al., "Analysis framework for the prompt discovery of compact binary mergers in gravitational-wave data", Phys. Rev. D **95**, 042001 (2017), arXiv:1604.04324 [astro-ph.IM].

[175]S. Sachdev et al., "The GstLAL Search Analysis Methods for Compact Binary Mergers in Advanced LIGO's Second and Advanced Virgo's First Observing Runs", (2019), arXiv:1901.08580 [gr-qc].

[176]T. Adams et al., "Low-latency analysis pipeline for compact binary coalescences in the advanced gravitational wave detector era", Class. Quantum Gravity **33**, 175012 (2016), arXiv:1512.02864 [gr-qc].

[177]A. H. Nitz, T. Dal Canton, D. Davis and S. Reyes, "Rapid detection of gravitational waves from compact binary mergers with PyCBC Live", Phys. Rev. D **98**, 024050 (2018), arXiv:1805.11174 [gr-qc].

[178]T. Dal Canton and I. W. Harry, "Designing a template bank to observe compact binary coalescences in Advanced LIGO's second observing run", (2017), arXiv:1705.01845 [gr-qc].

[179]S. Hooper et al., "Summed parallel infinite impulse response filters for low-latency detection of chirping gravitational waves", Phys. Rev. D **86**, 024012 (2012), arXiv:1108.3186 [gr-qc].

[180]Q. Chu, "Low-latency detection and localization of gravitational waves from compact binary coalescences", PhD thesis (Western Australia University, 2017).

[181]Bohé et al., "Improved effective-one-body model of spinning, nonprecessing binary black holes for the era of gravitational-wave astrophysics with advanced detectors", Phys. Rev. D **95**, 044028 (2017), arXiv:1611.03703 [gr-qc].

[182]S. Klimenko, S. Mohanty, M. Rakhmanov and G. Mitselmakher, "Constraint likelihood analysis for a network of gravitational wave detectors", Phys. Rev. D **72**, 122002 (2005), arXiv:gr-qc/0508068 [gr-qc].

[183]LIGO Scientific Collaboration and Virgo Collaboration, GCN **25012** (2019).

[184]P. Welch, "The use of fast fourier transform for the estimation of power spectra: a method based on time averaging over short, modified periodograms", IEEE Trans. Audio Electroacoust. **15**, 70–73 (1967).

[185]M. Hannam et al., "General-relativistic precession in a black-hole binary", Nature **610**, 652–655 (2022), arXiv:2112.11300 [gr-qc].

[186]E. Payne et al., "Curious case of GW200129: Interplay between spin-precession inference and data-quality issues", Phys. Rev. D **106**, 104017 (2022), arXiv:2206.11932 [gr-qc].

[187]W. M. Farr, J. R. Gair, I. Mandel and C. Cutler, "Counting and confusion: Bayesian rate estimation with multiple populations", Phys. Rev. D **91**, 023005 (2015), arXiv:1302.5341 [astro-ph.IM].

[188]M. Dwyer, N. Kijbunchoo, K. Merfeld, D. Sigg and R. McCarthy, *Comment to "Replacing the failing squeezer laser"*, https://alog.ligo-wa.caltech.edu/aLOG/index.php?callRep=51244.

[189]S. Chatterji, L. Blackburn, G. Martin and E. Katsavounidis, "Multiresolution techniques for the detection of gravitational-wave bursts", Class. Quantum Gravity **21**, S1809–S1818 (2004), arXiv:gr-qc/0412119 [gr-qc].

[190]S. Chatterji, "The search for gravitational wave bursts in data from the second LIGO science run", PhD thesis (Massachusetts Institute of Technology, 2005).

[191]J. C. Brown, "Calculation of a constant Q spectral transform", J. Acoust. Soc. Am. **89**, 425–434 (1991).

[192]P. Nguyen and R. Schofield, *Coupling estimates from PEM injections correctly predict LLO DARM glitch near S190510g from thunder-driven vibration at EY*, https://alog.ligo-la.caltech.edu/aLOG/index.php?callRep=46025.

[193]The LIGO Scientific Collaboration and The Virgo Collaboration, *Ligocam user documentation*, https://docs.ligo.org/detchar/data-quality-report/tasks/ligocam-dqr.html, 2018.

[194]M. Punturo et al., "The Einstein Telescope: a third-generation gravitational wave observatory", Class. Quantum Gravity **27**, 194002 (2010).

[195]D. Reitze et al., "Cosmic Explorer: the U.S. Contribution to Gravitational-Wave Astronomy beyond LIGO", Bull. AAS **51**, https://baas.aas.org/pub/2020n7i035 (2019).

[196]N. Aeronautics and S. Administration, *GCN: NASA's Time-Domain and Multimessenger Alert System*, https://https://gcn.nasa.gov/.

[197]LIGO Scientific Collaboration, Virgo Collaboration, KAGRA Collaboration, *IGWN public alerts user guide*, https://https://https://emfollow.docs.ligo.org/userguide/.

[198]F. Di Renzo, F. Fidecaro, M. Razzano and N. Sorrentino, "BRiSTOL - a Band-limited RMS Stationarity Test Tool for Gravitational Wave Data", in 55th Rencontres de Moriond on Gravitation (Jan. 2024), arXiv:2401.15392 [gr-qc].

[199]L. Vazsonyi and D. Davis, "Identifying glitches near gravitational-wave signals from compact binary coalescences using the Q-transform", Class. Quantum Gravity **40**, 035008 (2023), arXiv:2208.12338 [astro-ph.IM].

[200]S. Álvarez-López, A. Liyanage, J. Ding, R. Ng and J. McIver, "GSpyNetTree: a signal-vs-glitch classifier for gravitational-wave event candidates", Class. Quantum Gravity **41**, 085007 (2024), arXiv:2304.09977 [gr-qc].

[201]S. Mozzon, L. K. Nuttall, A. Lundgren, T. Dent, S. Kumar and A. H. Nitz, "Dynamic normalization for compact binary coalescence searches in non-stationary noise", Class. Quantum Gravity **37**, 215014 (2020), arXiv:2002.09407 [astro-ph.IM].

[202]R. Macas and A. Lundgren, "Sensitive test of non-Gaussianity in gravitational-wave detector data", Phys. Rev. D **108**, 063016 (2023), arXiv:2306.09019 [gr-qc].

[203]D. Davis, T. B. Littenberg, I. M. Romero-Shaw, M. Millhouse, J. McIver, F. Di Renzo and G. Ashton, "Subtracting glitches from gravitational-wave detector data during the third LIGO-Virgo observing run", Class. Quantum Gravity **39**, 245013 (2022), arXiv:2207.03429 [astro-ph.IM].

[204]C. Chatterjee and K. Jani, "No Glitch in the Matrix: Robust Reconstruction of Gravitational Wave Signals under Noise Artifacts", Astrophys. J. **982**, 102 (2025), arXiv:2412.17185 [gr-qc].

[205]Ligo Scientific Collaboration, VIRGO Collaboration and Kagra Collaboration, "LIGO/Virgo/KAGRA S231118an: Identification of a GW compact binary merger candidate", GRB Coordinates Network **35096**, 1 (2023).

[206]A. Helmling-Cornell, B. Weaver and J. Warner, *Forklift Activity and Gltiching*, https://alog.ligo-wa.caltech.edu/aLOG/index.php?callRep=69899.

[207]Ligo Scientific Collaboration, VIRGO Collaboration and Kagra Collaboration, "LIGO/Virgo/KAGRA S240624cd: Retraction of GW unmodeled transient candidate", GRB Coordinates Network **36747**, 1 (2024).

[208]R. Schofield, *Risk mitigation of acoustic coupling to the ISI tabletops*, https://alog.ligo-wa.caltech.edu/aLOG/index.php?callRep=10274.

[209]J. Hanson, J. Birch, A. Effler and A. Pele, *HAM6 flexures damping and in vac accelerometers*, https://alog.ligo-la.caltech.edu/aLOG/index.php?callRep=19134.

[210]A. G. Abac et al. (LIGO Scientific Collaboration and Virgo Collaboration and KAGRA Collaboration), "All-sky search for long-duration gravitational-wave transients in the first part of the fourth LIGO-Virgo-KAGRA Observing run", (2025), arXiv:2507.12282 [gr-qc].

[211]H. Melville, *Moby-dick or, the whale* (Penguin Classics, 2002).

[212]X. Siemens, J. Creighton, I. Maor, S. R. Majumder, K. Cannon and J. Read, "Gravitational wave bursts from cosmic (super)strings: Quantitative analysis and constraints", Phys. Rev. D **73**, 105001 (2006), arXiv:gr-qc/0603115 [gr-qc].

[213]K. C. Cannon, "A Bayesian coincidence test for noise rejection in a gravitational-wave burst search", Class. Quantum Gravity **25**, 105024 (2008).

[214]M. Litzkow, M. Livny and M. Mutka, "Condor - a hunter of idle workstations", in Proceedings of the 8th International Conference of Distributed Computing Systems (June 1988).

[215]D. Thain, T. Tannenbaum and M. Livny, "Distributed computing in practice: the Condor experience", Concurrency - Practice and Experience **17**, 323–356 (2005).

[216]P. Couvares, T. Kosar, A. Roy, J. Weber and K. Wenger, "Workflow management in Condor", in *Workflows for e-Science: Scientific Workflows for Grids*, edited by I. J. Taylor, E. Deelman, D. B. Gannon and M. Shields (Springer London, London, 2007), pp. 357–375.

[217]LIGO Scientific Collaboration, Virgo Collaboration and KAGRA Collaboration, *LVK Algorithm Library - LALSuite*, Free software (GPL), 2018.

[218]R. P. Fisher, G. Hemming, M.-A. Bizouard, D. A. Brown, P. F. Couvares, F. Robinet and D. Verkindt, "DQSEGDB: A time-interval database for storing gravitational wave observatory metadata", SoftwareX **14**, 100677 (2021), arXiv:2008.11316 [astro-ph.IM].

[219]B. Allen, W. G. Anderson, P. R. Brady, D. A. Brown and J. D. E. Creighton, "FINDCHIRP: An algorithm for detection of gravitational waves from inspiraling compact binaries", Phys. Rev. D **85**, 122006 (2012), arXiv:gr-qc/0509116 [gr-qc].

[220]B. Allen, "χ^2 time-frequency discriminator for gravitational wave detection", Phys. Rev. D **71**, 062001 (2005), arXiv:gr-qc/0405045 [gr-qc].

[221]A. C. Jenkins and M. Sakellariadou, "Anisotropies in the stochastic gravitational-wave background: Formalism and the cosmic string case", Phys. Rev. D **98**, 063509 (2018), arXiv:1802.06046 [astro-ph.CO].

[222]D. F. Chernoff, É. É. Flanagan and B. Wardell, "Gravitational backreaction on a cosmic string: Formalism", Phys. Rev. D **99**, 084036 (2019), arXiv:1808.08631 [gr-qc].

[223]J. J. Blanco-Pillado, K. D. Olum and J. M. Wachter, "Gravitational backreaction simulations of simple cosmic string loops", Phys. Rev. D **100**, 023535 (2019), arXiv:1903.06079 [gr-qc].

[224]O. S. Sazhina, I. I. Bulygin and O. Y. Solodilova, "Problems and Methods of Modern Search for Cosmic Strings", Astron. Rep. **69**, 14–27 (2025).

[225]J. Urrestilla and A. Vilenkin, "Evolution of cosmic superstring networks: a numerical simulation", Journal of High Energy Physics **2008**, 037 (2008), arXiv:0712.1146 [hep-th].

[226]Y. Gouttenoire, G. Servant and P. Simakachorn, "Beyond the Standard Models with cosmic strings", J. Cosmol. Astropart. Phys **2020**, 032 (2020), arXiv:1912.02569 [hep-ph].

[227]L. Lorenz, C. Ringeval and M. Sakellariadou, "Cosmic string loop distribution on all length scales and at any redshift", J. Cosmol. Astropart. Phys **2010**, 003 (2010), arXiv:1006.0931 [astro-ph.CO].

[228]T. Vachaspati and A. Vilenkin, "Gravitational Radiation from Cosmic Strings", Phys. Rev. D **31**, 3052 (1985).

[229]B. Allen and E. P. S. Shellard, "Gravitational radiation from cosmic strings", Phys. Rev. D **45**, 1898–1912 (1992).

[230]J. Polchinski and J. V. Rocha, "Analytic study of small scale structure on cosmic strings", Phys. Rev. D **74**, 083504 (2006), arXiv:hep-ph/0606205 [hep-ph].

[231]P. Auclair, C. Ringeval, M. Sakellariadou and D. Steer, "Cosmic string loop production functions", J. Cosmol. Astropart. Phys **2019**, 015 (2019), arXiv:1903.06685 [astro-ph.CO].

[232]C. Ringeval, M. Sakellariadou and F. R. Bouchet, "Cosmological evolution of cosmic string loops", J. Cosmol. Astropart. Phys **2007**, 023 (2007), arXiv:astro-ph/0511646 [astro-ph].

[233]J. J. Blanco-Pillado, K. D. Olum and B. Shlaer, "Number of cosmic string loops", Phys. Rev. D **89**, 023512 (2014), arXiv:1309.6637 [astro-ph.CO].

[234]The KAGRA Collaboration, the LIGO Scientific Collaboration, and the Virgo Collaboration, *LIGO, Virgo and KAGRA observing run plans*, (2025) (visited on 27/07/2025).

[235]J. Huston The Treasure of the Sierra Madre, film produced by Warner Bros.-First National, Burbank (distributed by Warner Bros. Pictures, 4000 Warner Blvd, Burbank, CA 91505; released 1948), 35 mm, black and white, 127 min.

[236]A. Vilenkin, "Cosmic strings as gravitational lenses", Astrophys. J. Lett. **282**, L51–L53 (1984).

[237]M. Sazhin et al., "CSL-1: chance projection effect or serendipitous discovery of a gravitational lens induced by a cosmic string?", Mon. Not. R. Astron. Soc. **343**, 353–359 (2003), arXiv:astro-ph/0302547 [astro-ph].

[238]N. Kaiser and A. Stebbins, "Microwave anisotropy due to cosmic strings", Nature **310**, 391–393 (1984).

[239]P. A. R. Ade et al., "Planck 2013 results. XXV. Searches for cosmic strings and other topological defects", Astron. Astrophys. **571**, A25 (2014), arXiv:1303.5085 [astro-ph.CO].

[240]T. Vachaspati, A. E. Everett and A. Vilenkin, "Radiation from vacuum strings and domain walls", Phys. Rev. D **30**, 2046–2053 (1984).

[241]H. Jiao, R. Brandenberger and A. Refregier, "Early structure formation from cosmic string loops in light of early JWST observations", Phys. Rev. D **108**, 043510 (2023), arXiv:2304.06429 [astro-ph.CO].

[242]J. J. Blanco-Pillado and K. D. Olum, "Form of cosmic string cusps", Phys. Rev. D **59**, 063508 (1999), arXiv:gr-qc/9810005 [gr-qc].

[243]E. J. Copeland and T. W. B. Kibble, "Kinks and small-scale structure on cosmic strings", Phys. Rev. D **80**, 123523 (2009), arXiv:0909.1960 [astro-ph.CO].

[244]C. Ringeval and T. Suyama, "Stochastic gravitational waves from cosmic string loops in scaling", J. Cosmol. Astropart. Phys **2017**, 027 (2017), arXiv:1709.03845 [astro-ph.CO].

[245]A. Afzal et al., "The NANOGrav 15 yr Data Set: Search for Signals from New Physics", Astrophys. J. Lett. **951**, L11 (2023), arXiv:2306.16219 [astro-ph.HE].

[246]G. Ashton et al., "BILBY: A User-friendly Bayesian Inference Library for Gravitational-wave Astronomy", Astrophys. J. Suppl. Ser. **241**, 27 (2019), arXiv:1811.02042 [astro-ph.IM].

[247]J. S. Speagle, "DYNESTY: a dynamic nested sampling package for estimating Bayesian posteriors and evidences", Mon. Not. R. Astron. Soc. **493**, 3132–3158 (2020), arXiv:1904.02180 [astro-ph.IM].

[248]G. Vajente, Y. Huang, M. Isi, J. C. Driggers, J. S. Kissel, M. J. Szczepańczyk and S. Vitale, "Machine-learning nonstationary noise out of gravitational-wave detectors", Phys. Rev. D **101**, 042003 (2020), arXiv:1911.09083 [gr-qc].

[249]E. Goetz, *H1 Calibrated Sensitivity Spectra Jan 04 2020 (Representative best of O3b -- C01_CLEAN_SUB60HZ)*, https://dcc.ligo.org/LIGO-G2100674/public, 2021.

[250]E. Goetz, *L1 Calibrated Sensitivity Spectra Jan 04 2020 (Representative best of O3b -- C01_CLEAN_SUB60HZ)*, https://dcc.ligo.org/LIGO-G2100675/public, 2021.

[251]E. Thrane and C. Talbot, "An introduction to Bayesian inference in gravitational-wave astronomy: Parameter estimation, model selection, and hierarchical models", Publ. Astron. Soc. Aust. **36**, e010 (2019), arXiv:1809.02293 [astro-ph.IM].

[252]R. Abbott et al., "Properties and Astrophysical Implications of the 150 $M_\odot$ Binary Black Hole Merger GW190521", Astrophys. J. Lett. **900**, L13 (2020), arXiv:2009.01190 [astro-ph.HE].

[253]J. C. Aurrekoetxea, C. Hoy and M. Hannam, "Revisiting the Cosmic String Origin of GW190521", Phys. Rev. Lett. **132**, 181401 (2024), arXiv:2312.03860 [gr-qc].

[254]N. Cornish, L. Sampson, N. Yunes and F. Pretorius, "Gravitational wave tests of general relativity with the parameterized post-Einsteinian framework", Phys. Rev. D **84**, 062003 (2011), arXiv:1105.2088 [gr-qc].

[255]J. J. Blanco-Pillado, K. D. Olum and B. Shlaer, "Cosmic string loop shapes", Phys. Rev. D **92**, 063528 (2015), arXiv:1508.02693 [astro-ph.CO].

[256]J. M. Wachter and K. D. Olum, "Gravitational Smoothing of Kinks on Cosmic String Loops", Phys. Rev. Lett. **118**, 051301 (2017), arXiv:1609.01153 [gr-qc].

[257]Q. Meijer, M. Lopez, D. Tsuna and S. Caudill, "Gravitational-wave searches for cosmic string cusps in Einstein Telescope data using deep learning", Phys. Rev. D **109**, 022006 (2024), arXiv:2308.12323 [astro-ph.IM].

[258]K. Vonnegut, *Galápagos* (Dell Publishing, 1985).

[259]J. Ellis, B. D. Fields and R. Surman, "Do we owe our existence to gravitational waves?", Phys. Lett. B **858**, 139028 (2024), arXiv:2402.03593 [astro-ph.HE].